Enhancing Understanding of Oxygenic Photosynthesis Using Two Dimensional Electronic Spectroscopy

by

Elizabeth L. Maret

A dissertation submitted in partial fulfillment
of the requirements for the degree of
Doctor of Philosophy
(Applied Physics)
in The University of Michigan
2019

Doctoral Committee:

Professor Jennifer P. Ogilvie, Chair
Professor Julie Biteen
Professor Steven Cundiff
Professor Eitan Geva
Professor Roseanne Sension

Elizabeth L. Maret

emaret@umich.edu

ORCID iD: 0000-0002-6385-8982

ACKNOWLEDGEMENTS

As is only appropriate, I must first thank my advisor, Jennifer Ogilvie, for her guidance, support, and encouragement. I feel so lucky to have be advised by someone who believed in me when I didn't believe in myself. I am also gratefully for the support of the Ogilvie lab members that I have interacted with over my tenure with the group. I thank Dr. Amar Bhagwat for his guidance during my early days in the lab, Dr. Vivek Tiwari for the middle days, and Dr. Yin Song and Dr. Orko Konar for the final days. Thanks to the more recently graduated Dr. Seckin Senlick, Dr. Anton Loukianov, Dr. Andy Niedringhaus, and Dr. Veronica Policht plus the soon to be Dr. Yassel Acosta for the grand 20 mile hike adventure through the Porcupine Mountains in the UP. No acknowledgement section from our lab would be complete without recalling this epic event. Thanks as well to Riley Sechrist for always being someone willing to help, even volunteering to come in an relieve me on a weekend so I could get some sleep during a data run. I wish the best of luck to Hoang Nguyen and Ariba Javed on their journey in the lab. Thank you all for your contributions to my learning process.

I must thank my immediate family, Sandy, Greg, Andie and Hannah, for their support at every stage of my life that has ultimately enabled me to complete this dissertation. I feel so fortunate to have not only two parents whose accomplishments I am constantly in awe of, but also two sisters whose own accomplishments I find equally inspiring. I love you all so much.

For me, the boundaries of family have never been limited by blood, so I must also thank my extended family, The Elk Herd (Lynn, Paul, and Mackenzie Hirt included), an outdoor adventure-loving group of engineers, doctors, and creative thinkers, for being the people I turn to for advice when my own family is unreachable for one reason or another (usually the reason involves sun and a sailboat). It is from all of you that I learned the importance of logical thinking and also the healing power of fun. May all your winters be blessed with powder days and summers with serene canoe waters. I wish all the blessings of whatever may be beyond this life to Bud Miller, the great patriarch of the Elk Herd, who passed away during the process of writing this thesis. Papa Bud lived the life I aspire to have; a illustrious and high achieving technical career, skiing as the cure to any winter ailment, and a mind and body as sharp and active as ever until his ripe age of 94. Rest well, old friend.

Reflecting on my time at the University of Michigan and in Ann Arbor, I am so grateful for the opportunities I had learning more than just what I did in the lab. With the support of my friends at PR Run Club (and other running friends, like Robin Bonomi) I was able to run marathons, something I had nearly vowed never to do. It has been from the friendship of the people at PR that I received the most motivation to push through the daily challenges. I consider you all to be my Ann Arbor family. Thank you for being there for me. Ann Arbor also gave me the opportunity to learn to play the fiddle, something I always thought I was physically incapable of. Thanks to the Detroit Irish Music Association for helping me get a start. Thanks as well to Carmen Flesher for her excellent tutelage and all-around awesomeness. You are one of the most impressive of my contemporaries that I have ever met. And thanks to Jeff Barnett for being the friend I need most at a particularly low point. It is through all these people and experiences outside the lab that I received the most motivation and inspiration for my work in the lab.

Finally, and perhaps most importantly, I must thank my fiance, Steph, for the energy and enthusiasm she brings to my life. Thank you for keeping me supported and fed during the long days and nights of data collection and for putting up with my irritability during the writing process. My life is all the richer for having you in it.

TABLE OF CONTENTS

LIST OF FIGURES

Figure

LIST OF TABLES

ABSTRACT

Many aspects of energy and charge transfer in oxygenic photosynthesis are still poorly understood at both the level of single pigments and multi-pigment complexes. At the single pigment level, chlorophylls and chlorophyll-like pigments (including bacteriochlorophyll, pheophytin, etc.) exhibit similar structure in the Q-band absorption region that has long been accepted to have correspondingly similar electronic structure. However, evidence has been mounting that suggests that despite the qualitative similarities between chlorophyll-like pigments they are in fact unique in their electronic structure. On larger length scales, key processes in photosynthesis such as stable charge separation, are accomplished via multiple pigments embedded within a protein matrix acting in concert. Understanding all the intermediate states that occur during charge separation in oxygenic photosynthesis, particularly in the photosystem II complex, is challenging due to the large degree of spectral overlap between chlorophyll and chlorophyll-like pigments. This has made it nearly impossible to disentangle individual pigment contributions from spectroscopic signatures and understand the structure-function relationship in this important system.

This thesis presents my work that capitalizes on the advantages of two-dimensional electronic spectroscopy (2DES), particularly its ability to maintain simultaneous high temporal and spectral resolution, and incorporates further modifications to the technique that allow for studying oxygenic photosynthesis at the single pigment and multi-pigment regimes. By integrating polarization control among the multi-laser pulse experiment I was able to compare the underlying electronic and vibrational energy level structure of bacteriochlorophyll a and chlorophyll a to show how the

structure of chlorophyll a deviates from the simple Gouterman model framework and lends support to the argument for vibronic models. Results of this work were supported by theoretical calculations performed by our collaborators from the group of Eitan Geva in the Chemistry Department at the University of Michigan and the group of Barry Dunietz at Kent State University. Futhermore, I used a multi-spectral 2DES technique, exciting across the Q_y band and probing the higher energy Q_x and carotenoid transitions in the photosystem II reaction center. The 2DES spectra reveal cross peaks between the highly congested Q_y band and Q_x and carotenoid transitions, providing insight into the contributions of the individual pigments to the absorption in the Q_y region. Analysis of the kinetics of the 2DES data allows us to test the proposed two-pathway model of charge separation in the photosystem II reaction center.

The results of these studies emphasize the importance of the feed-back between experiment and theory in building and refining an overall understanding of oxygenic photosynthesis. We anticipate that the information obtained in these studies will contribute to building the new models of the underlying energy structure of single pigments and excitonic interactions that lead to energy and charge transfer in the reaction center of oxygenic photosynthetic complexes.

CHAPTER 1

The Photosystem II Reaction Center

World-wide energy demand has been on the rise for decades. Recent years have seen exponential growth in this demand as more countries enter the first-world arena and build the infrastructure needed to support it. While global awareness of greenhouse gas emitting methods of energy production, like the burning of coal, has been on the rise and considerable effort has been spent attempting to decrease dependency on fossil fuels, more environmentally friendly methods like nuclear power have been met with challenges in remaining an economically viable option [17].

Solar energy is a renewable energy source that has arguably the greatest potential in meeting the world's increasing energy demand. Photosynthetic reaction centers exhibit a quantum efficiency near unity in their initial energy conversion processes [18]. This means that for every photon absorbed by the reaction center, it is almost certain that the complex will achieve a charge separation event and contribute to a build up of charge via a proton gradient. An improved understanding of the design principles governing charge separation in photosynthesis could guide the improvement of artificial light-harvesting materials, ultimately improving large scale solar energy harvesting.

1.1 Photosystem II

Oxygenic photosynthesis is the mechanism by which higher plants, algae, and cyanobacteria use sunlight, carbon dioxide, and water to produce chemical energy stored as carbohydrates via a series of electron transfer reactions. The precise means by which photosynthesis is carried out differs among various photosynthetic organisms that have developed different structural elements to harvest the regions of the solar spectrum that are available to them. However, the overall process is similar, in which light harvesting “antennae” complexes gather light energy. Protein scaffold holds light-absorbing pigments in place at precise separations and relative orientations. The resulting structure couples the electronic transitions of the pigment components to produce an energy “funnel” that moves the electronic excitation through the antennae to a central reaction center (RC). Energy absorbed by the RC initiates an electron transfer chain that creates a charge separated state to form a proton gradient that acts as the biological battery source for the sugar synthesis process [19].

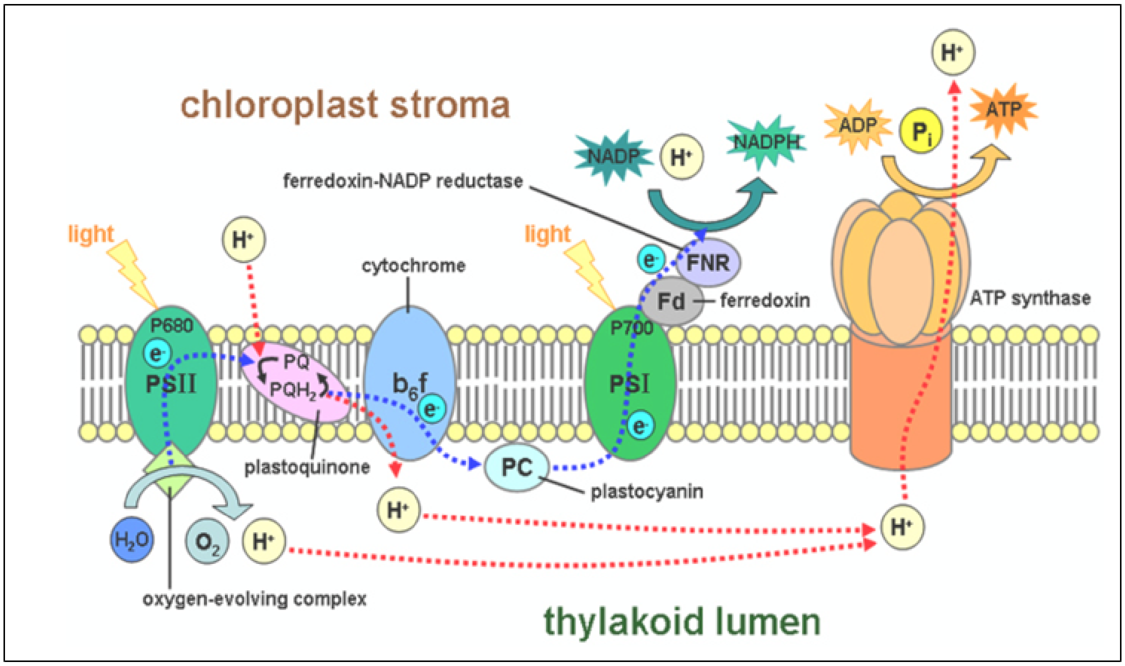

Figure 1.1: A schematic figure of the thylakoid membrane containing the pigment-protein complexes, including photosystem II (furthest left), that execute the light-driven reactions of photosynthesis. Image from [1].

Photosystem II (PSII) is a pigment-protein complex (Figure (1.2)) responsible for charge separation in oxygenic photosynthesis. The PSII complex is found embedded within the grana of thylakoid membranes of the organelles known as chloroplasts (Figure (1.1)). X-ray crstyallography has revealed PSII to be a 700 kDa homodimer with multiple functional sub-units [2]. Antenna complexes rich in chlorophyll a (Chl) pigments funnel energy to core antenna complexes (like CP47 and CP43), which subsequently transfer energy directly to the central RC. Energy absorbed by the PSII RC begins an electron transfer chain that reduces a plastoquinone (Q) and produces a >1 V redox potential [20]. Q is stabilized by protonation from a neighboring tyrosine protein residue. Following two complete RC photocycles, a proton is released into the lipid bilayer and later fuels the cytochrome b_6f (Cyt b_6f) intermediate to oxidize the photosystem I (PSI) complex and drive the ensuing sugar synthesis mechanisms [18].

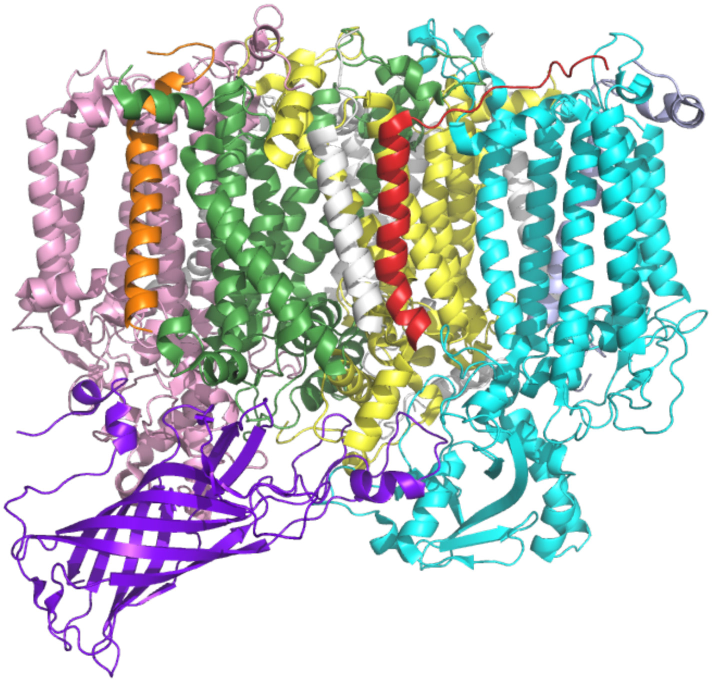

Figure 1.2: Photosystem II monomer protein structure. Figure made in PyMol software using PDB:3WU2 structure of *T. vulcanus* [2].

The role of PSII as the initiator of photosynthesis has made it an object of intense study with much interest focused on the roles of the various complexes, specifically in identifying the RC as the complex that performs charge separation. Isolation of the RC was first reported by Nanba and Satoh [21] with several variations on their original method developed by Berthold et al. [22] and van Leeuwen et al. [23].

1.2 Spectral Congestions in the PSII RC

The PSII RC pigment-protein complex exhibits pseudo-C_2 symmetry, with the axis of symmetry normal to the membrane axis. The two regions created by the axis of symmetry are the D1 and D2 branches. As a whole the RC contains ten light absorbing pigments: six chlorophyll a's (Chl), two pheophytin a's (Phe), and two β-carotene carotenoids (Car) (Figure (1.3)). It is generally understood that energy and charge transfer are carried out by the chlorin pigments (Chl's and Phe's), while the Car pigments serve a protective role, removing free radicals that may disrupt or inhibit the charge transfer process [19, 24]. Two coupled and closely spaced (∼8 Å) Chl pigments make up the PD1 and PD2 pair (also referred to as the "special pair"), where the "D1" and "D2" notation signifies the branch on which the pigment is located. Accessory Chl pigments identified with the ChlD1 and ChlD2 notation are located ∼10 Å (center-to-center) from the special pair. Approximately 10 Å from the accessory Chl pigments are the PheD1 and PheD2 pigments. Auxillary Chl's, ChlzD1 ChlzD2, are approximately 25 Å removed from the PD1 and PD2 pair. All of these distances were determined from the 1.9 Å crystal structure [2]. Models of charge transfer and energy transfer through the RC focus primarily on the roles of the chlorin pigments with some models including only six "core" pigments (PD1, PD2, ChlD1, ChlD2, PheD1, and PheD2), while others use an eight pigment model that also incorporates the Chlz pigments.

Phe and Chl pigments are nearly identical in their chemical structure. They therefore exhibit similar electronic structure, as can be seen in their linear absorption (Figures (1.4) and (1.5)). These spectra of both pigments contain a peak in the 660-670 nm region (referred to as the Q_y peak), a series of smaller peaks between 525-630 nm referred to as the Q_x region, and strong absorption in the 400-440 nm region called the Soret Band (or B Band). Spectral location and electronic structure of these peaks are generally understood within the context of the four-orbital Gouterman model of porphyrins [25,26], where the symmetry of the molecule leads to the Q-band and Soret Band peaks described, with Q-band transition dipole moments oriented within the molecular plane. Partial hydrogenation breaks the symmetry in the Q-band, leading

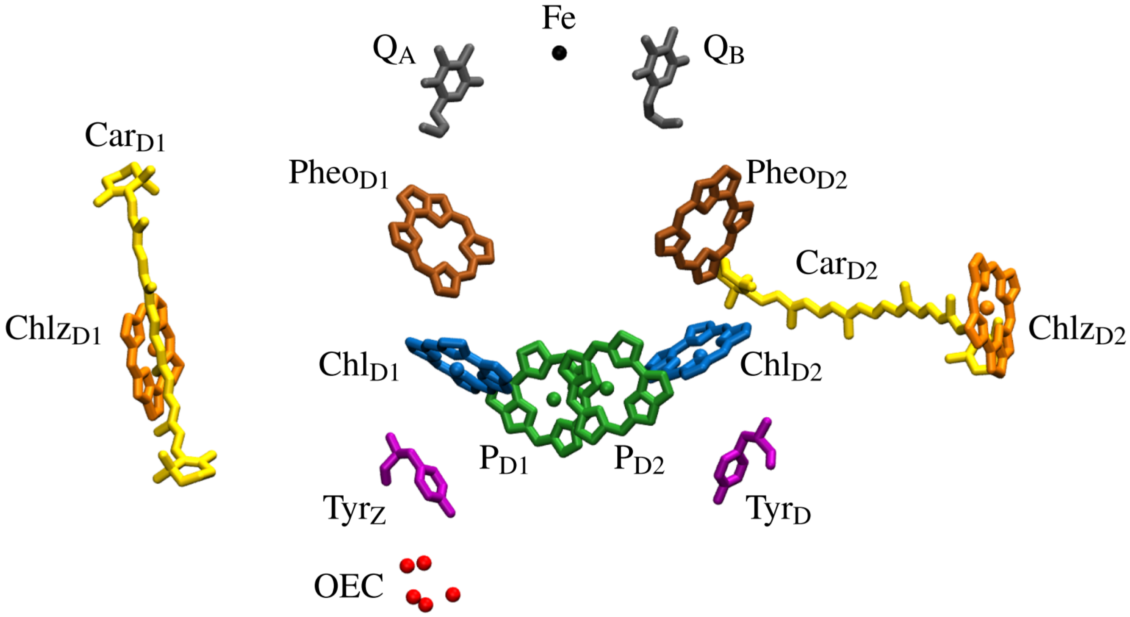

Figure 1.3: Reaction center pigments in the D1-D2-Cyt-b559 complex. Phytol tails of chlorin pigments are removed for simplicity and quinones are shown are removed in the D1-D2-Cyt-b559 preparation. Image from [3].

to the two perpendicularly polarized transitions Q_x and Q_y, where x and y denote the polarization axes in the molecular plane. Chl and Phe absorption peaks are extremely sensitive to the local environment (as can be seen comparing Figures (1.4) and (1.5)) and can experience shifts in their absorption peaks based on the solvent environment. In natural RC environments, orientations and charge from neighboring proteins further influence the pigment electronic structure leading to a RC exhibiting a large degree of spectral congestion, to the point where it becomes nearly impossible to identify spectral contributions in Q_y from individual pigments within the reaction center. This obscures the overall structure-function relationship of the RC.

1.3 Spectroscopy of the PSII RC

It is well established for the PSII RC that a charge separated state between PD1 and the D1 branch quinone ($PD1^+QD1^-$) is formed within 500 ps following absorption by the P680 transition [27]. This is a distance > 20 Å, a charge separation distance too large to be generated by a single excitation. Intermediate charge separated states

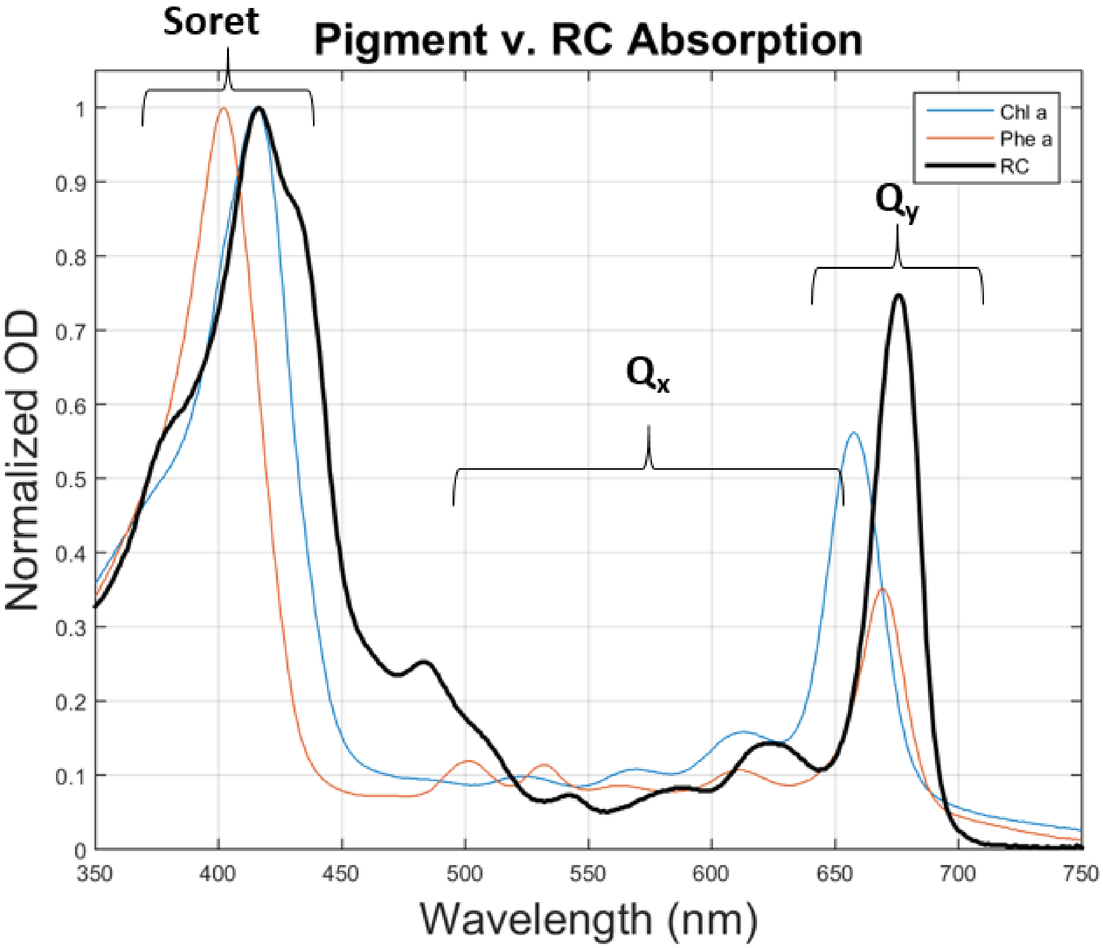

Figure 1.4: Linear absorption spectra of Chl a (blue) and Phe a (orange) in isopropanal compared with an intact and purified reaction center complex in Dx2-β storage buffer (black).

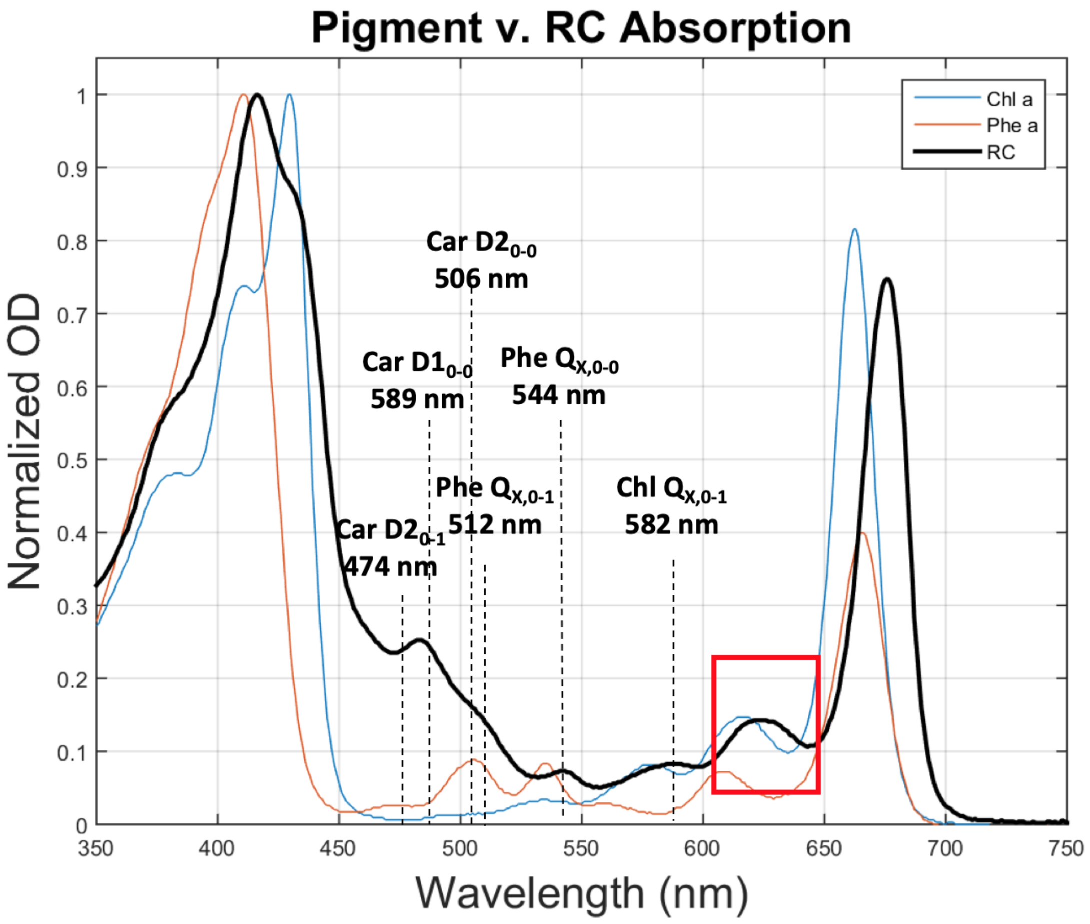

Figure 1.5: Linear absorption spectra of Chl a (blue) and Phe a (orange) in acetone compared with an intact and purified reaction center complex in Dx2-β storage buffer (black). Note the differences in Q_y peak strength and spectral shifts in the Soret band between Chl and Phe pigments as compared with Figure (1.4) with the pigments measured in isoproponal. Labels indicate key pigments and their transition wavelengths referred to throughout this thesis. The red square denotes a peak often ascribed to be the Chl Q_x 0-0 transition, but further discussion in Chapter 4 shows it to be a peak formed from an overlap of Q_x and Q_y electronic/vibrational transitions.

(or radical pair states) must therefore exist that transport the electron on sub-500 ps time scales across the distance of the RC. Identifying these states and determining the mechanism and kinetics of the charge separation process has been the focus of nearly two decades of work by several different researchers [28–30].

Ultrafast spectroscopy experiments have been the primary means of uncovering the charge separation mechanisms of the PSII RC by virtue of their ability to resolve sub picosecond timescales. The spectral complexity of the PSII complex has motivated studies of simpler preparations wherein the photosynthetic antennae are removed leaving the "D1-D2-Cyt-b559" complex (show in Figure (1.3)). Procedures for isolating the D1-D2-Cyt-b559 RC remove the quinones, stopping short of the final charge separated state. This is helpful in performing ultrafast experiments since the repetition rate of solid state ultrafast lasers is generally much faster than this final long-lived state that exists for >1 ms. Isolated RCs are therefore assumed to reach their final charge separated state when the system has relaxed to $\mathrm{PD1^{+}PheD1^{-}}$. Transient absorption studies have been the primary spectroscopic method used to study the PSII RC. Coupled with global analysis, a post-experimental data analysis method [31, 32], data obtained by transient absorption can be used to resolve spectroscopic signatures of intermediate states, providing insight into the mechanism of charge separation. For example, during charge separation, bleaching of the Phe Q_x transition at 544 nm in transient absorption data indicates either that Phe has been excited or Phe has been reduced to $\mathrm{Phe^{-}}$, which follows with increased excited state absorption signal from the anion band at 445 nm.

Efforts to uncover the mechanisms of charge transfer in the PSII RC also utilize exciton models that can help inform the identity of the initially formed radical pair by first identifying the pigments that act as the primary electron donor and the primary electron acceptor. Exciton models often rely on extensive fitting linear and non-linear Stark spectra to identify the Q_y transitions of each pigment. The pigment with the lowest energy transition is considered to be the primary electron donor, fitting with the energy funnel model. Results of exciton models are further used to inform the intermediate states used in kinetic models.

From transient absorption studies in tandem with a combination of global analysis, target analysis, and exciton model studies, current understanding of the PSII RC charge transfer mechanism involves two competing models. One model, developed by Holzwarth et al. [33], posits a single charge separation path where delocalized excitation of the RC forms an initial charge separated pair between ChlD1 and PheD1, where the hole on ChlD1 is then transferred to PD1 before the system relaxes into a long-lived charge separated state:

$$(RC)^* \Longrightarrow ChlD1^+PheD1^- \Longrightarrow PD1^+Phe^- \Longrightarrow (PD1^+PheD1^-)_{relaxed}$$

This model proposes that primary charge separation occurs within 2-4 ps of excitation with ChlD1 as the primary electron donor [34] and PheD1 as the primary electron acceptor. In contrast, a kinetic model developed by the van Grondelle group proposes two competing pathways referred to as the ChlD1 and PD1 pathways for the proposed electron donor pigments [4]. In the ChlD1 pathway (left branch of Figure (1.6)), absorption is delocalized over the ChlD1, PD1, and PD2 pigments. Within 3 ps the ChlD1$^+$PheD1$^-$ radical pair is formed, followed by a second PD1$^+$PheD1$^-$ charge separated state after 58 ps.

$$(ChlD1PD1PD2)^* \Longrightarrow ChlD1^+PheD1^- \Longrightarrow PD1^+PheD1^-$$

On the other hand, the PD1 pathway (right branch of Figure (1.6)) finds excitation to be localized over the special pair and ChlD1 pigments and forming the initial charge separated state within 1 ps of excitation, holding PD1 to be the primary electron donor with ChlD1 as the primary electron accepter. After 37 ps a secondary radical pair is formed between PD1 and PheD1.

$$(PD1ChlD1)^* \Longrightarrow PD1^+ChlD1^- \Longrightarrow PD1^+PheD1^-$$

Considering both pathways, the authors propose that PD1 is the primary electron donor, PheD1 is the primary electron acceptor, and ChlD1 can function as both. The authors also propose that the competing pathways exist as a result of contributions from disorder from the surrounding protein matrix and the ambient temperature.

Exciton models exist that support both the single pathway and two pathway models (further details are presented in Chapter 2), leaving a large degree of uncertainty as to which model is in fact correct. To achieve a higher degree of certainty as to the excitonic structure and charge separation mechanism, it is essential that an experimental method is used which can attain simultaneous high temporal resolution and resolution of the role of the different excitonic and charge transfer states in the charge separation process. Two-dimensional electronic spectroscopy (2DES) meets these demands. 2DES is the optical analogue of NMR techniques that utilize ultrafast pulse sequences to generate nonlinear optical signals retaining information on both the initial excited condition and detected evolution of the system [35]. Furthermore, pulses can be compressed to reach tens of femtosecond resolution, enabling a finer window in which to observe the formation of intermediate states. Thus 2DES can resolve the time dependence of the formation of spectroscopic intermediates as a function of excitation frequency thereby exposing the role of different excitonic states in the charge separation process. In contrast, the more commonly used transient absorption requires the use of narrowband excitation to excite specific excitonic transitions, sacrificing time resolution of their role in the charge separation process.

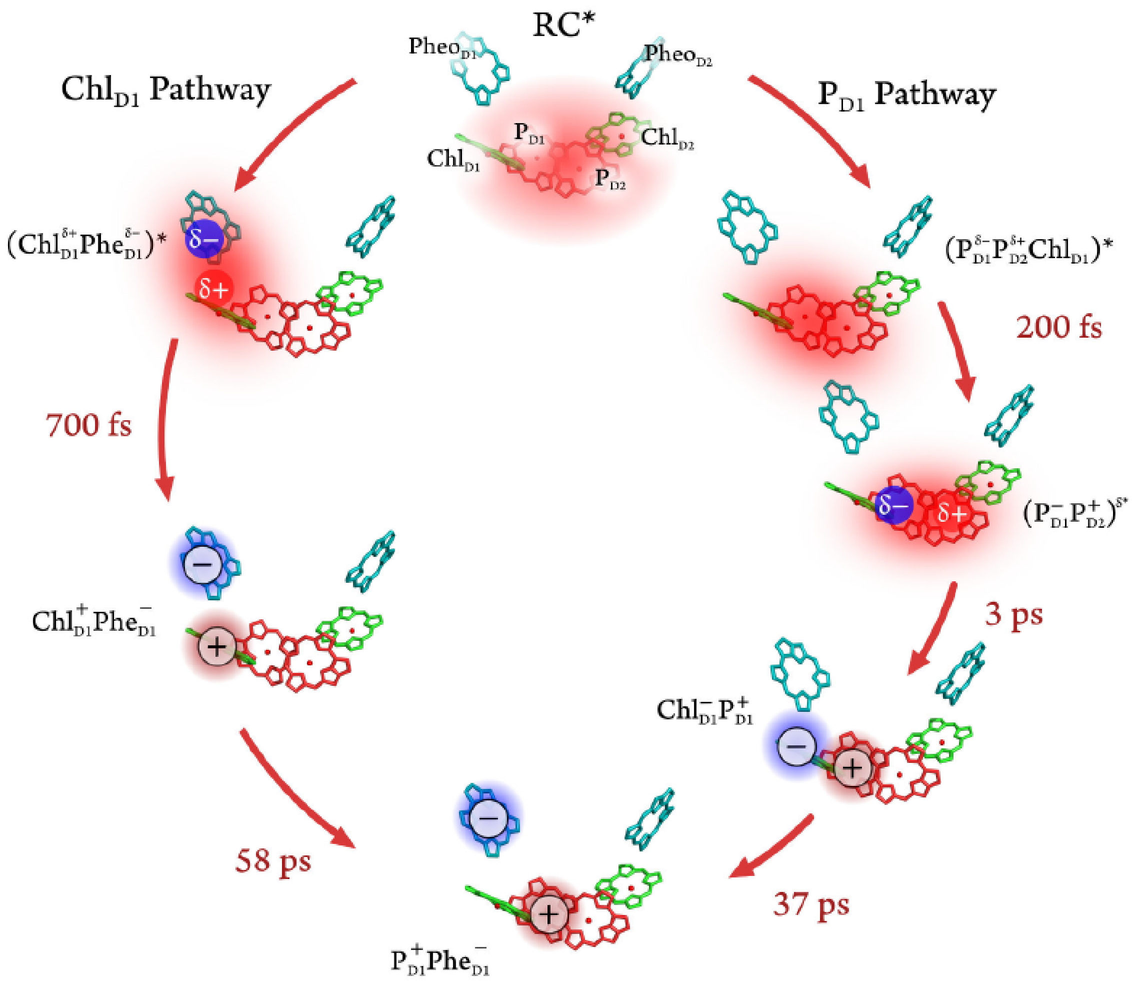

Figure 1.6: An illustration of the ChlD1 and PD1 pathways of the two-pathway model with charge separated state notation as presented in [4] and lifetimes from [5]. Transparent red regions describe the delocalized excitation. Solid blue (negative) and red (positive) regions describe charge separated character. Figure from [6].

1.4 Outline of Thesis

This thesis presents my work using 2DES to further inform our understanding of the mechanisms of the PSII RC during charge separation, examining spectral signatures beyond the Q_y region at both the level of single pigments and the isolated RC. Until recently, the majority of the work done by our lab relating to the charge separation mechanism in the PSII RC has focused on on the Q_y band, involving

2DES measurements coupled with global analysis to identify excitonic coupling [36] and simulations of 2DES spectra from exciton models [37]. We [38, 39] and other groups [40–42] have also looked into the functional role of underlying energy and charge transfer mechanisms in the PSII RC from Q_y data, examining the nature of coherences, implementing Stark spectroscopy, and applying exciton models. However, the large degree of spectral congestion in the Q_y region, however, makes it exceedingly challenging to unambiguously assign spectral signatures to specific pigments. By including information from the Q_x and carotenoid regions, we can identify spectral signatures corresponding to the same pigments participating in Q_y, but with enhanced certainty as to its pigment of origin.

In Chapter 2, I compare three prominent exciton models of the PSII RC found in the literature. Chapter 3 dives into the theoretical details of generating and evaluating 2DES signals. In this chapter I also present the experimental details behind the boxCARS and pump-probe 2DES geometries, which are the methods used to collect the data presented in this thesis. Chapter 4 presents a study which incorporated additional control over the polarization of each experimental pulse to compare the underlying electronic structure of the Q_y and Q_x regions of bacteriochlorophyll a (Bchl a) and chlorophyll a (Chl a) pigments. Chapter 5 presents a study on the PSII RC that attempts to follow spectral signatures of charge separation over a broad bandwidth by exciting the Q_y transition and probing with a white light continuum to observe cross peaks from other pigment transitions and anion band formation. The study attempts to compare the exciton models presented in Chapter 2 with this data to inform the validity of these models. It also tests our data with current models of charge separation, extracting the 2D spectral characteristics of the charge separation intermediates. Finally, Chapter 6 summarizes the major findings of this thesis and presents some thoughts on future directions for the field.

CHAPTER 2

Photosystem II Reaction Center Exciton Models

2.1 An Introduction to Photosynthetic Excitons

In Chapter 1 I described the structure of the Photosystem II D1-D2-Cytb$_{559}$ reaction center (RC), possessing pseudo-C$_2$ symmetry between the D1 and D2 branches, and containing 8 chlorin pigments: the dipole coupled "special pair" chlorophylls PD1 and PD2, the accessory chlorophylls Chl D1 and Chl D2, the pheophytins Phe D1 and Phe D2, and the auxiliary chlorophylls Chl z D1 and Chl z D2. Each of these pigments have similar spectral properties to each other, resulting in considerable spectral congestion in the Q$_y$ band. Within the RC, each pigment is subject to a different local electric field environment as a result of the static charge felt by nearby protein amino acid residues, resulting in unique Q$_y$ spectral shifts for each pigment. Additionally, each pigment is subject to electronic coupling with its neighboring pigments.

In order to describe the electronic structure of photosynthetic systems, a common approach is to introduce the concept of the photosynthetic exciton [43]. The photosynthetic excitons are the eigenstates of the Hamiltonian that describes the coupled system of pigments embedded within the photosynthetic protein. [It is worth noting here that while the term "exciton" is the same as that used in the solid-state community, the concept differs from the quasi-particle created by a delocalized electron-hole pair in that photosynthetic excitons are typically more localized, with larger electron-hole binding energies.] The system Hamiltonian details the electronic transitions of each pigment and the coupling between pigments, generally determined by structure-based calculations. This is called the site-basis Hamiltonian. Diagonalizing the site-basis Hamiltonian results in the exciton-basis Hamiltonian, where each new diagonal element is an exciton composed of a linear combination of site-basis contributions. Considerable interest is placed in the lowest energy exciton and its site-basis contributors as this is the exciton from which the charge transfer process is initiated, according to the energy funnel concepts of photosynthetic light harvesting complexes [19]. For this reason, most studies of the PSII RC have focused on the Q_y band. The lowest energy exciton is thought to provide evidence as to which pigment gives up an electron as the primary electron donor and the subsequent initial radical pair that begins the charge separation process. Both the composition of the lowest energy exciton (in addition to its transition energy value) and the primary electron donor in the PSII RC are still under debate. In this chapter I will present the concepts that go into constructing the site-basis Hamiltonian and compare three recent exciton models used to describe the PSII RC.

2.2 The Site-Basis Hamiltonian

The framework of exciton models for the PSII RC has evolved since it was first conceived with the multimer model, in which all RC pigments transition energies where considered equal [44] and PD1, PD2 did not have strong coupling indicative of the “special pair.” Poor agreement between theoretical models and spectroscopic measurements [45] and higher resolution crystal structure data [2, 46] necessitated a model that considers unique transition energies for each pigment with varied coupling values.

Constructing the site-basis Hamiltonian begins with defining the states involved in the system. Some models consider only a 6 pigment system [7, 47, 48], neglecting contributions from the auxilary Chl z’s. Other models, however, use an 8 pigment system [3, 49], some even including a 9th charge transfer (CT) state [3, 49] (i.e., the radical pair formed immediately following optical absorption that initiates electron transfer). While the CT state is optically dark and does not appear in various linear spectra, the argument for including it is that overlap in the electronic potential manifolds between the primary electron donor and the CT state causes mixing and subsequent transfer of dipole strength to the CT state [9, 10, 49].

The coupling strength between each pigment in the system must also be determined. This relies on crystallography studies to determine pigment orientations and separations in the system, in addition to quantum-chemical calculations to resolve transition dipole moment orientations and strengths, to determine the electronic coupling between pigment neighbors. To date, the highest resolution crystal structure was achieved at 1.9 Å by Umena et al.. [2] and the pigment coupling strengths have been calculated using methods including the Poisson-transition-charges-from-electrostatic-potential method (Poisson-TrEsp) [50] and the point-dipole approximation [49]. Coupling strengths can differ depending on the calculation method used, as shown in Table 1 of Reference [48] and as shown in Table (2.1).

Values for the Q_y electronic transitions, or site-energies, for each pigment are obtain by fitting measured optical spectra, linear absorption, for example, with those calculated from theory, typically by means of a genetic algorithm to optimize the model parameters. A linear absorption spectrum can be calculated with the following equation.

$$A(\omega) = \omega Re \left\{ \int_0^\infty e^{i\omega t} \langle R^{(1)}(t) \rangle dt \right\} \tag{2.1}$$

In essence, Equation (2.1) expresses that the linear absorption is the Fourier transform of the ensemble averaged first-order response function $\langle R^{(1)} \rangle$, where ω is the angular frequency and t is time. Further details of deriving the first-order and higher order response functions are presented in Chapter 3. Here, so as not to be overwhelmed with the details, I simply state that embedded in the first-order response function is the Hamiltonian describing the entire RC system. This Hamiltonian contains the follow parts:

$$\hat{H} = \hat{H}_S + \hat{H}_B + \hat{H}_{SB} + \hat{H}_{SF} \tag{2.2}$$

where $\hat{H}_s$ is the Hamiltonian of the system, describing the electronic properties of the states (pigment and CT) defined for a given model, $\hat{H}_B$ is the Hamiltonian of the bath, $\hat{H}_{SB}$ describes the system-bath coupling, and $\hat{H}_{SF}$ describes the system-field coupling introduced by optical excitation. The form of each element in the Hamiltonian is dependent upon the parameters set by a given model. $\hat{H}_S$ will naturally be dependent on the number of states defined for the model, whether or not a CT state is used and how it describes the degrees of freedom (tight-binding model, etc.). $\hat{H}_B$ is most often represented as a set of harmonic oscillators. $\hat{H}_{SF}$ is described by the optical electric-field interaction with the transition dipole moment operators (further details in Chapter 3).

In Equation (2.2), a term of great consequence is the system-bath coupling $\hat{H}_{SB}$. The pigments in the RC are not held in a vacuum. Instead they are immersed in a chaotic environment, subject to numerous vibrations such as inter- and intra-molecular vibrations, and changes in the electrostatic environment induced by protein conformational changes. The net result of these vibrations is that instead of a spectrum displaying a narrow electronic transition with high certainty in the energy at which that transition occurs, the spectrum is considerably broadened.

Lineshape broadening is modeled in the system-bath coupling by the spectral density $J(\omega)$, which is a function describing the distribution of the modes present in a system (Figure (2.2) shows the spectral densities used in the model described below). Forms of the spectral density can be measured via fluorescence line narrowing (FLN) experiments or spectral hole-burning experiments (SHB) [51]. Common forms of the spectral density used to model photosynthetic complexes are the overdamped Brownian oscillator, B777 (named after the B777 complex in the Light Havesting Complex 1 of purple bacteria, from which it was measured), Ohmic, and Log-Normal. The spectral density used in a given model can have enormous impact on the outcome of the calculation and, hence, the site energies obtained from the fitting. Kell et al.. [12] provide a critical analysis of the commonly used spectral densities in photosynthetic systems (include those previously mentioned) and point out that a single spectral density should not be used to describe all photosynthetic systems. Instead, one should be chosen based on the following criteria: 1) $J(\omega) \to 0$ as $\omega \to 0$, 2) $\omega^2 J(\omega) \to 0$ as $\omega \to \infty$ and 3) the shape should fit well with experimental measurements. While the authors emphasize that the appropriate spectral density must be carefully chosen for a given system, they strongly support a Log-Normal spectral density when modeling the Fenna-Mattews-Olson (FMO) complex or the antenna complex CP29 of PSII.

Given the spectral congestion of the PSII RC, determining the site-energies for each of the pigments in a system requires a simultaneous fit of multiple types of spectra. In the case of the PSII RC, the most commonly used spectra are linear absorption (OD), fluorescence (FL), linear dichroism (LD), circular dichroism (CD), triplet-minus-singlet (T-S), and RC5-RC6 mutant difference spectra where RC5 is the PSII RC missing the Chl D1 and RC6 is the full PSII RC containing all 6 chlorophyll pigments.

In addition to the linear spectra described above, Stark spectroscopy has also been used to determine the site-energy of the CT state. This method has been criticized by Raszewski et al. [48] because Stark spectra are nonlinear and require more parameters to obtain an adequate fit to the data. In addition, these added parameters can make it challenging to compare the results of linear and non-linear measurements. The authors instead promote the use of mutant difference spectra, using mutants with changes to a single protein residue near the target pigment. A different residue near a pigment alters the local electric field environment felt by the pigment, effectively achieving the same goal as a Stark measurement, without introducing numerous additional parameters to fit. In this way, a direct comparison of linear spectra can be made to identify a pigment site-energy, requiring a single adjustment to the site-basis Hamiltonian. The Stark spectrum method has been embraced, however, by Novoderezhkin et al. [9] and Gelzinis et al. [3].

2.3 Comparison of Exciton Models

In this section I present three exciton models that have been used to describe the PSII RC and explain its energy transfer behaviors. These models were chosen for

Site-basis Hamiltonian									
	PD1	**PD2**	**Chl D1**	**Chl D2**	**Phe D1**	**Phe D2**	**Chl z D1**	**Chl z D2**	**CT**
PD1	15080 14970 15190	158 (239)	-27.32 (-17)	-41.83 (-81)	-3.98 (-4)	12.61 (16)	0.45 (1)	0.58 (1)	0
PD2	158 (239)	15015 14970 15180	-46.77 (-82)	-22.04 (-10)	15.06 (20)	-2.99 (-4)	0.6 (1)	0.61 (1)	0
Chl D1	-27.32 (-17)	-46.77 (-82)	14800 14749 15000	3.54 (12)	43.51 (71)	-2.18 (-5)	1.67 (3)	-0.09 (0)	125
Chl D2	-41.83 (-81)	-22.04 (-10)	3.54 (12)	15010 14925 15130	-2.37 (-5)	41.65 (64)	-0.05 (0)	1.8 (2)	0
Phe D1	-3.98 (-4)	15.06 (20)	43.51 (71)	-2.37 (-5)	14950 14925 15050	1.55 (3)	-2.52 (-4)	-0.18 (0)	125
Phe D2	12.61 (16)	-2.99 (-4)	-2.18 (-5)	41.65 (64)	1.55 (3)	14850 14815 15060	-0.19 (0)	-2.57 (-4)	0
Chl z D1	0.45 (1)	0.6 (1)	1.67 (3)	-0.05 (0)	-2.52 (-4)	-0.19 (0)	14985 14925 15555	0.15 (0)	0
Chl z D2	0.58 (1)	0.61 (1)	-0.09 (0)	1.8 (2)	-0.18 (0)	-2.57 (-4)	0.15 (0)	15065 15038 15485	0
CT	0	0	125	0	125	0	0	0	14270 15120

Table 2.1: Site-basis Hamiltonian with all values in units of cm^{-1}.

their extensive comparison with experimental data.

Site Energies									
	PD1	**PD2**	**Chl D1**	**Chl D2**	**Phe D1**	**Phe D2**	**Chl z D1**	**Chl z D2**	**CT**
van Grondelle	658.3	658.7	666.7	660.9	664.5	664	642.9	645.8	682
Renger	668	668	678	670	670	675	670	665	
Gelzinis	663	666	675.5	666	669	673.5	667.5	664	701

Table 2.2: The site energies calculated from the van Grondelle, Renger, and Gelzinis models. Values are in units of nm. Red values indicate the lowest energy pigment and CT state (if used) for each model. Blue values indicate the highest energy value.

van Grondelle Model - Details of the model proposed by the van Grondelle group can be found in references [9,10,49]. This model proposes 8 electronic states for the 8 RC pigments, plus 1 CT state. Coupling values were found using the crystal structure of Kamiya and Shen [46] and calculations using the point-dipole approximation. OD, FL, LD, CD, T-S, and RC5-RC6 linear spectra were fit using an overdamped Brownian oscillator (Figure 2.2) with 48 underdamped high-frequency modes. The spectral density is mathematically described by the following equation, where the left-hand term describes the overdamping and the right-hand term describes the underdamped terms:

$$J(\omega) = 2\lambda_0 \frac{\omega\gamma_0}{\omega^2 + \gamma^2} + \sum_{j=1}^{48} 2\lambda_j \omega_j^2 \frac{\omega\gamma_j}{(\omega_j^2 - \omega^2)^2 + \omega^2\gamma_j^2}. \tag{2.3}$$

In Equation (2.3) 2λ is the Stokes shift, ω is the transition frequency, ω_j is the jth vibrational mode of the spectral density and γ is the damping constant. As can be seen in Figure (2.2) this spectral density favors high frequency modes.

The van Grondelle model also uses Stark spectra to identify the CT state site energy. Site energy values in nm are in Table (2.2). Table (2.1) shows the site-basis

Hamiltonian with the van Grondelle site-energy values in red. The purple values in parentheses are the Renger group's estimation of the van Grondelle coupling values based on the point-dipole approximation. Explicit coupling values used by the van Grondelle group are not published in literature.

Results of the van Grondelle model find the lowest energy exciton to be delocalized over the PD1, PD2, Chl D1, and Phe D1 pigments (Figure (2.1) panel C, k=2) and the CT state (Figure (2.1) panel C, k=1) to be delocalized over PD1, PD2, and Chl D1. For this reason, the authors propose the CT state can be either $\mathrm{PD2^+PD1^-}$ or $\mathrm{ChlD1^+Phe^-}$ and the primary electron donor is either PD2 or Chl D1.

Renger Model - The exciton model developed by the Renger group differs from the van Grondelle model in that it only includes 6 pigments, excluding contributions from the Chl z's (although, the site-energies and coupling values for these pigments are still solved for and are the green values in Table (2.1)) [47, 48, 52]. A CT state is not included in the Renger model since the group is in fact critical of the practice of fitting Stark spectra to identify the CT state [48]. Pigment site energies are found by fitting OD, LD, CD, and FL data, in addition to using OD difference spectra of mutants with altered protein residues. Pigment coupling values are calculated using the Poisson-TrEsp method [52] and the B777 spectral density is used to model lineshape broadening, which favors low-frequency modes (Figure (2.2)). The B777 spectral density is mathematically modeled by the following equation:

$$J(\omega) = \frac{S_0}{s_1 + s_2} \sum_{i=1,2} \frac{s_i}{7!2\omega_i^4} \omega^3 e^{-\sqrt{\frac{\omega}{\omega_i}}} \tag{2.4}$$

where s_i are scaling factors and ω_i are the vibrational modes. Diagonalizing the Renger site-basis Hamiltonian finds the lowest energy exciton is localized on the Chl D1 pigment, which the authors claim to be the primary electron donor [7].

Gelzinis Model - The model developed by Gelzinis et al. [3] borrows elements from both the van Grondelle and Renger models. It incorporates the same 8 pigments and 1

CT state of the van Grondelle model and uses the pigment coupling values determined by the Renger group in reference [52] (green off-diagonal values in Table (2.1)). In addtion, the Gelzinis model uses the blue diagonal and CT off-diagonal elements for it site-energies and CT coupling values, respectively. It deviates from the other two models by using a Super-Ohmic spectral density, which includes both low- and high-frequency terms, both of which specify a cut-off frequency ω_i^c.

$$\begin{aligned} J(\omega) &= J_{LF}(\omega) + J_{HF}(\omega) \\ J_{LF}(\omega) &= \sum_{i=1,2} \lambda_i \frac{\pi}{2} \left(\frac{\omega}{\omega_i^c}\right)^3 \omega^3 e^{-\frac{|\omega|}{\omega_i^c}} \\ J_{HF}(\omega) &= \sum_{j=1}^{8} \frac{4 s_j W_j \omega^3 \Gamma}{\left(\omega^2 - W_j^2 - \Gamma\right)^2 + 4\omega^2\Gamma^2} \end{aligned} \tag{2.5}$$

In Equation (2.5) λ is the reorganization energy, W_j are the vibrational frequencies, Γ is the damping parameter, and s_j are the Huang-Rhys factors. Site-energies (Table (2.2)) are obtained by fitting OD, LD, CD, T-S, and Stark spectra. The authors caution against relying too heavily on fitting fluorescence spectra, since, in general, PSII RCs only fluoresce when damaged and fitting to such data may not be indicative of the complex's natural physiological function. Ultimately, the model finds the lowest energy exciton to be localized on Chl D1 and believe this to be the primary electron donor.

<table>
<tr><th colspan="6">Site Energies</th></tr>
<tr><th></th><th>States</th><th>Spectral Density</th><th>Lowest Energy Exciton Composition</th><th>CT State State</th><th>Primary Electron Donor</th></tr>
<tr><td>**van Grondelle**</td><td>8 Pigments
(1 CT)</td><td>Brownian
Oscillator</td><td>PD1,PD2,
Chl D1, Phe D1</td><td>Chl D1$^+$ Phe D1$^-$
or PD2$^+$PD1$^-$</td><td>Chl D1
or PD2</td></tr>
<tr><td>**Renger**</td><td>6 Pigments</td><td>B777</td><td>Chl D1</td><td>Chl D1$^+$ Phe D1$^-$</td><td>Chl D1</td></tr>
<tr><td>**Gelzinis**</td><td>8 Pigments
(1 CT)</td><td>Super
Ohmic</td><td>Chl D1</td><td>Chl D1$^+$ Phe D1$^-$
(others possible)</td><td>Chl D1</td></tr>
</table>

Table 2.3: A summary of the three exciton models presented here and their respective results.

2.4 Discussion of Exciton Models

Spectral density, as the parameter with the most sensitive influence on the fitting results, is often the point of most criticism in an exciton model. Here I note some of the criticism regarding the spectral densities used in the above models.

Kell et al. [12] and Raszewski et al. [48] severely criticize using an overdamped Brownian oscillator spectral density, as the van Grondelle model does, because it favors high-frequency intra-molecular pigment vibrational modes that have a weak Frank-Condon overlap and does not meet the criteria $J(\omega) \to 0$ as $\omega \to 0$ necessary for a physical model describing photosynthetic complexes. Kell et al. do provide some criticism for the B777 and super-ohmic spectral densities as well. The authors claim that B777 follows the correct limiting behavior (mentioned in the first two criteria above), but does not always provide a good fit to fluorescence line narrowing data. They conclude that it could be a good model for small photosynthetic complexes (like the RC), but not for larger complexes. Regarding the super-ohmic spectral density,

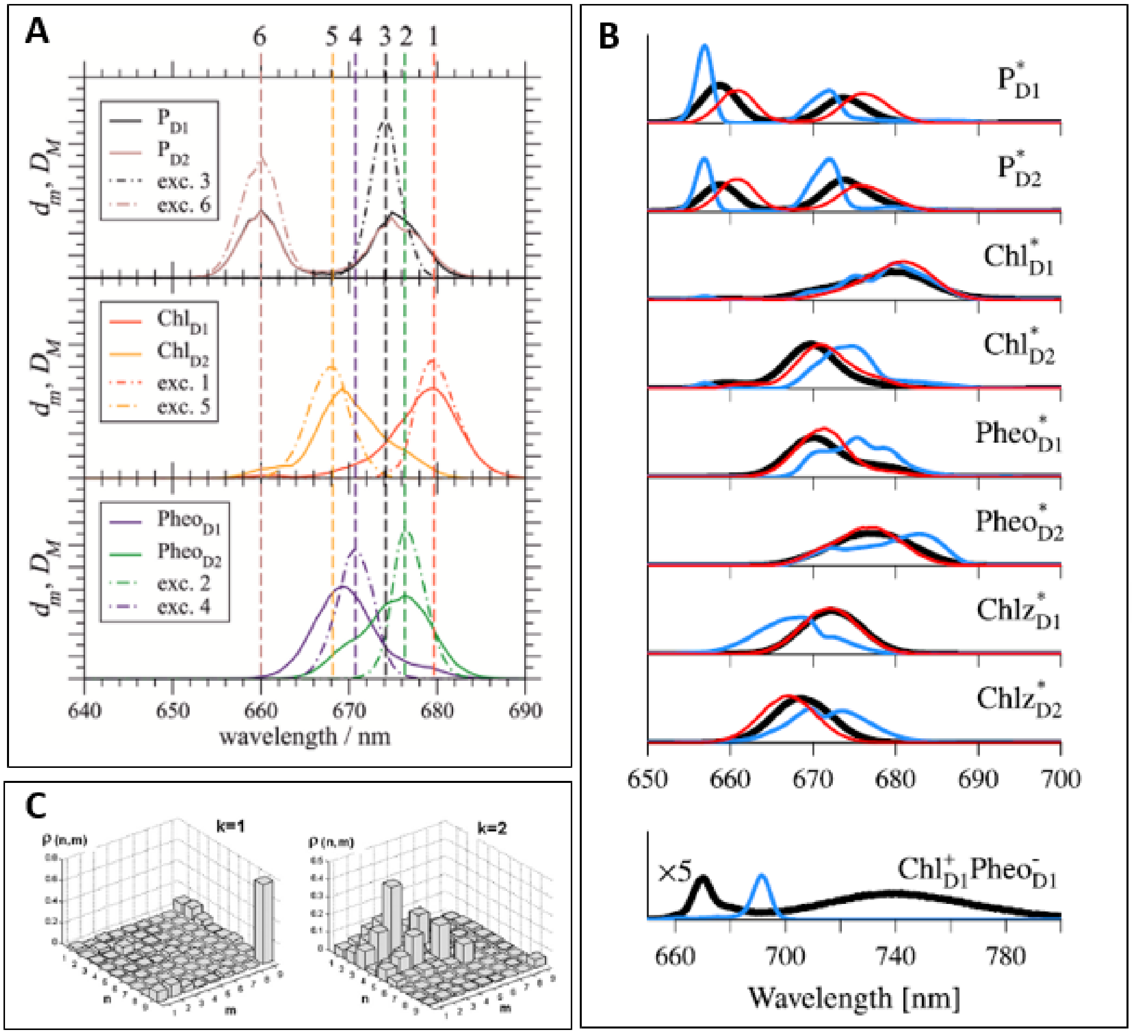

Figure 2.1: **Panel A**: Exciton-state pigment energy distributions resulting from the Renger model [7]. Dashed vertical lines indicate the exciton transition energies corresponding to the number label. Colors of the vertical lines and horizontal curves indicate pigment the distribution corresponds to. **Panel B**: Exciton-state pigment distributions from the Gelzinis model (from [3]). Black lines denote distributions for work presented in [3], blue lines for work in a different study by the same authors [8], and red lines from the Renger model shown in Panel A. **Panel C**: van Grondelle model (from [9]) density matrix contributions. Numbers 1-9 along the matrix axes indicate pigments PD1, PD2, ChlD1, ChlD2, PheD1, PheD2, ChlzD1, ChlzD2, and CT state, respectively. k = 1 and k = 2 indicate the CT (k=1) and lowest energy (k=2) excitons in the model. Note the strong contributions from PD1, PD2, ChlD1, and PheD1 in k=2.

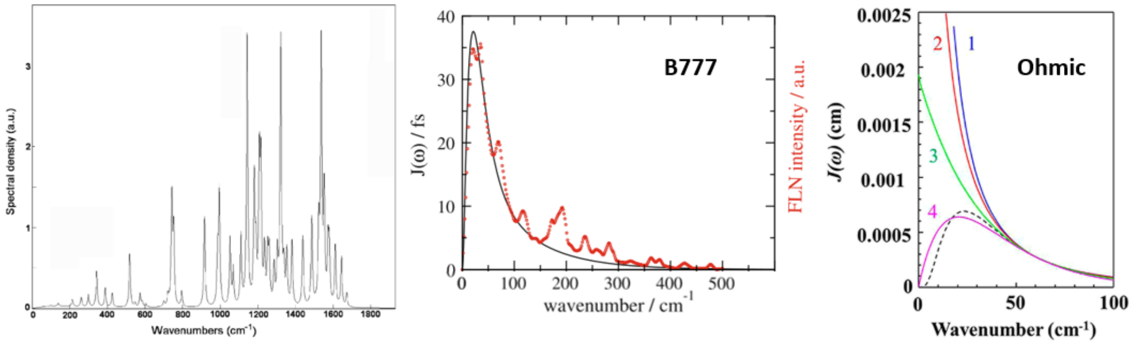

Figure 2.2: Spectral density functions used in the van Grondelle (left, image from [10]), Renger (middle, image from [11]), and Gelzinis (right, curve 4, image taken from [12]) models.

the authors note that it can exhibit divergence as $\omega \to 0$ if not used to a high enough power (i.e., the third power of the $(\frac{\omega}{\omega_i^c})^3$ term in Equation (2.5)). Calculations by Kell et al., however, were made considering the PSII CP29 antenna complex and FMO complex, complexes that are both considerably larger than the PSII RC. These criticisms must therefore be taken with a grain of salt.

Considering the above three exciton models together (a summary of their parameters and results can be found in Table (2.3), there seems to be some consensus that Chl D1 has a strong role to play in the primary charge transfer process in the PSII RC. Evidence against this is in the results of the van Grondelle model, which merely suggests an alternative, or even parallel, primary electron donor, PD2, and initial radical pair formation, $PD2^+PD1^-$. A unifying consensus regarding the appropriate spectral density to be used when modeling the PSII RC still needs to be reached before definite conclusions on the best exciton model can be made. Chapter 5 of this thesis seeks to use the ability to resolve an excitation dependent frequency axis of 2D spectroscopy to provide more support in distinguishing among the various exciton models of the PSII RC.

Figures (2.3)-(2.5) show the resulting excitons from diagonalizing the Hamiltonian in Table (2.1) for the Gelzinis model, Renger model, and van Grondelle model. In the Hamiltonian red elements are the site energies given by the van Grondelle model in [9], blue elements are the site energies and couplings used by the Gelzinis model in [3], and green elements are the site energies and couplings used in the Renger model in [7]. The Gelzinis model uses the the same coupling values as the Renger model, which were calculated using the Poisson-TrEsp method. Purple elements in parentheses are the coupling values calculated by the Renger group in [48] based on the point-dipole method used by the van Grondelle group in their model. Coupling values used by the van Grondelle group are not explicitly available in literature. In Figures (2.3)-(2.5), X-axis values for each bar indicate the exciton-basis eigenvalues (or, exciton-basis transition value) in wavelength. In diagonalizing the site-basis Hamiltonian, a matrix of the squared amplitudes for each pigment contribution is generated. The percent contribution of each pigment in each exciton was calculated by taking the square root of the given amplitude and dividing it by the sum of all the pigment contributions for a given exciton. Relative size of the colored elements inside each exciton bar indicate this percent contribution of the corresponding pigment. Heights of the bars indicate the transition dipole strength. I refer back to these bar plots when analyzing the data presented in Chapter 5.

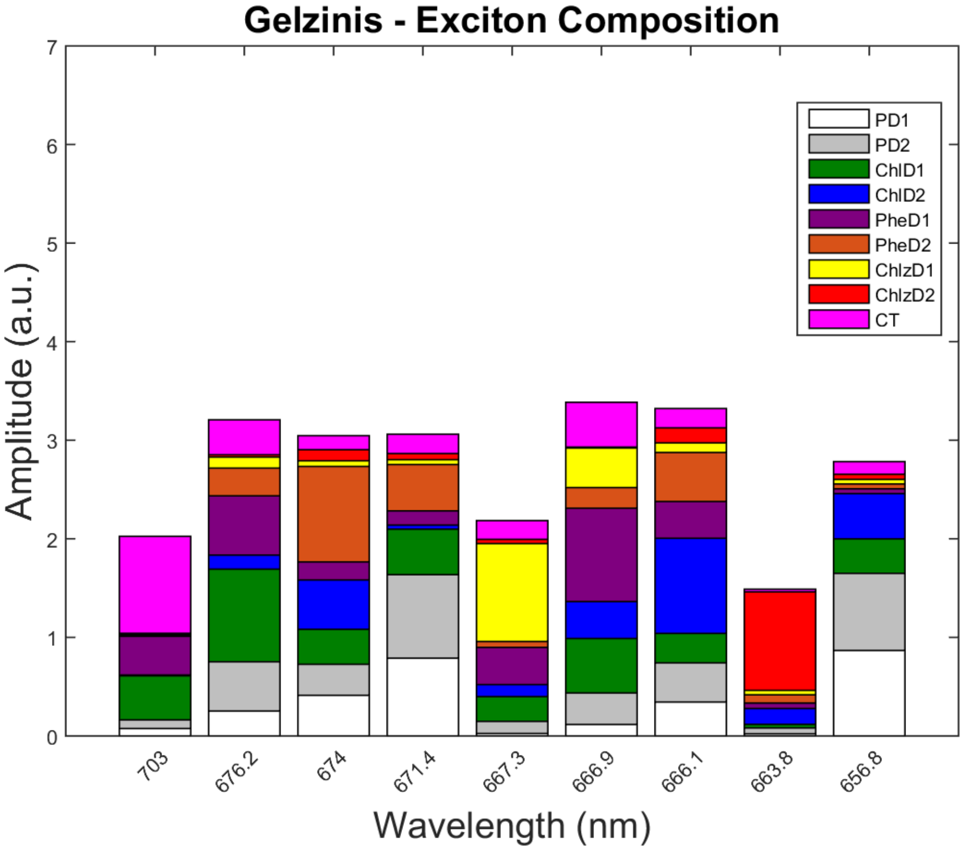

Figure 2.3: Gelzinis model exciton composition. Exciton transition energies (provided in wavelength on the x-axis) were calculated by diagonalizing the site-basis Hamiltonian in Table (2.1) using the blue diagonal and green coupling values. The square root of each element in the resulting amplitude matrix to find the contributing amplitude of each pigment for a given exciton. The total amplitude contribution from each pigment in an exciton is reflected in the height of each bar in the figure. Colors indicate the percent contribution of the corresponding pigment to that exciton.

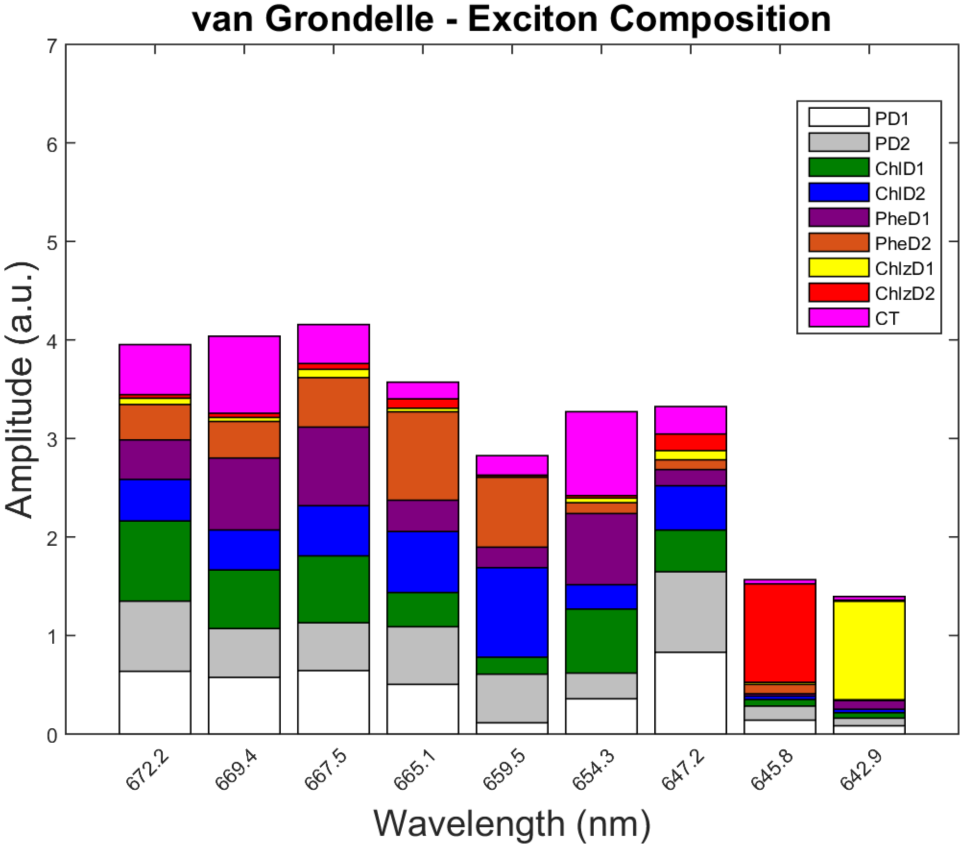

Figure 2.4: van Grondelle model excitons. Exciton transition energies (provided in wavelength on the x-axis) were calculated by diagonalizing the site-basis Hamiltonian in Table (2.1) using the red diagonal and purple coupling values. The square root of each element in the resulting amplitude matrix to find the contributing amplitude of each pigment for a given exciton. The total amplitude contribution from each pigment in an exciton is reflected in the height of each bar in the figure. Colors indicate the percent contribution of the corresponding pigment to that exciton.

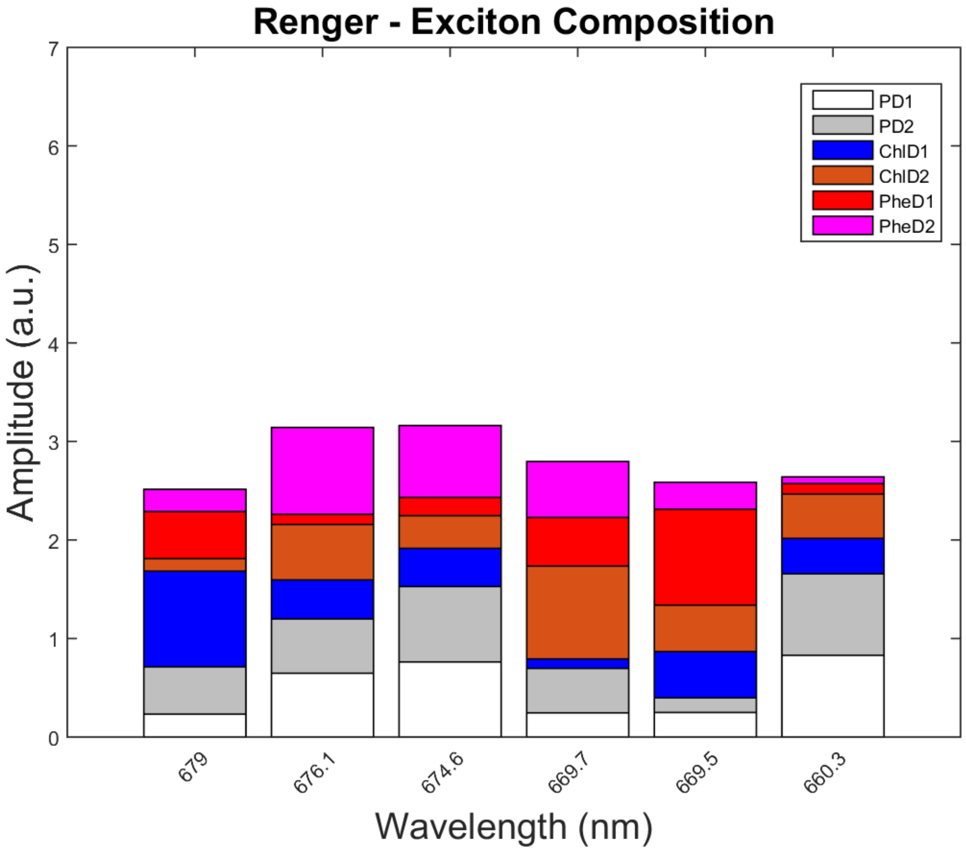

Figure 2.5: Renger model excitons. Exciton transition energies (provided in wavelength on the x-axis) were calculated by diagonalizing the site-basis Hamiltonian in Table (2.1) using the green diagonal and green coupling values. The square root of each element in the resulting amplitude matrix to find the contributing amplitude of each pigment for a given exciton. The total amplitude contribution from each pigment in an exciton is reflected in the height of each bar in the figure. Colors indicate the percent contribution of the corresponding pigment to that exciton.

CHAPTER 3

Two-Dimensional Electronic Spectroscopy

In this chapter I make the case for two-dimensional electronic spectroscopy (2DES) as a powerful spectroscopic technique for extracting rich information about the electronic structure and ultrafast dynamics of photosynthetic complexes. I use the density matrix formalism to derive the third order polarization signal measured in a 2DES experiment and an example of a possible third order response function that could be generated from a two-level system. Then, I explain the detection methods used to retrieve and enhance signal quality in 2DES experiments. Finally, I describe the tools used to perform the experiments and compare the box-CARS and Pump-Probe geometry methods used to collect the data presented in Chapters 4 and 5 of this thesis.

Due to the limited scope of this thesis, much of the theory behind 2DES and nonlinear spectroscopy is only briefly presented. For further details, the reader is directed to the following (non-exhaustive) list of texts on the subject: [35, 53–56].

3.1 Advantages of 2DES

Our interest in studying photosynthetic complexes, and specifically the PSII RC, is to understand how excitation energy is transferred across its molecular structure to establish a charge separation. The energetic state of the system can be probed via spectroscopic signatures (like ground state bleach, excited state absorption, and stimulated emission) that indicate the electronic structure of the system. Dynamics and kinetics can also be determined by adding a time-dependent element to the spectroscopic experiment. Extracting the richest information content from the system requires simultaneous high frequency and temporal resolution. Traditional spectroscopic tools offer either high frequency or high temporal resolution, not both. Ultrafast pump-probe experiments, for example, use laser pulses, compressed to have pulse widths in the picosecond (ps) to femtosecond (fs) regimes, to deliver coherent light pulses to interrogate the sample. High temporal resolution can be achieved by compressing a spectrally broad pulse, based on the time-bandwidth product [57]. The large frequency content of the pulse, however, restricts the frequency resolution. Similarly, a narrow spectral content (i.e., high spectral resolution) leads to temporally broad pulses.

As was presented in Chapter 1, the PSII RC suffers from a large degree of spectral congestion, particularly in the Q_y band of the chlorophyll and pheophytin pigments where all 8 core pigments absorb. Furthermore, because of the large network of pigments within a close spatial arrangement of each other, we wish to discern how the pigments are coupled to one another and their role in the charge separation process. 2DES is an experimental tool that surpasses the abilities of linear absorption and pump-probe and allows one to gain insight into the Q_y band electronic structure and charge separation process.

3.1.1 Pulse Interactions

A 2DES experiment utilizes three ultrafast laser pulses with carefully controlled inter-pulse timing to induce a third order polarization in the interrogated sample. A signal, containing information about the electronic structure of the material, then radiates off the sample in the direction determined by the phase-matching condition. Figure 3.1 is a schematic representation of a 2DES pulse sequence.

The first laser pulse incident on the system creates an electronic coherence within the sample at its resonant frequencies. A second pulse, some t_1 time later, generates an excited state or ground state population, which decays over the t_2 time frame until the arrival of the third pulse. This third pulse again creates a coherence in the system, which decays as a function of t_3. Signal following the third pulse can

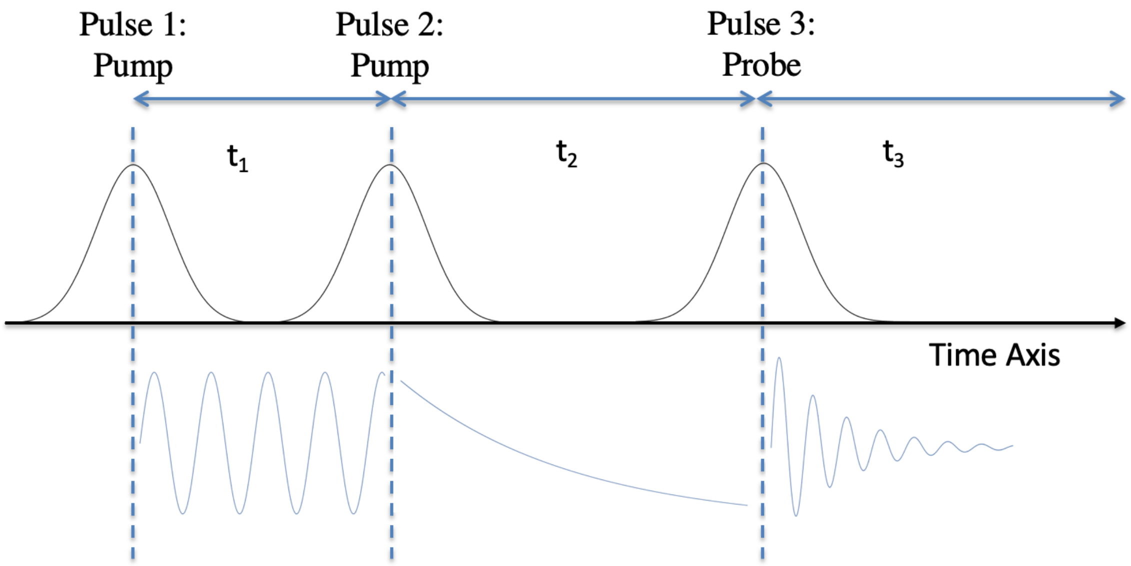

Figure 3.1: Three pulses in a 2DES experiment. The first pulse (pump) generates a coherent oscillation at the resonant frequencies in the sample over the t_1 time. The second pulse (pump) then creates an excited state population that decays over the t_2 time. Finally, the third pulse (probe) again creates a coherence, that radiates an electric-field which is heterodyne detected during time t_3.

be detected in the frequency domain with a spectrometer, defining an ω_3 (or ω_{det} detection frequency) axis. Similarly, a Fourier transform can be performed over the t_1 time frame to generate an ω_1 (or ω_{ex} excited frequency) axis that retains information on the initial resonant frequencies of the system. Using the these two frequency axes, a two-dimensional correlation plot of ω_{det} versus ω_{ex} can be generated at a series of t_2 waiting time points, thereby retaining a high frequency resolution of the system along two frequency axes with time resolution limited by the experimental pulse widths.

3.1.2 Information in 2DES

Figures (3.2) and (3.3) show cartoon representations of features that can appear in 2DES spectra [58]. The 2DES diagonal peak elongation indicates the degree of homogeneous and inhomogeneous broadening in the system. Because of the Fourier relationship between the state lifetimes (τ) and the measured transition frequency (ω_0): $\frac{1}{\tau} = \omega_0$ short lifetimes lead to a large degree of uncertainty in the measured frequency, thereby broadening the spectrum (Figure (3.4)). However, in condensed phase systems, lifetime broadening is usually small compared to the broadening caused by dynamic interactions between the system and its envrionment. These interactions, which alter the resonant frequency of the system, occur over a wide range of timescales. The most rapid of these, which are experienced by all the system components, lead to homogeneous broadening. Slower dynamics, such as protein motions and even static differences in the local environment due to the local protein structure, lead to inhomogeneous broadening. In a 2DES plot at early at early times, inhomogeneous broadening appears as elongation along the diagonal and homogeneous broadening as elongation along the anti-diagonal. This provides valuable information as to the underlying nature of the 2D lineshapes.

In 2DES spectra, resonant electronic transitions emerge as peaks on the diagonal. 2DES cross peaks indicate coupling and energy transfer between the transitions. When a photosynthetic system experiences energy transfer in the weak coupling limit features like those in Figure (3.2) emerge. In this case, at early times (i.e., $t_2 = 0$), only the resonant features appear elongated along the diagonal, indicating the presence of inhomogeneous broadening. At longer t_2 times a cross peak emerges at (ω_b,ω_a), indicating downhill energy transfer. In addition, the peaks become more rounded as the system experiences spectral diffusion.

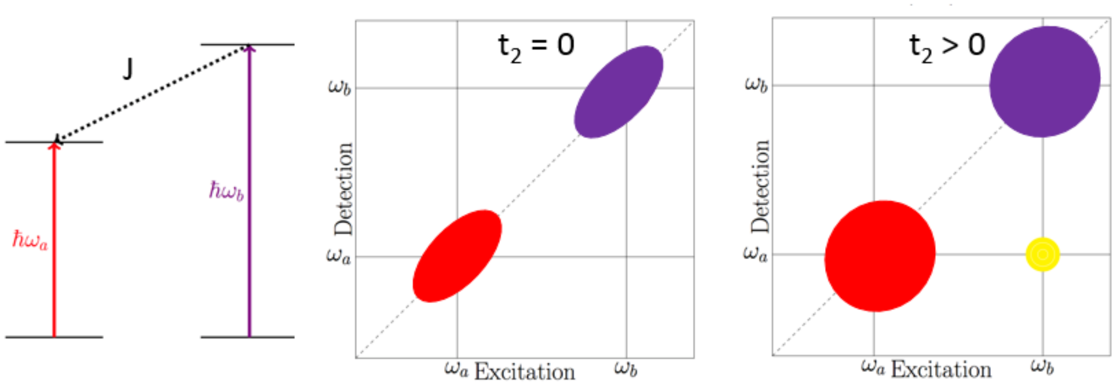

Figure 3.2: Weak (Förster) coupling.

In the strong coupling limit, on the other hand, features like those in Figure (3.3) emerge. In this case, two monomers can experience strong Coulombic coupling, such that excitation is highly delocalized over the two monomers creating a shared ground state. This leads to excitonic splitting, where the two new excited states are separated in energy in proportion to their coupling strength. 2DES features of this kind manifest as cross-peaks at (ω_b,ω_a) and (ω_a,ω_b) at early times that similarly experience spectral diffusion as t_2 increases.

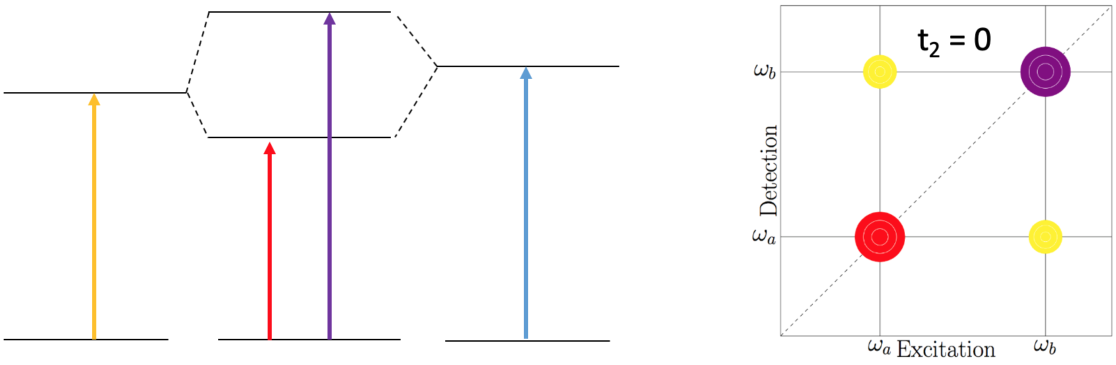

Figure 3.3: Strong (excitonic) coupling.

In summary, 2DES is a powerful tool for studying electronic structure and dynamical transfer processes in photosynthetic complexes and is the method used for studying the PSII RC as presented in this thesis. The next section details the theory behind generating a third order polarization in media and the means by which information is extracted from the interrogated system.

3.2 Third Order Response Functions in 2DES

3.2.1 The Density Matrix

We begin the discussion by first considering a two-level system with ground state $|0\rangle$ and excited state $|1\rangle$ that are separated by the energy gap $E_1 - E_0 = \hbar(\omega_1 - \omega_0) = \hbar\omega_{01}$. Assuming a time-independent Hamiltonian, this system can be represented as a superposition of the two states with the wavefunction $|\psi(\vec{r})\rangle$, where the contribution of each state is determined by the amplitudes $c_0^{'}$ and $c_1^{'}$:

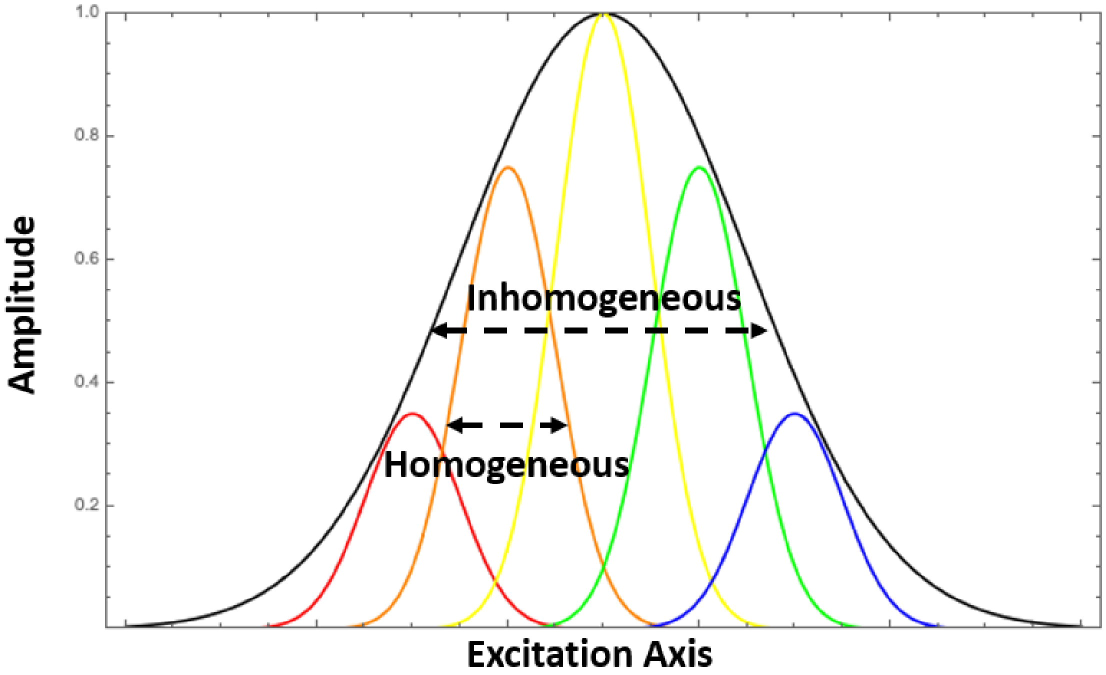

Figure 3.4: Gaussian line shapes can be broadened from homogeneous contributions, such as fast irreversible decay events, and from inhomogeneous contributions, such as local environment effects.

$$|\psi(\vec{r})\rangle = c_0^{'} |0\rangle + c_1^{'} |1\rangle \,. \tag{3.1}$$

We can account for the time evolution of the system by solving the time-dependent Schrödinger equation,

$$\frac{d}{dt} |\psi(\vec{r},t)\rangle = \frac{-i}{\hbar} \hat{H}_0 |\psi(\vec{r},t)\rangle \tag{3.2}$$

which, for a time-independent Hamiltonian H_0, has the solution

$$|\psi(\vec{r},t)\rangle = c_0^{'} e^{-i(E_0/\hbar)t} |0\rangle + c_1^{'} e^{-i(E_1/\hbar)t} |1\rangle \,. \tag{3.3}$$

Here we have used the eigenvalues of the time-independent Hamiltonian $\hat{H}_0 |n\rangle = E_n |n\rangle$, for which the energy can also be expressed as $E_n = \hbar\omega_n$ for state n.

For a perturbed system in the semi-classical representation, coherent laser light incident on the system changes the Hamiltonian to $\hat{H} = \hat{H}_0 + \hat{V}(t)$ for an interaction potential $\hat{V} = -\vec{\mu} \cdot \vec{E}(t)$. Here, the terms of the interaction involve the dipole moment operator $\vec{\mu}$ and the electric field of the incident laser source $\vec{E}(t)$. This perturbation from the light source couples the two states of the system so the stationary probability amplitudes $c_n^{'}$ acquire a time dependence $c_n^{'}(t)$.

Accounting for the excited system's time-dependent amplitudes the wavefunction becomes:

$$|\psi(\vec{r},t)\rangle = c_0^{'}(t)e^{-i\omega_0 t}|0\rangle + c_1^{'}(t)e^{-i\omega_1 t}|1\rangle . \tag{3.4}$$

The explicit expressions for the time dependent amplitudes are obtained by using Equation (3.4) in the time-dependent Schrödinger equation. The result is the following set of coupled differential equations:

$$\begin{aligned} i\hbar\frac{d}{dt}c_0^{'}(t) &= c_1^{'}(t)\vec{E}(t)\cdot\vec{\mu}_{10}e^{-i\omega_{01}t} \\ i\hbar\frac{d}{dt}c_1^{'}(t) &= c_0^{'}(t)\vec{E}(t)\cdot\vec{\mu}_{01}e^{i\omega_{01}t}. \end{aligned} \tag{3.5}$$

where $\vec{\mu}_{10} = \langle 1|\,\vec{\mu}\,|0\rangle$ and $\vec{\mu}_{01} = \langle 0|\,\vec{\mu}\,|1\rangle$ are the transition dipole matrix elements and $\vec{E}(t) = \vec{E}_0 cos(\omega t)$ is the electric field of the laser source. Light incident on the system induces a macroscopic polarization, which is the sum of all the individual dipoles created from the electric field of the incident light acting on the system. The macroscopic polarization can be found by evaluating the expectation value of $\vec{\mu}$:

$$\vec{P}(t) = \langle\psi(\vec{r},t)|\,\vec{\mu}\,|\psi(\vec{r},t)\rangle . \tag{3.6}$$

Modeling a system using wavefunctions becomes impractical when considering multi-state systems governed by statistical ensembles and interaction with a thermal bath. Information about the time-dependent evolution of a system can be handled more readily using the density matrix formalism.

To use the density matrix formalism, we first define the density matrix operator as the outer product of the wavefunction kets:

$$\rho = |\psi\rangle \langle\psi| \tag{3.7}$$

The above definition is for the case when the system is in a pure state, which is when the system can be defined by a single wavefunction. The true power of the density matrix formalism is realized when it is extended to apply to ensembles mixed states. In an ensemble the system is composed of j molecules with probability P_j of being in state $|\psi_j\rangle$, such that $\rho = \sum_j P_j |\psi_j\rangle \langle\psi_j|$. Traditional ket notation is unable to account for the simultaneous conditions of multiple pure state systems. However, for the sake of simplicity, we only consider the pure state case.

In the pure state case, the definition of the density matrix operator can be rewritten in the eigenstate basis in the following way:

$$\begin{aligned}\rho &= |\psi\rangle \langle\psi| \\ &= \left(\sum_n c_n(t) |n\rangle\right) \left(\sum_m c_m^*(t) \langle m|\right) \\ &= \sum_{nm} c_n(t) c_m^*(t) |n\rangle \langle m|\end{aligned} \tag{3.8}$$

For our two-level system, the density matrix operator can be used to construct the density matrix ρ_{nm}:

$$\begin{aligned}
&\begin{bmatrix} \langle 0|\,\rho\,|0\rangle & \langle 0|\,\rho\,|1\rangle \\ \\ \langle 1|\,\rho\,|0\rangle & \langle 1|\,\rho\,|1\rangle \end{bmatrix} \\
&= \begin{bmatrix} \rho_{00} & \rho_{01} \\ \\ \rho_{10} & \rho_{11} \end{bmatrix} \\
&= \begin{bmatrix} c_0(t)c_0^*(t) & c_0(t)c_1^*(t) \\ \\ c_1(t)c_0^*(t) & c_1(t)c_1^*(t) \end{bmatrix} \\
&= \begin{bmatrix} \left(c_0^{'}(t)e^{-i\omega_0 t}\right)\left(c_0^{'*}(t)e^{i\omega_0 t}\right) & \left(c_0^{'}(t)e^{-i\omega_0 t}\right)\left(c_1^{'*}(t)e^{i\omega_1 t}\right) \\ \\ \left(c_1^{'}(t)e^{-i\omega_1 t}\right)\left(c_0^{'*}(t)e^{i\omega_0 t}\right) & \left(c_1^{'}(t)e^{-i\omega_1 t}\right)\left(c_1^{'*}(t)e^{i\omega_1 t}\right) \end{bmatrix} \\
&= \begin{bmatrix} \left|c_0^{'}(t)\right|^2 & c_0^{'}(t)c_1^{'*}(t)e^{i\omega_{01} t} \\ \\ c_1^{'}(t)c_0^{'*}(t)e^{-i\omega_{01} t} & \left|c_1^{'}(t)\right|^2 \end{bmatrix}
\end{aligned} \tag{3.9}$$

where the final values use the amplitude expressions from Equation (3.4) and can be found in their explicit form by integrating the differential equations of Equation (3.5). In Equation (3.8) the diagonal elements of the density matrix describe the population of the system, while the anti-diagonal elements are the coupled coherences.

3.2.2 Density Matrix Dynamics

Now that we have an explicit form for the elements of the density matrix, we can use it to model system dynamics in a similar fashion as we would using the wavefunction.

To find the density matrix equivalent form of the time-dependent Schrödinger equation we take the derivative of the density matrix operator with respect to time.

$$\begin{aligned}\frac{d}{dt}\rho &= \frac{d}{dt}\left(\left|\psi\right\rangle\left\langle\psi\right|\right)\\ &= \left(\frac{d}{dt}\left|\psi\right\rangle\right)\left\langle\psi\right| + \left|\psi\right\rangle\left(\frac{d}{dt}\left\langle\psi\right|\right)\\ &= \frac{-i}{\hbar}\left(\hat{H}\left|\psi\right\rangle\right)\left\langle\psi\right| - \frac{-i}{\hbar}\left|\psi\right\rangle\left(\left\langle\psi\right|\hat{H}\right)\\ &= \frac{-i}{\hbar}\left(\hat{H}\left|\psi\right\rangle\left\langle\psi\right| - \left|\psi\right\rangle\left\langle\psi\right|\hat{H}\right)\\ &= \frac{-i}{\hbar}\left[\hat{H},\rho\right].\end{aligned} \tag{3.10}$$

Individual density matrix elements are found from:

$$\frac{d}{dt}\rho_{nm} = \frac{-i}{\hbar}\left[\hat{H},\rho\right]_{nm} \tag{3.11}$$

This result is called the Liouville-von Neumann equation.

Now, we consider the form of the macroscopic polarization using the density matrix formalism. From Equation (3.6) we know that the polarization is the expectation value of the dipole operator, which can be expanded as follows:

$$\begin{aligned}\vec{P} &= \left\langle\psi\right|\vec{\mu}\left|\psi\right\rangle\\ &= \left(\sum_m c_m^*(t)\left\langle m\right|\right)\vec{\mu}\left(\sum_n c_n(t)\left|n\right\rangle\right)\\ &= \sum_{mn} c_m^*(t)c_n(t)\left\langle m\right|\vec{\mu}\left|n\right\rangle\\ &= \sum_{mn}\rho_{nm}\vec{\mu}_{mn}\\ &= Tr\left(\rho\vec{\mu}\right).\end{aligned} \tag{3.12}$$

Thus the polarization using the density matrix is the trace of the product of the density matrix and the dipole operator. The dipole operator is an off-diagonal matrix given by:

$$\hat{\mu} = \begin{bmatrix} 0 & \hat{\mu}_{01} \\ \hat{\mu}_{01}^{*} & 0 \end{bmatrix}. \tag{3.13}$$

Until this point we have only considered the system to be in the Schrödinger picture where the time evolution is only on the wavefunction and any operators are time independent. We can also consider the system in the interaction picture where both the wavefunction and operator experience time evolution. In the interaction picture, any time evolution is also due solely to the light-matter interaction and not the inherent energies described by the time independent system Hamiltonian $\hat{H}_0$. Wavefunctions in the interaction picture are expressed as follows, where the subscript S denotes the Schrödinger picture and I denotes the interaction picture:

$$|\psi_I(t)\rangle = e^{\frac{i}{\hbar}\hat{H}_0(t-t_0)} |\psi_S(t)\rangle . \tag{3.14}$$

Here we have introduced $\hat{U}_0^{\dagger}(t,t_0) = e^{\frac{i}{\hbar}\hat{H}_0(t-t_0)}$, the Hermitian conjugate to the time evolution operator $\hat{U}_0(t,t_0) = e^{-\frac{i}{\hbar}\hat{H}_0(t-t_0)}$. In the interaction picture, the dipole operator becomes:

$$\begin{aligned} \hat{\mu}_I(t) &= \hat{U}_0^{\dagger}(t,t_0)\hat{\mu}\hat{U}_0(t,t_0) \\ &= e^{\frac{i}{\hbar}\hat{H}_0(t-t_0)}\hat{\mu}e^{-\frac{i}{\hbar}\hat{H}_0(t-t_0)} \end{aligned} \tag{3.15}$$

and the light-matter interaction Hamiltonian is:

$$\begin{aligned} \hat{V}_I(t) &= \hat{U}_0^{\dagger}(t,t_0)\hat{V}(t)\hat{U}_0(t,t_0) \\ &= e^{\frac{i}{\hbar}\hat{H}_0(t-t_0)}\vec{\mu}\cdot\vec{E}(t)e^{-\frac{i}{\hbar}\hat{H}_0(t-t_0)} \\ &= \left(e^{\frac{i}{\hbar}\hat{H}_0(t-t_0)}\vec{\mu}e^{-\frac{i}{\hbar}\hat{H}_0(t-t_0)}\right)\cdot\vec{E}(t) \\ &= \hat{\mu}_I(t)E(t). \end{aligned} \tag{3.16}$$

In the interest of simplicity, the dot product and vectorial nature of the electric field have been dropped in the final expression above. We can define the Liouville-von Neumann equation in the interaction picture as in expressed in Equation (3.17). Note that actions on the density matrix are for specific elements, but we drop the element notation in order to focus on how the light-matter interactions influence the density matrix in a general manner.

$$\frac{d}{dt}\rho_I(t) = -\frac{i}{\hbar}\left[\hat{V}_I(t),\rho_I(t_0)\right]. \tag{3.17}$$

If we assume the light-matter interaction to be weak, the density matrix can be expanded as a power series $\rho_I(t) = \rho_I^{(0)}(t) + \rho_I^{(1)}(t) + \rho_I^{(2)}(t) + \rho_I^{(3)}(t) + \ldots$ and the contributions from higher order terms can be solved iteratively using Equation (3.17). The first order contribution therefore looks like:

$$\begin{aligned} \rho_I^{(1)}(t) &= -\frac{i}{\hbar}\int_{t_0}^{t} dt_1^{'}\left[\hat{V}_I(t_1^{'}),\rho_I^{(0)}(t_0)\right] \\ &= -\frac{i}{\hbar}\int_{t_0}^{t} dt_1^{'}E(t_1^{'})\left[\hat{\mu}_I(t_1^{'}),\rho_I^{(0)}(t_0)\right] \end{aligned} \tag{3.18}$$

At this point it is also important to take note of the time dependence, which can be better understood by consulting Figure (3.5). $\rho_I^{(0)}(t)$ is the density matrix at some initial time, assumed to be at equilibrium and evolving as it would without perturbation. From here on this term will be expressed simply as $\hat{\rho}_0$. By introducing a light-matter interaction into the system at some time point t_1, the first order contribution to the density matrix term can exist at any time after t_1, and the integration is then performed over all times $dt_1^{'}$. Figure (3.5) shows $dt_1^{'}$ to be from $-\infty$ to the point of measure t. However, by the conditions of causality, where the signal cannot precede the stimulus, the signal can only exist between the interval defined by the stimulus t_1 and the point at which the signal is measured t.

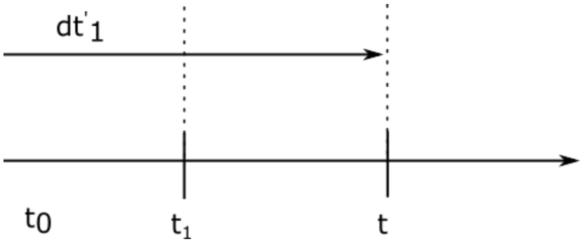

Figure 3.5: An illustration of the time dependence for the first order density matrix. t_0 denotes times when the system is in the steady state, t_1 is the point in time at which the pulse interacts with the system, t is the time at which a measurement is made, and the integration is performed over $dt_1^{'}$.

Iterating Equation (3.17) to account for three perturbations, the third order contribution to the density matrix is found to be:

$$\rho_I^{(3)}(t) = \left(\frac{-i}{\hbar}\right)^3 \int_{t_0}^{t} dt_3^{'} \int_{t_0}^{t_3} dt_2^{'} \int_{t_0}^{t_2} dt_1^{'} E_3(t_3^{'}) E_2(t_2^{'}) E_1(t_1^{'}) \times \left[\hat{\mu}_I(t_3^{'}), \left[\hat{\mu}_I(t_2^{'}), \left[\hat{\mu}_I(t_1^{'}), \hat{\rho}_0\right]\right]\right] \tag{3.19}$$

where $E_1(t_1^{'})$, $E_2(t_2^{'})$ and $E_3(t_3^{'})$ are the fields for the first, second, and third pulses, respectively. The time dependence on the third order contribution of the density matrix can be understood by consulting Figure (3.6). Similar to the first order contribution, the third order contribution can only exist following the final pulse at $t_3^{'}$ and is measured at t.

Following the results of Equation (3.12), the third order contribution of the density matrix is multiplied by a fourth signal transition dipole moment term and the trace is taken to obtain the third order polarization:

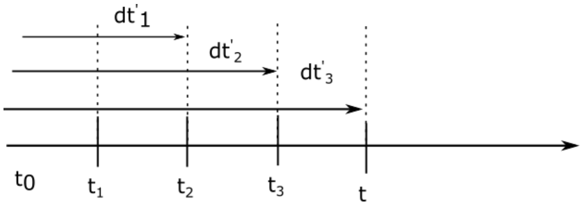

Figure 3.6: An illustration of the time dependence for the third order density matrix. t_1, t_2, and t_3 are the absolute times at which the first, second, and third pulses interact, respectively. $dt_1^{'}$, $dt_2^{'}$, and $dt_3^{'}$ are the times over which the first, second, and third order contributions are integrated, respectively.

$$\begin{aligned} P^{(3)}(t) = \left(\frac{-i}{\hbar}\right)^3 \int_{t_0}^{t} dt_3^{'} \int_{t_0}^{t_3} dt_2^{'} \int_{t_0}^{t_2} dt_1^{'} E_3(t_3^{'}) E_2(t_2^{'}) E_1(t_1^{'}) \times \\ Tr\{\hat{\mu}_I(t)\left[\hat{\mu}_I(t_3^{'}), \left[\hat{\mu}_I(t_2^{'}), \left[\hat{\mu}_I(t_1^{'}), \hat{\rho}_0\right]\right]\right]\}. \end{aligned} \tag{3.20}$$

Here, by taking advantage of the commutator identity $[A,[B,C]] = [[A,B],C]$ and using the invariance of cyclic permutations under the trace, the term in the trace can be rearranged as follows:

$$\begin{aligned} & Tr\{\hat{\mu}_I(t)\left[\hat{\mu}_I(t_3^{'}), \left[\hat{\mu}_I(t_2^{'}), \left[\hat{\mu}_I(t_1^{'}), \hat{\rho}_0\right]\right]\right]\} \\ & = Tr\{\left[\left[\left[\hat{\mu}_I(t), \hat{\mu}_I(t_3^{'})\right], \hat{\mu}_I(t_2^{'})\right], \hat{\mu}(t_1^{'})\right]\hat{\rho}_0\}. \end{aligned} \tag{3.21}$$

It now becomes convenient to change how the time dependence is defined in the polarization. Until this point, the $t_1^{'}$, $t_2^{'}$ and $t_3^{'}$ times have been used to represent absolute time values. Instead, we now define time intervals between the pulses as $\tau_1 = t_2 - t_1$, $\tau_2 = t_3 - t_2$ and $\tau_3 = t - t_3$ (Figure (3.7)), and consider how the system evolves over these time intervals. This is applied to $P^{(3)}$ by implementing a change of variables and considering the limit where $t_0 \to -\infty$.

Addressing the limits of integration for the integral over $t_1^{'}$, we are now interested in the time interval $\tau_1 = t_2 - t_1$. Applying this to the upper and lower bounds of the integration, the upper bound is now $\tau_1^{upper} = t_2 - t_2 = 0$ and the lower bound is $\tau_1^{lower} = t_2 - (-\infty) = \infty$. The integration variable becomes $d\tau_1 = -dt_1$ and the form

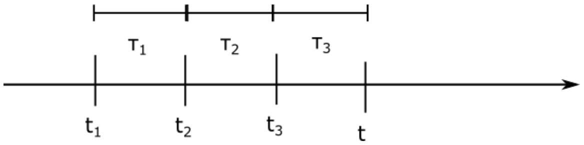

Figure 3.7: An illustration of the time intervals created by the pulses.

of the integral is thus $\int_{t_0}^{t_2} dt_1 \rightarrow \int_{\infty}^{0} -d\tau_1 = \int_{0}^{\infty} d\tau_1$. A similar change is applied to the other integrals and the third order polarization becomes:

$$\begin{aligned} P^{(3)}(t) = \left(\frac{-i}{\hbar}\right)^3 \int_0^\infty d\tau_3 \int_0^\infty d\tau_2 \int_0^\infty d\tau_1 E_3(t-\tau_3)E_2(t-\tau_2-\tau_1)\times \\ E_1(t-\tau_1-\tau_2-\tau_3)Tr\{[[[\hat{\mu}_I(\tau_3+\tau_2+\tau_1),\hat{\mu}_I(\tau_2+\tau_3)],\hat{\mu}_I(\tau_1)],\hat{\mu}(0)]\,\hat{\rho}_0\}. \end{aligned} \tag{3.22}$$

Here the time dependence on the dipole moments is such that the first interaction $\hat{\mu}_I(0)$ acts on the steady state density matrix and therefore has not yet acquired any time evolution. Subsequently, the second pulse occurs after the system has evolved over τ_1, the third pulse after $\tau_1 + \tau_2$, and the final interaction over $\tau_1 + \tau_2 + \tau_3$. The terms within the trace thus show the accumulated time evolution on the density matrix. This is then convolved with the electric fields from each pulse interaction.

3.2.3 Third Order Response Functions

Using the shorthand $\hat{\mu}_I(\tau_3+\tau_2+\tau_1) = \hat{\mu}_4(t)$, $\hat{\mu}_I(\tau_2+\tau_1) = \hat{\mu}_3(t)$, $\hat{\mu}_I(\tau_1) = \hat{\mu}_2(t)$, and $\hat{\mu}_I(0) = \hat{\mu}_1(t)$, we can now define the third order response function as:

$$R^{(3)} = \left(\frac{-i}{\hbar}\right)^3 Tr\{[[[\hat{\mu}_4(t),\hat{\mu}_3(t)],\hat{\mu}_2(t)],\hat{\mu}_1(t)]\,\hat{\rho}_0\}. \tag{3.23}$$

Expanding the nested commutators for a two-level system, the third order polarization has eight possible terms. Using the invariance of cyclic permutations under the trace so that $\hat{\rho}_0$ is positioned next to $\hat{\mu}_1(t)$, the response functions are thus defined as follows (using the labeling convention of Andrei Tokmakoff [55]):

$$\left(-\frac{i}{\hbar}\right)^3 Tr\{\hat{\mu}_4(t)\hat{\mu}_3(t)\hat{\mu}_2(t)\hat{\mu}_1(t)\hat{\rho}_0\} - Tr\{\hat{\rho}_0\hat{\mu}_1(t)\hat{\mu}_2(t)\hat{\mu}_3(t)\hat{\mu}_4(t)\} = R_1^{(3)} + R_1^{*(3)} \tag{3.24}$$

$$\left(-\frac{i}{\hbar}\right)^3 Tr\{\hat{\mu}_4(t)\hat{\mu}_2(t)\hat{\rho}_0\hat{\mu}_1(t)\hat{\mu}_3(t)\} - Tr\{\hat{\mu}_3(t)\hat{\mu}_1(t)\hat{\rho}_0\hat{\mu}_2(t)\hat{\mu}_4(t)\} = R_2^{(3)} + R_2^{*(3)} \tag{3.25}$$

$$\left(-\frac{i}{\hbar}\right)^3 Tr\{\hat{\mu}_4(t)\hat{\mu}_3(t)\hat{\rho}_0\hat{\mu}_1(t)\hat{\mu}_2(t)\} - Tr\{\hat{\mu}_2(t)\hat{\mu}_1(t)\hat{\rho}_0\hat{\mu}_3(t)\hat{\mu}_4(t)\} = R_3^{(3)} + R_3^{*(3)} \tag{3.26}$$

$$\left(-\frac{i}{\hbar}\right)^3 Tr\{\hat{\mu}_4(t)\hat{\mu}_1(t)\hat{\rho}_0\hat{\mu}_2(t)\hat{\mu}_3(t)\} - Tr\{\hat{\mu}_3(t)\hat{\mu}_2(t)\hat{\rho}_0\hat{\mu}_1(t)\hat{\mu}_3(t)\} = R_4^{(3)} + R_4^{*(3)} \tag{3.27}$$

It should be noted that because the density matrix is an outer product, left and right operations are complex conjugates of each other. Therefore, the sequence of the interaction must be preserved. In this way, an interaction on the right is a "bra" interaction, while an interaction on the left is a "ket" interaction.

To better understand the intricacies of the response functions, the $R_2^{(3)}$ expression of Equation (3.25) is expanded below. In the interest of being explicit, time evolution operator terms like $\hat{U}_0(\tau_3{+}\tau_2{+}\tau_1)$ are expanded and expressed as their mathematically equivalent product $\hat{U}_0(\tau_3)\hat{U}_0(\tau_2)\hat{U}_0(\tau_1)$.

$$\begin{gathered} R_2^{(3)} = \left(-\frac{i}{\hbar}\right)^3 Tr\{\hat{\mu}_4(t)\hat{\mu}_2(t)\hat{\rho}_0\hat{\mu}_1(t)\hat{\mu}_3(t)\} \\ = \left(-\frac{i}{\hbar}\right)^3 Tr\{\hat{U}_0^\dagger(\tau_3)\hat{U}_0^\dagger(\tau_2)\hat{U}_0^\dagger(\tau_1)\hat{\mu}_4\hat{U}_0(\tau_3)\hat{U}_0(\tau_2)\hat{U}_0(\tau_1)U_0^\dagger(\tau_1)\hat{\mu}_2 U_0(\tau_1)\hat{\rho}_0\hat{\mu}_1\times \\ \hat{U}_0^\dagger(\tau_2)U_0^\dagger(\tau_1)\hat{\mu}_3\hat{U}_0(\tau_2)\hat{U}_0(\tau_1)\} \end{gathered} \tag{3.28}$$

Removing the adjacent complex conjugate pairs like $\hat{U}_0(\tau_1)U_0^\dagger(\tau_1)$, including pairs that emerge from cyclic permutations results in:

$$R_2^{(3)} = \left(-\frac{i}{\hbar}\right)^3 Tr\{\hat{\mu}_4 \underbrace{\hat{U}_0(\tau_3)\underbrace{\hat{U}_0(\tau_2)\hat{\mu}_2\underbrace{\hat{U}_0(\tau_1)\hat{\rho}_0\hat{\mu}_1\hat{U}_0^\dagger(\tau_1)}_{\text{Pulse 1}}U_0^\dagger(\tau_2)}_{\text{Pulse 2}}\hat{\mu}_3\hat{U}_0^\dagger(\tau_3)}_{\text{Pulse 3}}\}. \tag{3.29}$$

Here the $\hat{\rho}_0\hat{\mu}_1$ term is sandwiched between $\hat{U}_0(\tau_1)$ on the left and $\hat{U}_0^\dagger(\tau_1)$ on the right. This is interpreted as the density matrix being perturbed from equilibrium by a bra interaction, which then evolves over the τ_1 time interval. The resulting term then experiences a ket interaction from $\hat{\mu}_2$ and evolves over τ_2. This is followed by another bra interaction from $\hat{\mu}_3$ that evolves over τ_3. Finally, the system emits signal from the ket side with the $\hat{\mu}_4$ interaction.

Considering Equation (3.29) in matrix form and assuming the system is initially in the ground state (i.e., $\rho_{00} = 1$), the expression below is obtained.

$$R_2^{(3)} = \left(-\frac{i}{\hbar}\right)^3 \times$$

$$Tr\{\begin{bmatrix} 0 & \hat{\mu}_4 \\ \hat{\mu}_4^* & 0 \end{bmatrix} e^{-\frac{i}{\hbar}\hat{H}_0\tau_3} e^{-\frac{i}{\hbar}\hat{H}_0\tau_2} \begin{bmatrix} 0 & \hat{\mu}_2 \\ \hat{\mu}_2^* & 0 \end{bmatrix} e^{-\frac{i}{\hbar}\hat{H}_0\tau_1} \begin{bmatrix} 1 & 0 \\ 0 & 0 \end{bmatrix} \begin{bmatrix} 0 & \hat{\mu}_1 \\ \hat{\mu}_1^* & 0 \end{bmatrix} e^{\frac{i}{\hbar}\hat{H}_0\tau_1} e^{\frac{i}{\hbar}\hat{H}_0\tau_2} \times$$

$$\begin{bmatrix} 0 & \hat{\mu}_3 \\ \hat{\mu}_3^* & 0 \end{bmatrix} e^{\frac{i}{\hbar}\hat{H}_0\tau_3}\}$$

Multiplying the matrices for $\hat{\rho}_0\hat{\mu}_1$ and recalling the form of the dipole operator from Equation (3.13), the first interaction will result in the coherence $\hat{\mu}_1 |0\rangle \langle 1|$, which evolves over τ_1. Including the time evolution terms, this takes the form $\hat{\mu}_1 e^{-\frac{i}{\hbar}\hat{H}_0\tau_1} |0\rangle \langle 1| e^{\frac{i}{\hbar}\hat{H}_0\tau_1}$. An exponential function of an operator acting on an eigenvector is equivalent to an exponential function of that eigenvalues of the operator, so this term becomes $\hat{\mu_1} e^{-i\omega_0 \tau_1} |0\rangle \langle 1| e^{i\omega_1 \hat{H}_s \tau_1} = \hat{\mu_1} |0\rangle \langle 1| e^{i\omega_{01}\tau_1}$. It is therefore evident that the system evolves as a coherence with a frequency of ω_{01} over the τ_1 time interval. The second interaction puts the system in an excited state population $|1\rangle \langle 1|$. Evaluating the time dependence here results in $\hat{\mu_2}^* \hat{\mu_1} |1\rangle \langle 1| e^{-i\omega_1 \tau_2} e^{i\omega_1 \tau_2}$ and the oscillations over the τ_2 time interval cancel. The third interaction again results in a coherence with a frequency of $-\omega_{01}$ over the τ_3 time interval. Finally, the fourth interaction returns the system to the ground state and a signal is emitted. The end result is thus:

$$R_2^{(3)} = \left(-\frac{i}{\hbar}\right)^3 Tr\{ \begin{bmatrix} \hat{\mu}_4 \hat{\mu}_2^* \hat{\mu}_1 \hat{\mu}_3^* & 0 \\ & \\ 0 & 0 \end{bmatrix} e^{-i\omega_{01}\tau_3} e^{i\omega_{01}\tau_1} \}$$

$$= \left(-\frac{i}{\hbar}\right)^3 \hat{\mu}_4 \hat{\mu}_2^* \hat{\mu}_1 \hat{\mu}_3^* e^{-i\omega_{01}\tau_3} e^{i\omega_{01}\tau_1}.$$

This signal is called a rephasing signal since the signs of the argument in the exponents over the τ_1 and τ_3 signals are opposite from each other and will therefore produce a rephasing photon echo signal.

Double-sided Feynman diagrams, like that in Figure (3.8), are often used as a visual aid to track the state of the density matrix over the sequence of interactions. The diagrams are read from bottom to top, following the progression of time. Each cell of the diagram shows the density matrix term that evolves over the indicated time interval. Solid arrows indicate the wavevector interaction from the incident electric field on the sample and dashed arrows indicate the signal emission. Wavevectors pointing up and to the left are negative, while those pointing up and to the right are positive. A wavevector pointing into the diagram represents an absorption event, while one pointing away is an emission event. Figure (3.8) shows the double-sided Feynman diagram for the rephasing $R_2^{(3)}$ signal derived above. Recall that the final expression was obtained following a bra, ket, bra, ket interaction sequence, as is clearly shown in Figure (3.8). All of the remaining third order response functions detailed in Equations (3.25) - (3.27) can be solved in a similar manner and each has its own distinct double-sided Feynman diagram.

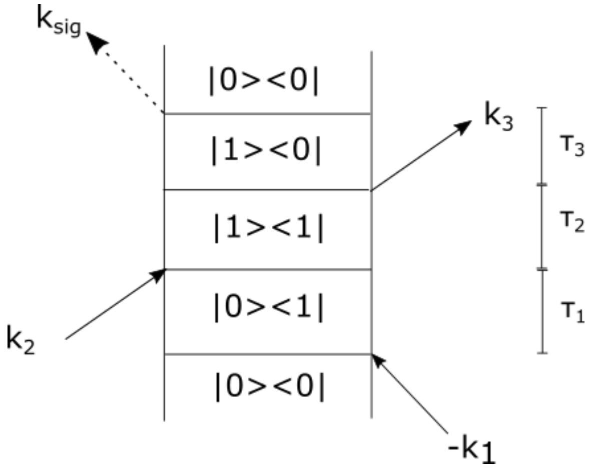

Figure 3.8: Double-sided Feynman diagram for the $R_2^{(3)}$ rephasing pathway.k_1, k_2 and k_3 are the wavevectors of the electric fields contained within the $E_1(t-\tau_1-\tau_2-\tau_3)$, $E_2(t-\tau_2-\tau_3)$, $E_3(t-\tau_3)$ terms.

3.3 2DES Experimental Geometries Since its first demonstration by the Jonas group [59, 60], a number of different experimental implementations of 2DES have been developed. These were recently reviewed by Fuller and Ogilvie [61]. The work presented in this thesis uses both the box-CARS and pump-probe geometry, reviewed briefly here.

3.3.1 Box-CARS Geometry

Phase Matching - The box-CARS geometry has the advantage of being a background-free geometry. This means the wavevectors are spatially manipulated such that third order polarization signal emerges in a unique direction without contributions from the exciting pulses. Experiments performed in the box-CARS geometry presented in this thesis accomplish this using a diffractive optic in a 4-f focusing geometry on which both the pump and probe beams are focused [14]. Diffracted orders are spatially filtered such that the pump +1 and -1 orders, as well as the probe +1 and +3 orders focus on the sample.

By the phase-matching condition the rephasing signal ($\vec{k}_R = -\vec{k}_1 + \vec{k}_2 + \vec{k}_3$) and non-rephasing signal ($\vec{k}_{NR} = +\vec{k}_1 - \vec{k}_2 + \vec{k}_3$) emerge in opposite directions due to the sign of the wavevector on the first ($\vec{k}_1$) and second ($\vec{k}_2$) pulses. This presents a problem as it would require detection at two different spatial locations to recover the full absorptive information. A common solution is to perform the experiment twice, flipping the time ordering of $\vec{k}_1$ and $\vec{k}_2$ to generate the rephasing and non-rephasing signals, but maintaining the vectoral relationship between the beams so that the emitted signal is in the same direction for both signal types. Additionally, in this setup, diffracted orders contain pulse pairs generated with precise inter-pulse timing by a Dazzler acousto-optic modulator. This allows for simultaneous measurement of both the rephasing and non-rephasing signal at each t_2 delay point [14].

The emitted signal is collected collinearly with a fourth pulse, attenuated by an etched mirror, that is delayed from signal by 800 fs and acts as a local oscillator (LO) to enable heterodyne detection. Measurements made by the camera in the spectrometer measure the intensity of the interference between the LO and signal fields. Signal containing the relative phase relationship $\phi_{sig} - \phi_{LO}$ can be recovered by Fourier transforming over the interference and multiplying by a windowing function around the peak with the correct frequency (also known as spectral interferometry) [62, 63]. However, there is ambiguity in the global phase of the extracted signal, making it difficult to separate dispersive and absorptive 2DES signals. This problem can be overcome by taking advantage of the projection-slice theorem [35], which says that a projection of the ω_{ex} axis along the diagonal of a 2D plot reproduces a pump-probe spectrum. By fitting this generated 2D plot with a transient absorption measurement taken at the same t_2 delay value, we can perform the following minimization that retrieves the global phase as a function of frequency ($\theta(\omega)$) [14]:

$$min\{|TG(\omega)|cos(\phi_{TG}(\omega) + \theta(\omega)) - \alpha PP(\omega)\}^2 \tag{3.30}$$

where $TG(\omega)$ and $PP(\omega)$ are the frequency resolved transient grating (where $t_1 =$

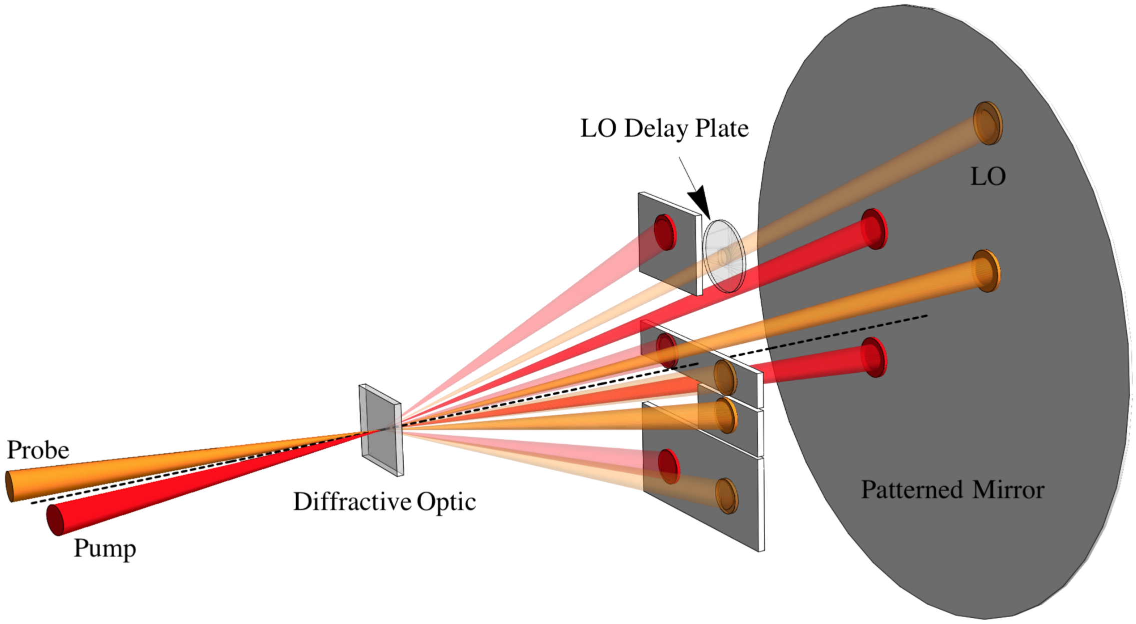

Figure 3.9: Beam geometries generated by a diffractive optic. Image from [13].

0) and pump-probe spectra, respectively, α is a scaling constant, and $\phi_{TG}(\omega)$ is the phase of the transient grating signal.

Phase Cycling - In the heterodyne detected box-CARS setup there are still a number of signals that must be separated from the desired 2DES signal. In addition, each complete 2D pulse train involves 4 pump pulses that need to be resolved into their respective rephasing and nonrephasing contributions. Moreover, transient grating measurements must also be made to solve the global phasing problem. Each of these issues can be resolved simultaneously by implementing a phase cycling scheme that solves the following system of equations:

$$\begin{bmatrix} S_1 \\ S_2 \\ S_3 \end{bmatrix} = \begin{bmatrix} e^{i(y_1-x_1)} & e^{i(x_1-y_1)} & 1 \\ e^{i(y_2-x_2)} & e^{i(x_2-y_2)} & 1 \\ e^{i(y_3-x_3)} & e^{i(x_3-y_3)} & 1 \end{bmatrix} \begin{bmatrix} S_R \\ S_{NR} \\ S_{TG} \end{bmatrix} \tag{3.31}$$

for three independent measurements S_1, S_2, and S_3 of the rephasing (S_R), non-rephasing (S_{NR}), and transient grating (S_{TG}) spectra. This system of equations is solved with the 6-step phase sequence:

$$\{(x_1, y_1), (x_2, y_2), (x_3, y_3)\} = \left\{(0, 0), (0, \frac{2\pi}{3}), (0, \frac{4\pi}{3})\right\}. \tag{3.32}$$

Considering all this information together, this means that for every t_2 delay time point we use the Dazzler to control both the inter-pulse timing and phase values to take six measurements that can separate out rephasing, non-rephasing, and transient grating spectra, as well as remove excess scattering terms that contribute to noise.

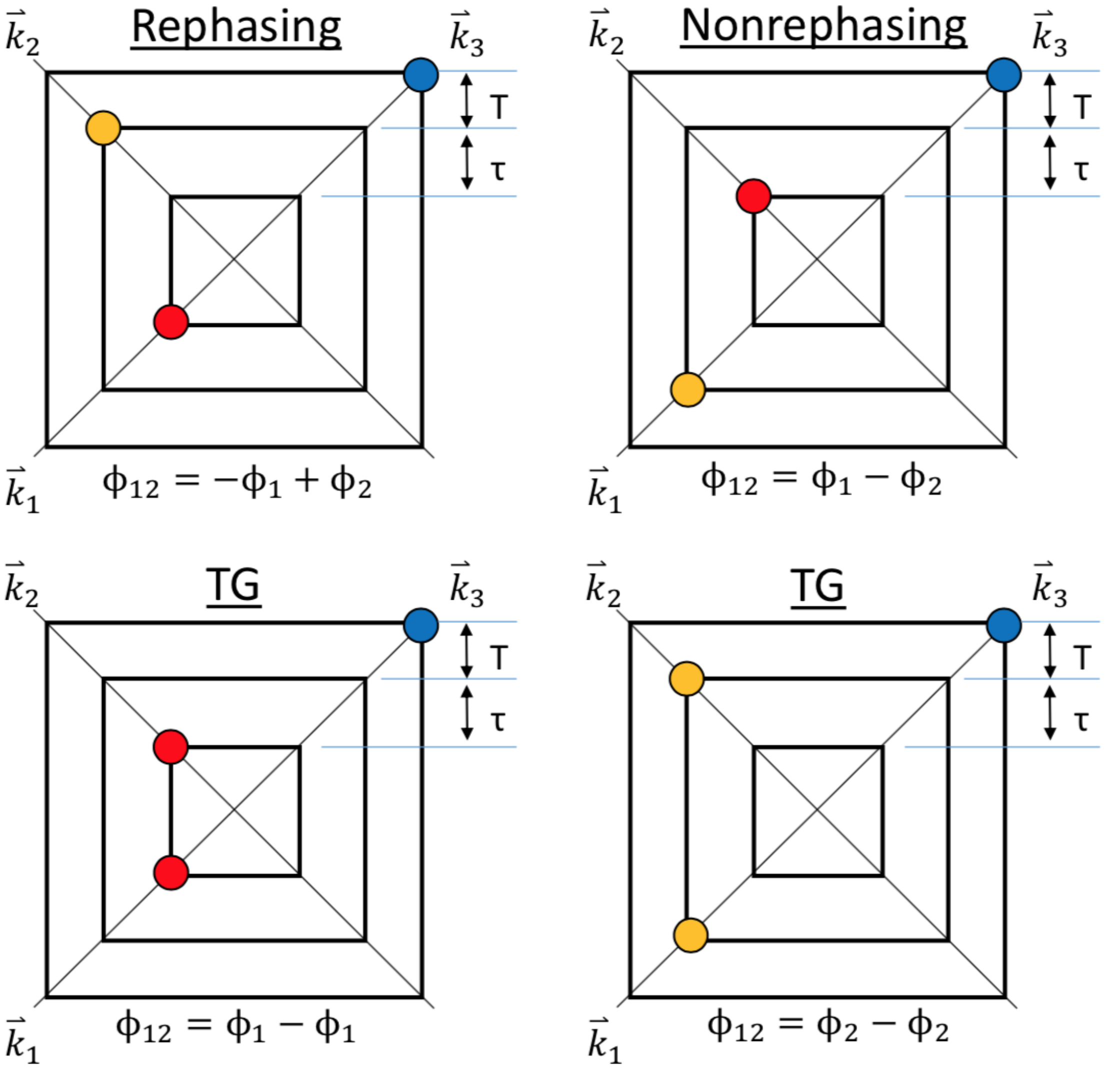

Figure 3.10: Diagrams illustrating the pulse timing scheme used in the box-CARS geometry to obtain Rephasing, Nonrephasing, and TG signals simultaneously for a single waiting time point [14]. Image from [13].

3.3.2 Pump-Probe Geometry

Phase Matching - In the pump-probe geometry pump pulse pairs are collinear and cross with the probe pulse at the sample. As a result, the signal direction is collinear with the probe beam, which can be directly coupled into the spectrometer. This implies that both rephasing and non-rephasing are contained in the signal that emits in the same direction as the probe and can be separated by phase-cycling [64].

Moreover, the third-order polarization signal is intrinsically heterodyned without the need for a delayed pulse, thus removing the need to solve for the global phase [64–66]. **Phase Cycling -** Resolving specific rephasing and non-rephasing signals in the pump-probe geometry requires a four-step phase cycling sequence:

$$(\phi_1, \phi_2) = \left\{(0,0),(0,\pi),(0,\frac{\pi}{2}),(0,\frac{3\pi}{2})\right\}. \tag{3.33}$$

The pump-probe geometry has an advantage over the box-CARS geometry when it comes to simplicity of signal processing. Furthermore, it is a simpler scheme to implement when using broadband continuum light sources. However, the method is limited by the camera intensity saturation threshold as the probe is directly coupled into the camera. The beam intensity control afford over each pulse in the box-CARS geometry is not limited in this way. The box-CARS geometry is also desirable in that it is a completely background free geometry. Thus, both methods have their advantages and disadvantages that must be considered for a given experiment. A comparative look at the two methods (as well as others) can be found in References [61, 66].

3.4 Box-CARS Experimental Setup

Chapter 4 of this thesis describes experiments performed in the box-CARS geometry. Further details will be provided in that chapter, but as a brief summary the experiment looks at the underlying energy landscape of the Q_y and Q_x spectral regions of chlorophyll a (Chl a) and bacteriochlorophyll a (BChl a), specifically seeking an understanding of the coupling between the two transitions. To examine this, experiments therefore implemented a pump light source targeting the Q_x region and a probe light source over the Q_y region. Chl a exhibits a Q_y peak at 667 nm while BChl a's peak is red-shifted by about 100 nm to 770 nm. This requires the use of two different light sources to probe the different pigments. Below I describe the experimental setup and the equipment used.

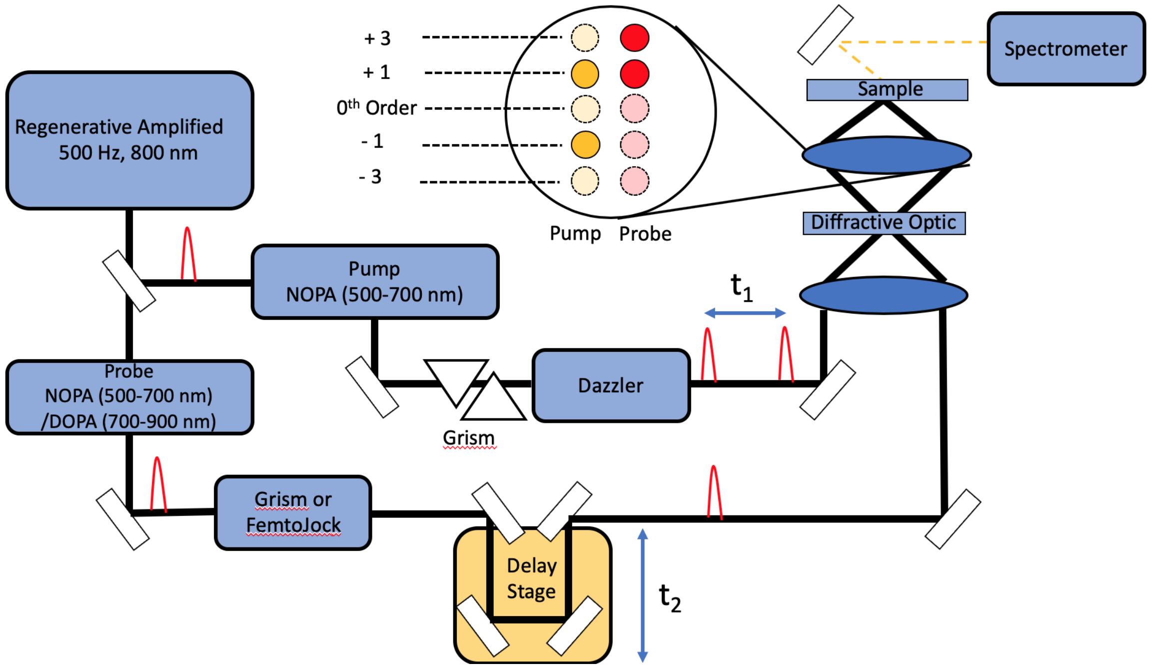

Figure 3.11: Schematic of box-CARS geometry experimental setup. Figure adapted from [13].

Experiments performed in the box-CARS geometry use light originating from a regenerative amplifier (Spectra Physics Spitfire Pro) operating at a 500 Hz rep rate, with a central wavelength of 800 nm, 40 fs pulse width, and 4 mJ pulse energy. This output is split such that one beam seeds an inter-changeable pump light source and a probe light source. The probe light source was chosen based on the spectral conditions of the sample; either using a two dual-stage non-collinear optical parametric amplifier (NOPA) [67] tuned to cover the Q_y band of Chl a or a dual-stage degenerate optical parameteric amplifier (DOPA) [68] tuned to cover the Q_y peak of BChl a. The pump light source was an additional NOPA tuned to cover the Q_x region of both Chl a (620 - 587 nm) and BChl a (578 nm). The pump beam out of the NOPA passes through a pre-compensating grism [69] and then through a Dazzler acousto-optic pulse shaper (Fastlite) capable of generating compressed pulse pairs with precisely controlled pulse timing and phase, for both experiments. Pulse compression with the Dazzler was performed using the SPEAR method [70]. The pump pulse pair beam was then focused on the diffractive optic. For Chl a, the probe beam out of the NOPA also passed through a grism to compress the pulses and its path was directed onto a delay stage where timing with the pump pulses could be controlled. For Bchl a experiments, the probe out of the DOPA passed through a FemtoJock (Biophotonic Solutions) which used a spatial light modulator and the MIIPS method [71] to compress the pulse. The probe was then also focused onto the diffractive optic. In both Chl a and BChl a experiments, the pump and probe beams focused onto the diffractive optic and higher orders were blocked using spatial filtering as depicted in Figure (3.9). Third-order polarization signals were collected as described in Section (3.3.1) and coupled into a spectrometer. Scans were performed by moving the pump delay stage to each t_2 position and scanning the t_1 values with the Dazzler. At each t_1 position, the six phase cycling spectra are measured, as well as measurements with the probe beam blocked to be subtracted in post processing to remove contributions from pump scatter. This process maintains a 90% duty cycle.

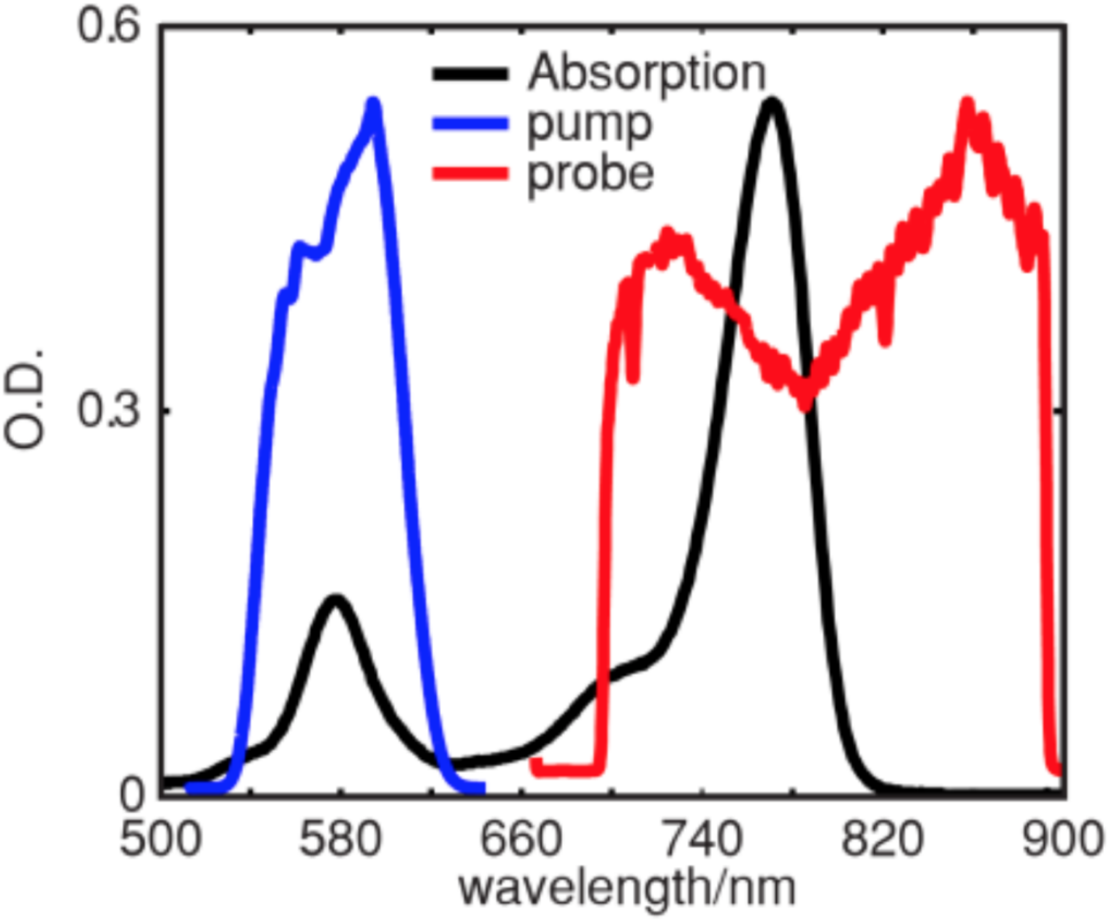

Figure 3.12: Linear absorption spectrum of Bchl a (black), with the NOPA generated pump (blue) and DOPA generated probe (red) spectra used in the experiment.

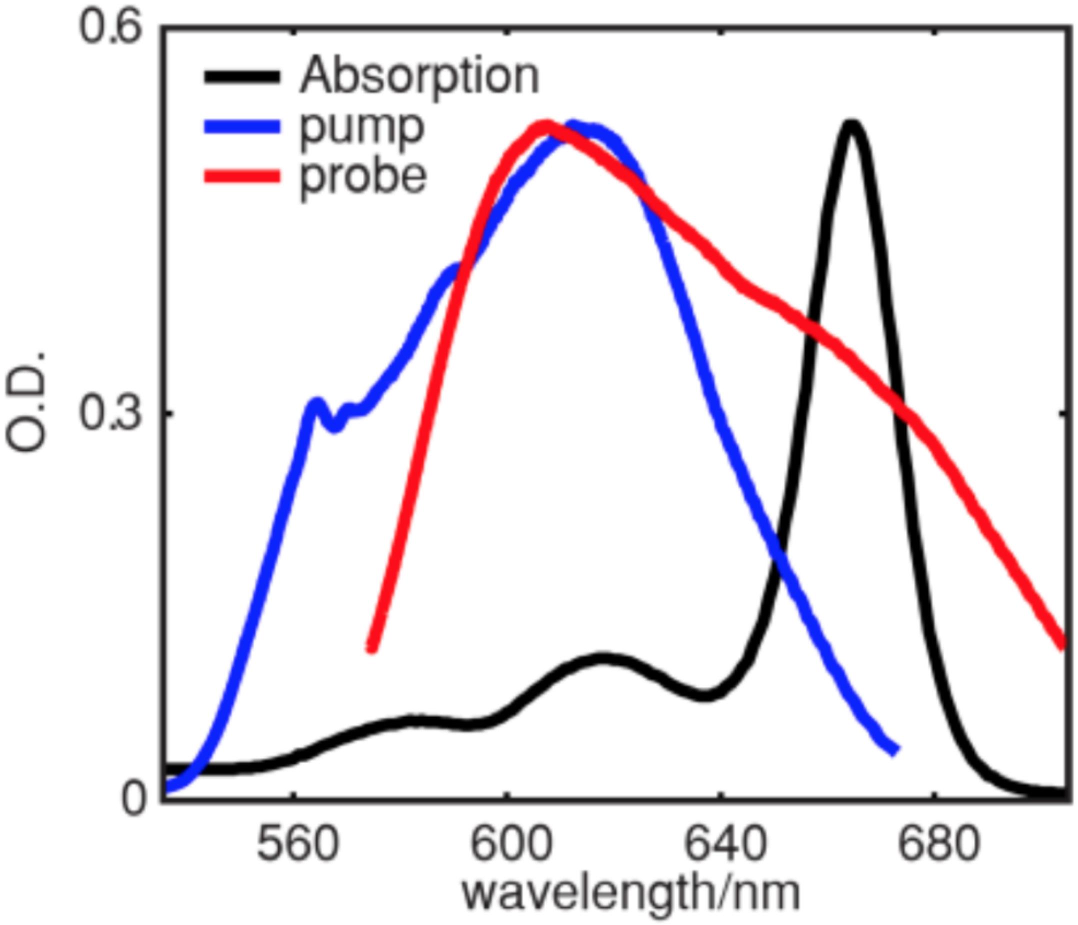

Figure 3.13: Linear absorption spectrum of Chl a (black), with the NOPA generated pump (blue) and NOPA generated probe (red) spectra used in the experiment.

3.5 Pump-Probe Experimental Setup

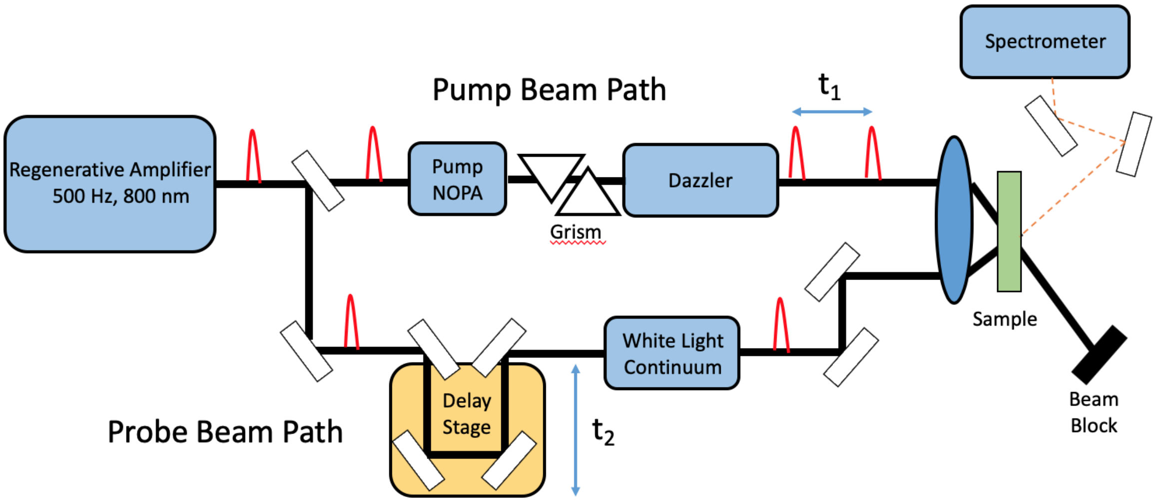

Figure 3.14: Schematic of pump-probe experimental geometry built by Song et al. [15].

Experiments in the pump-probe geometry are described in detail in Chapter 5. The experiments take advantage of the multiple inter-changeable light sources available in the Laboratory for Ultrafast Multidimensional Optical Spectroscopy (LUMOS) [15], implementing a NOPA pump and white light continuum broadband probe.

Ultrafast light pulses are generated in a Spitfire ACE regenerative amplifier (Spectra Physics) with 800 nm central wavelength, operating at a 500 Hz rep-rate (8 mJ pulse energy), and with a 35 fs pulse width. As in the box-CARS experiments, light out of the regenerative amplifier was split into separate pump and probe beams, with the pump seeding a NOPA and a probe generating a white light continuum in either a fused silica (FS) of calcium fluoride (CaF_2) crystal. The NOPA was tuned to have a center wavelength of 650 nm with an approximately 90 nm bandwidth covering both the Q_y absorption centered at 677 nm and the first higher energy peak at 625 nm. Light out of the NOPA was pre-compressed with a grism and further compressed to 15 fs using a Dazzler and the SPEAR method [70]. As in the box-CARS setup, the Dazzler was also used to generate pump pulse pairs and control the t_1 timing and relative pulse phases. Crystals for the probe light were chosen based on the spectral range it could cover. Light from the FS crystal cover the 475-725 nm range while light from the CaF_2 crystal covered the 375-725 nm range. Such broad band light cannot be adequately compressed while maintaining sufficient pulse energy. Instead, the linear chirp of the broadband probe was corrected in the post-processing in the method demonstrated by Tekavec et al. [72]. Probe light out of the crystals passed through a delay stage to control the t_2 delay. Pump and probe beams were crossed at the sample and focused to approximately 100 μm^2 (pump) and 90 μm^2 (probe) spot sizes. As explained in Section (3.3.2), the phase-matched direction emerges in the direction of the probe beam, which is then coupled to the spectrometer. Similar to the box-CARS case, the experiment follows a scanning procedure where for each t_2 delay value, the t_1 range is scanned performing a four-step phase cycling measurement at each t_1 step to obtain both rephasing and non-rephasing signals. A shutter is used to block the probe to subtract contributions from pump scatter.

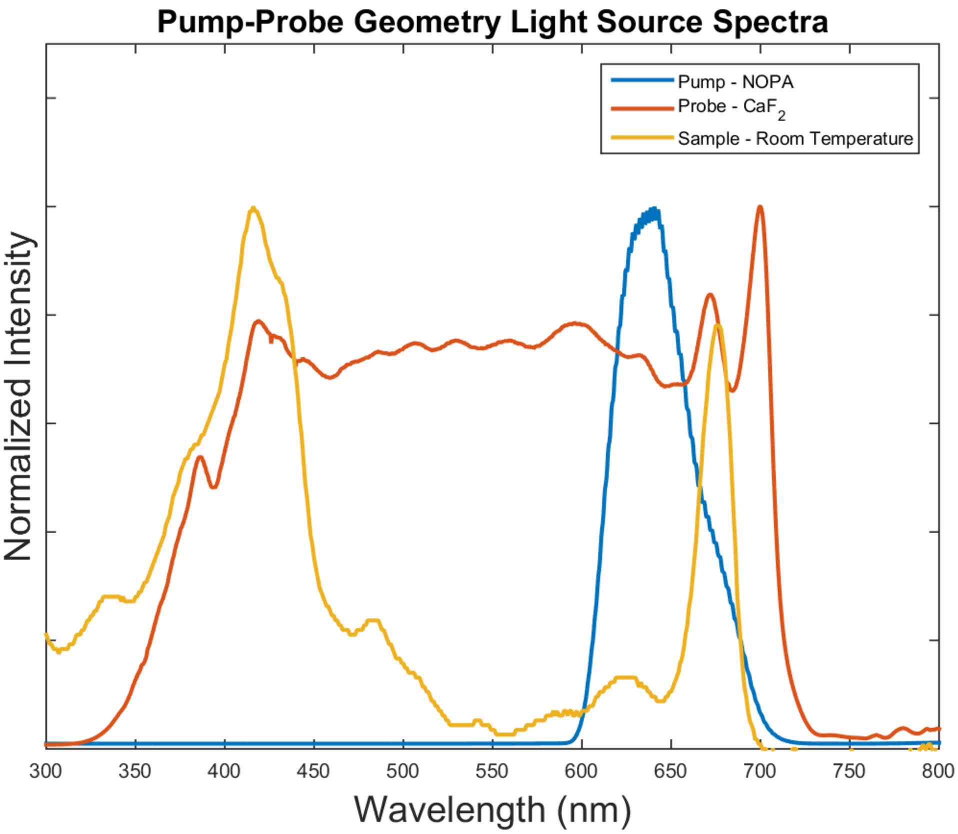

Figure 3.15: Pump-probe geometry using a calcium fluoride crystal for supercontinuum white light generation on the probe line.

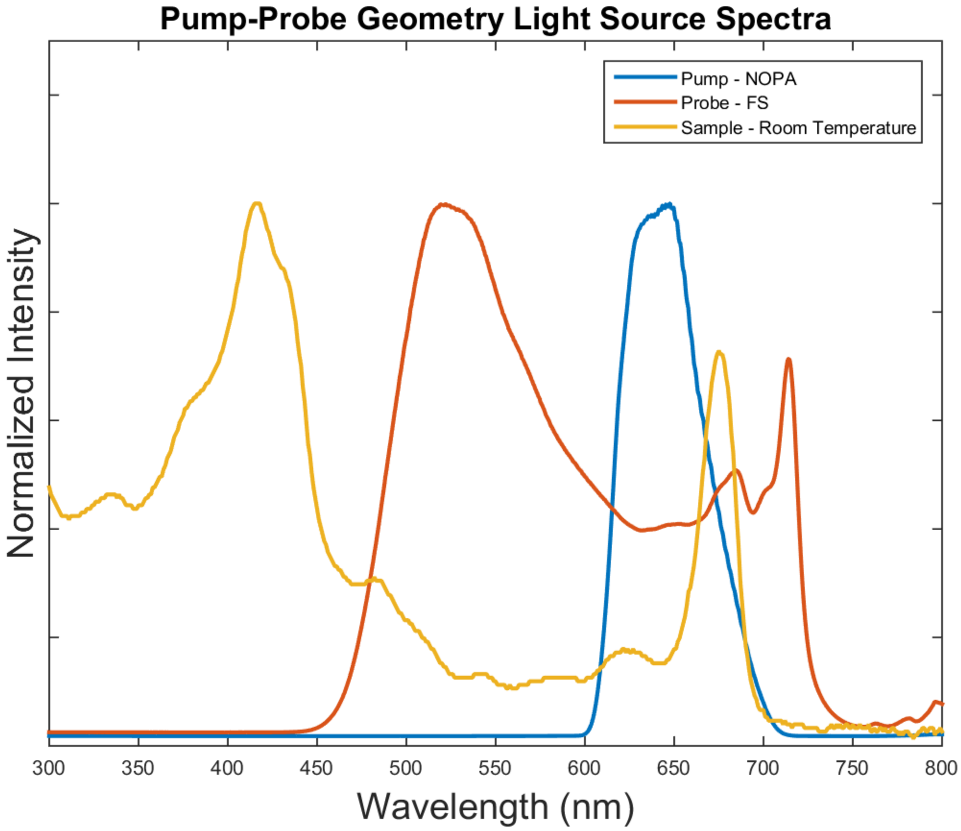

Figure 3.16: Pump-probe geometry using a fused silica crystal for supercontinuum white light generation on the probe line.

CHAPTER 4

Investigating Vibronic Structure and Photoinduced Dyanmics of Bacteriochlorophyll a and Chlorophyll a by Polarized 2D Spectroscopy and ab initio Calculations

In Chapter 1 I emphasized the spectral congestion in the Q_y band of the D1D2 RC and the spectroscopic challenges this presents. These challenges are further compounded by the fact that the underlying Q-band structure for the individual pigments is also widely debated [73]. In this chapter I describe a set of experiments performed separately on bacteriochlorophyll a (Bchl a) and chlorophyll a (Chl a) pigments investigating the underlying electronic and vibrational structure of the Q-band in these two pigments. Results of these measurements were compared against quantum-chemical calculations made with our collaborators in the Chemistry Department here at the University of Michigan and at Kent State University. At the time of writing this thesis, the results of this study are in submission to the journal Chem. The author list is Yin Song, Alexander Schubert, Elizabeth Maret, Ryan K. Burdick, Barry D. Dunietz, Eitan Geva, and Jennifer P. Ogilvie. The title is **Combining polarized two-dimensional electronic spectroscopy with ab initio calculations to investigate the vibronic structure and photoinduced dynamics of bacteriochlorophyll a and chlorophyll a**. The data collection and analysis was performed by myself with Yin Song under the guidance of Jennifer Ogilvie, while the theoretical work was led by Alexander Schubert in collaboration with the Geva and Dunietz groups.

4.1 Chl a and Bchl a

Chl a and Bchl a are two of the most abundant pigments found in photosynthetic systems. As such, they serve a number of functional roles, including energy transfer in antennae systems and charge separation in reaction centers. They exhibit nearly identical chemical structure, both having a planar tetra pyrrole chlorin ring with the four nitrogen atoms coordinated to a central magnesium atom. An additional fifth pyrrole prevents the molecules from achieving the large degree of symmetry seen by their tetrapyrrole cousins. The molecules also both have a long phytyl containing hydrocarbon tail. There are two primary chemical differences between the pigments, the locations of which are marked in red on Figure (4.1) that influence differences in electronic structure [74].

Because of the large degree of similarity to porphyrins, since the 1960s, understanding of the electronic structure of Chl a and Bchl a has been interpreted through the framework of the Gouterman model [25]. By this model, two bands of electronic transitions occur: the lower energy Q band and higher energy Soret Band (or B band). In the Q band, the transition dipole moments (TDM) fall in the molecular plane, where partial hydrogenation leads to symmetry break, producing a perpendicularly polarized Q_x and Q_y transitions. Further hydrogenation in Bchl a leads to a larger split in Q_x and Q_y. Figure (4.2) shows the linear absorption spectra of the two pigments (which the pump (blue) and probe (red) spectra used in the experiments). From these spectra it is clear that Chl a exhibits three peaks in the Q-band at 667, 620, and 587 nm, while Bchl a has two well separated peaks at 770 and 578 nm. Throughout this chapter I will refer to the Q_y electronic transition as S_1 and the Q_x electronic transition as S_2. The three peaks of the Chl a linear absorption will occasionally be referred to as E_1 (667 nm), E_2 (620 nm), and E_3 (587 nm) (see Figure (4.8) for details).

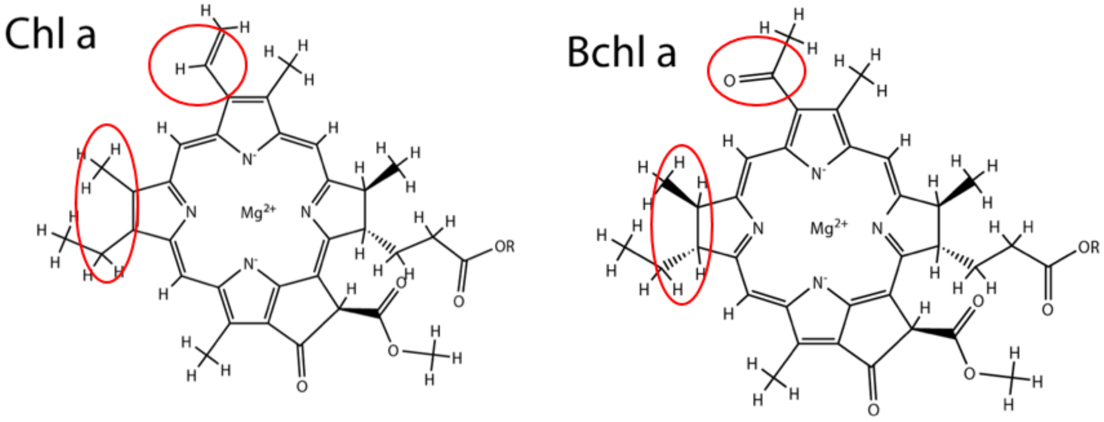

Figure 4.1: Chl a and Bchl a chlorin ring chemical structures omitting the hydrocarbon tails. The pigments exhibit nearly identical structure expect at the locations noted in red.

The Gouterman model has strong qualitative agreement with linear absorption measurements, but falls short in explaining a number of quantitative spectroscopic results. Some examples of these shortcomings are that some measurements have found Q_x and Q_y are not completely orthogonal and magnetic circular dichroism measurements cannot be described using this model. Some studies have attributed the disagreement between the Gouterman model and spectroscopic data to contributions from vibronic coupling. We investigated the underlying electronic structure of the Q-band by using 2DES with added polarization control over the pump and probe beams (described below), which allows us to resolve the spatial orientation of TDMs. The results were compared against quantum calculations.

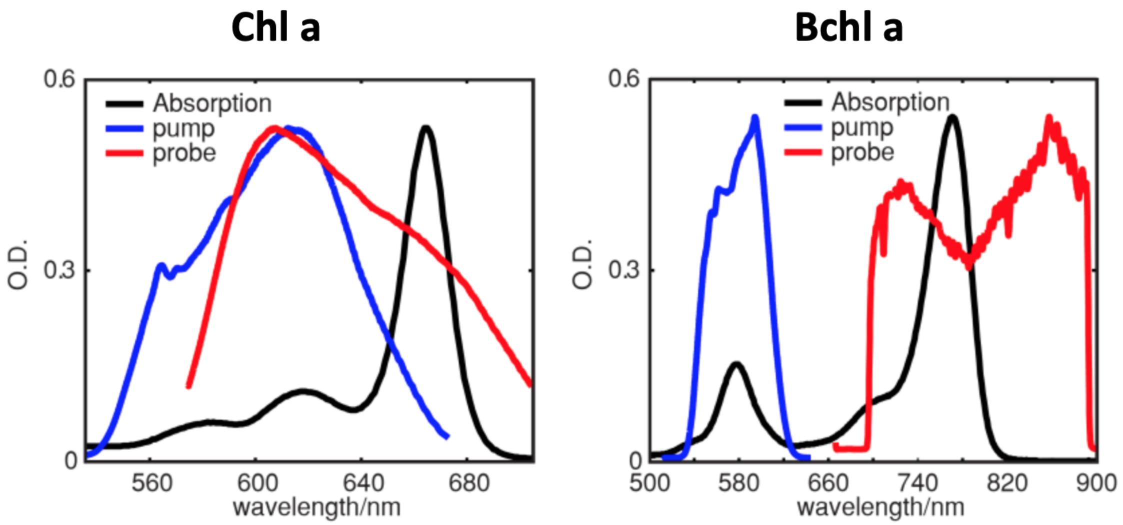
Chl a

Bchl a

Figure 4.2: Linear absorption spectra of Chl a and Bchl a overlayed with the pump and probe spectra use in the respective experiments.

4.2 Polarized 2DES (P-2DES)

Applying polarization dependence to the pulses in a 2DES experiment pulse sequence enables selective enhancement of cross peaks. To illustrate this, recall Equation (3.22) from Chapter 3, which describes the third-order polarization signal generated by the 2DES experiment. The equation is reproduced below using the absolute times τ_1, τ_2, and τ_3 for the times between pulses 1 and 2, 2 and 3, and 3 and measurement, respectively.

$$\begin{aligned} P^{(3)}(t) = \left(\frac{-i}{\hbar}\right)^3 \int_{-\infty}^{t} d\tau_3 \int_{-\infty}^{3} d\tau_2 \int_{-\infty}^{\tau_2} d\tau_1 E_3(\tau_3) E_2(\tau_2) \times \\ E_1(\tau_1) \langle \mu(t)[\mu(\tau_3), [\mu(\tau_2), [\mu(\tau_1), \rho(-\infty)]]] \rangle \end{aligned} \tag{4.1}$$

Here, the angled brackets indicate an orientational average over all space. This equation assumes an all parallel configuration where the vectoral nature of the electric fields and transition dipoles is dropped. In order to consider how polarization of the laser pulses influences the dipoles of the system the vectoral nature of these terms must now be introduced. The laser pulses can be considered in the semi-impulsive limit, where the field interactions are approximated by delta functions making it a simple task to solve the integrals. The resulting signal is as follows:

$$S \propto \langle(\overrightarrow{\mu}_\delta \cdot \overrightarrow{E}_d)(\overrightarrow{\mu}_\gamma \cdot \overrightarrow{E}_c)(\overrightarrow{\mu}_\beta \cdot \overrightarrow{E}_b)(\overrightarrow{\mu}_\alpha \cdot \overrightarrow{E}_a)\rangle \tag{4.2}$$

where it becomes apparent that the resulting signal is the orientational average of the product of dot products between the set of dipoles $\{\delta\gamma\beta\alpha\}$ and fields $\{dcba\}$. This relation can be further simplified if the unit vectors of each vector is separated from the field and dipole strength.

$$\begin{aligned} S &\propto \langle(\hat{\mu}_\delta \cdot \hat{E}_d)(\hat{\mu}_\gamma \cdot \hat{E}_c)(\hat{\mu}_\beta \cdot \hat{E}_b)(\hat{\mu}_\alpha \cdot \hat{E}_a)\rangle\langle\mu_\delta\mu_\gamma\mu_\beta\mu_\alpha\rangle(E_dE_cE_bE_a) \\ &\propto \langle(\hat{\mu}_\delta \cdot \hat{E}_d)(\hat{\mu}_\gamma \cdot \hat{E}_c)(\hat{\mu}_\beta \cdot \hat{E}_b)(\hat{\mu}_\alpha \cdot \hat{E}_a)\rangle \end{aligned} \tag{4.3}$$

Equation (4.3) is known as the four-point correlation function. From this relation it can be seen that the dot product between the dipole and field unit vectors can be viewed as a weighting parameter where the vector relationship between the dipole orientation and field polarization can be tuned to assign a specified strength to the signal. Such control over signal strength can be advantageous when it enhancing cross peaks over diagonal peaks is desired.

To illustrate the usefulness of polarization dependent tune-ability, imagine the case of a single dipole transition $\hat{\alpha}$ isotropically oriented in space (i.e., randomly oriented) that is excited with pulse all oriented parallel to each other along the z-direction in the laboratory frame. The signal strength weight factor in this case can be expressed in the following equation:

$$\begin{aligned} S_p &= \langle(\hat{Z}\cdot\hat{\alpha})(\hat{Z}\cdot\hat{\alpha})(\hat{Z}\cdot\hat{\alpha})(\hat{Z}\cdot\hat{\alpha})\rangle \\ &= \frac{1}{4}\int_0^{2\pi} d\phi \int_0^{\pi} d\theta sin\theta(cos\theta)^4 \\ &= \frac{1}{5} \end{aligned} \tag{4.4}$$

The orientational average overall space is performed by performing the integral in spherical coordinates taking advantage of the relations $(\hat{Z}\cdot\hat{\alpha}) = cos\theta$, $(\hat{X}\cdot\hat{\alpha}) = sin\theta cos\phi$, and $(\hat{Y}\cdot\hat{\alpha}) = sin\theta sin\phi$. The result of Equation (4.4) means that the diagonal signal for a collection of isotropically oriented α dipoles in a P-2DES experiment with have one fifth the strength it would otherwise have if all the dipoles were also oriented in the z-direction. Similarly, the diagonal peak signal strength can be found when using a cross polarized scheme where the pump and probe pulses polarization are orthogonal to each other.

$$\begin{aligned} S_c &= \langle(\hat{Z}\cdot\hat{\alpha})(\hat{Z}\cdot\hat{\alpha})(\hat{X}\cdot\hat{\alpha})(\hat{X}\cdot\hat{\alpha})\rangle \\ &= \frac{1}{4}\int_0^{2\pi} d\phi \int_0^{\pi} d\theta sin\theta(cos\theta)^2(sin\theta cos\phi)^2 \\ &= \frac{1}{15} \end{aligned} \tag{4.5}$$

Here it is clear that a diagonal peak for the isotropic α dipole excited with the cross polarized scheme will have one fifteenth the strength it would have if the dipoles were all parallel to the pulses. With this it becomes apparent that if separate measurements are made in the parallel and cross polarized configurations by performing the subtraction $S_p - 3S_{CP}$ will completely cancel the dipole diagonal peak signal, leaving only contributions from cross peaks, i.e., $S_{XP} = S_p - 3S_{CP}$. Recovering this cross peak signal can be very powerful in enhancing signals that might otherwise be much weaker than the resonant diagonal signals. In the context of this study, it enables the removal of signals from pathways involving all parallel TDM and thus a peak in the cross peak specific spectrum indicates signals from pathways with non-parallel

TDMs.

Extracting cross peak signals becomes more challenging when considering a system with two coupled dipoles. The parallel signal in this case becomes:

$$\begin{aligned} S_p &= \langle(\hat{Z}\cdot\hat{\alpha})(\hat{Z}\cdot\hat{\alpha})(\hat{Z}\cdot\hat{\beta})(\hat{Z}\cdot\hat{\beta})\rangle \\ &= \frac{1}{45}(4P_2(cos\theta_{\alpha\beta})+5) \\ &= \frac{1}{15}(2cos^2\theta_{\alpha\beta}+1) \end{aligned} \tag{4.6}$$

where $P_2(cos\theta_{\alpha\beta})$ is the $l = 2$ Legendre polynomial and $\theta_{\alpha\beta}$ is the angle between the α and β dipoles. Similarly, the cross polarized signal for a coupled dipole system is:

$$\begin{aligned} S_c &= \langle(\hat{Z}\cdot\hat{\alpha})(\hat{Z}\cdot\hat{\alpha})(\hat{X}\cdot\hat{\beta})(\hat{X}\cdot\hat{\beta})\rangle \\ &= \frac{1}{15}P_2(cos\theta_{\alpha\beta}) \\ &= \frac{1}{30}(3cos^2\theta_{\alpha\beta}-1) \end{aligned} \tag{4.7}$$

Using the same cross peak specific signal relation $S_{XP} = S_p - 3S_{CP}$ the relation can be manipulated to find an expression for the angled between the dipoles dependent on the parallel and cross polarized signals.

$$\theta_{\alpha\beta} = Cos^{-1}\left(\sqrt{\frac{2S_p - S_{cp}}{S_p + 2S_{cp}}}\right) \tag{4.8}$$

Therefore, Equation (4.8) implies that by taking 2DES measurements in the parallel and cross polarized configurations the angle between dipole moments can be calculated. Additionally, the anisotropy relation can also be calculated.

$$r = \frac{S_p - S_{cp}}{S_p + 2S_{cp}} \tag{4.9}$$

Proof of concept of P-2DES was performed on a chemical compound by Zanni et al. [75] and has been applied to photosynthetic complexes by the Fleming group [76, 77].

We performed these measurements on Chl a and BChl a by integrating half-waveplate and wire-grid polarizer pairs into the pump and probe arms of the 2DES BOXCARS setup (Figure (4.3)).

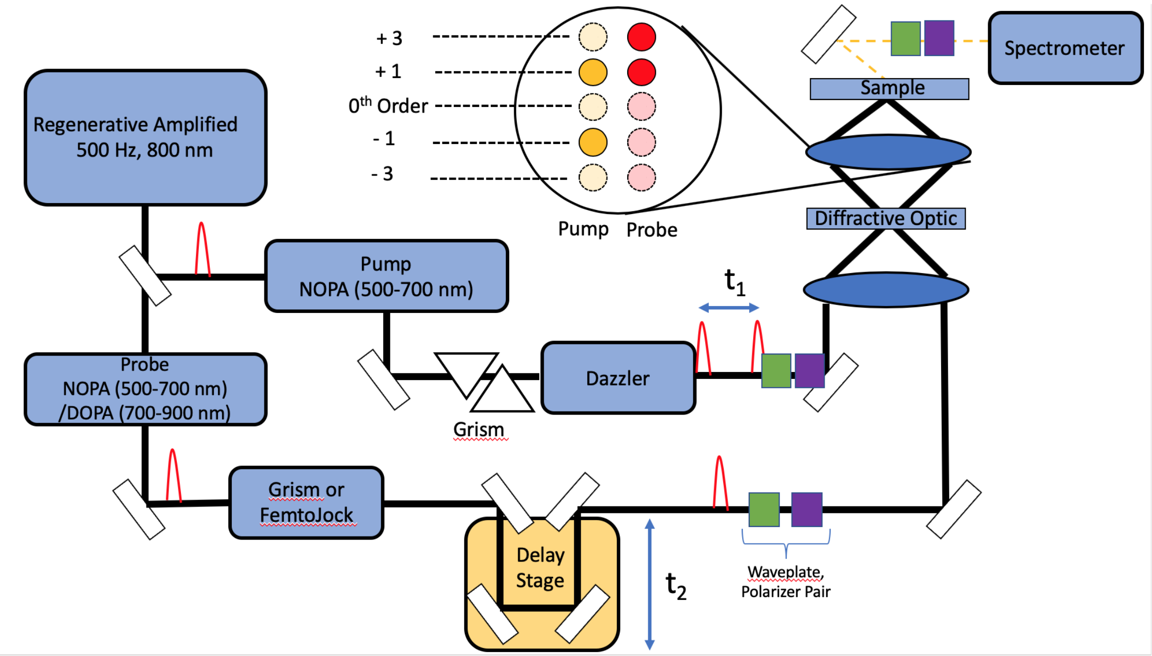

Figure 4.3: BOXCARS experimental setup with added half-waveplate and polarizer pairs in the pump and probe lines. The final waveplate/polarizer pair before the spectrometer serves to match the measured signal polarization with the optimal polarization for the spectrometer grating.

4.3 P-2DES Results

Chl a (from spinach) and Bchl a (from *Rhodopseudomonas spharoides*) samples were purchased from Sigma Aldrich. For the purpose of reducing the variables that could influence orientation of the TDM vectors, Chl a and Bchl a samples were used in solvents that result in penta coordination of the magnesium atom in the chlorin ring. Therefore Chl a was dissolved in isopropanol and BChl a was dissolved in acetone. Both samples were prepared under N_2 atmosphere and purged with N_2 gas for 5 minutes before loading into the sample cell (also under N_2 atmosphere). Sample cells were sealed using either vacuum grease or epoxy. P-2DES measurements were taken at room temperature.

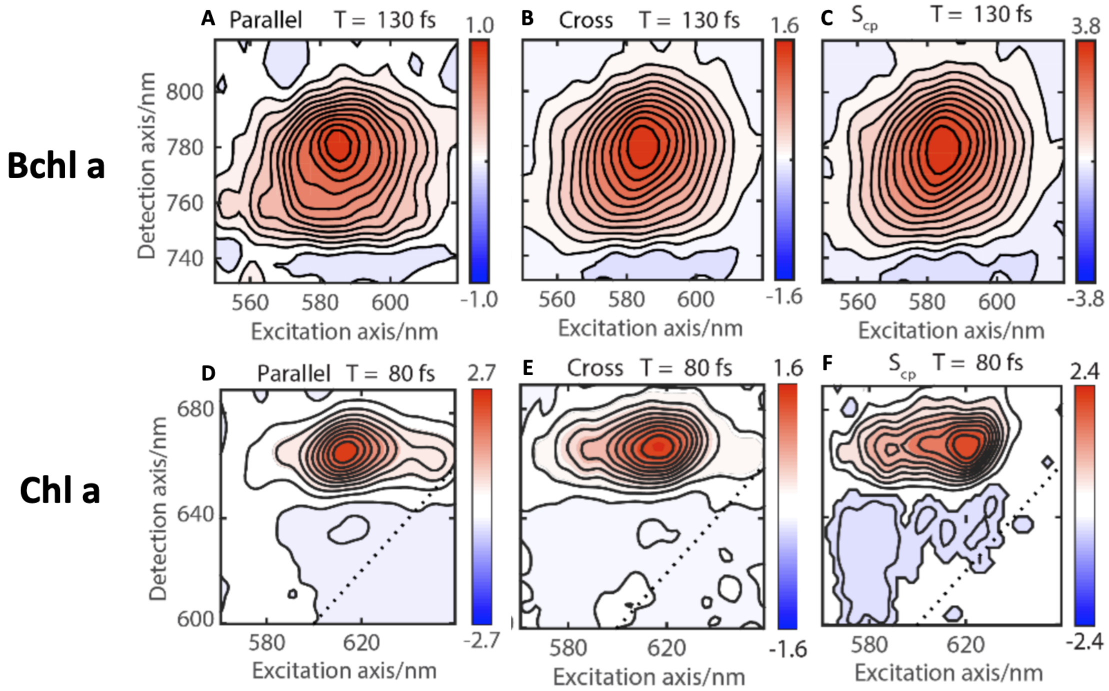

Figure 4.4: P-2DES measurements in the parallel (A and D) and cross (B and E) polarized configurations with the calculated cross peak specific spectra (C and F). The top row shows the spectra for Bchl a (at 130 fs) and the bottom row for Chl a (at 80 fs). Waiting times were chosen to eliminate signal contribution from solvent response.

2DES spectra of Bchl a and Chl a taken in the parallel and cross polarized configurations, as well as the resulting cross peak specific spectra are presented in Figure (4.4). In the case of Bchl a, one strong cross peak persists among all three spectra at a 578 nm excitation wavelength and 780 nm detection wavelength. This is slightly shifted from the expected detection wavelength of 770 nm due to the laser pulse spectra inducing amplitude modulation. The presence of this peak in all three spectra suggests the TDM of the Q_x and Q_y peaks are non-parallel, as predicted by the Gouterman model. To investigate the nature of the TDM angle further, the angle between Q_x and Q_y and the anisotropy are calculated using Equation (4.8) using data from a spectral cut along the excitation axis at the detected 771 nm wavelength. The results of these calculations for Bchl a and Chl a are presented in Figure (4.5).

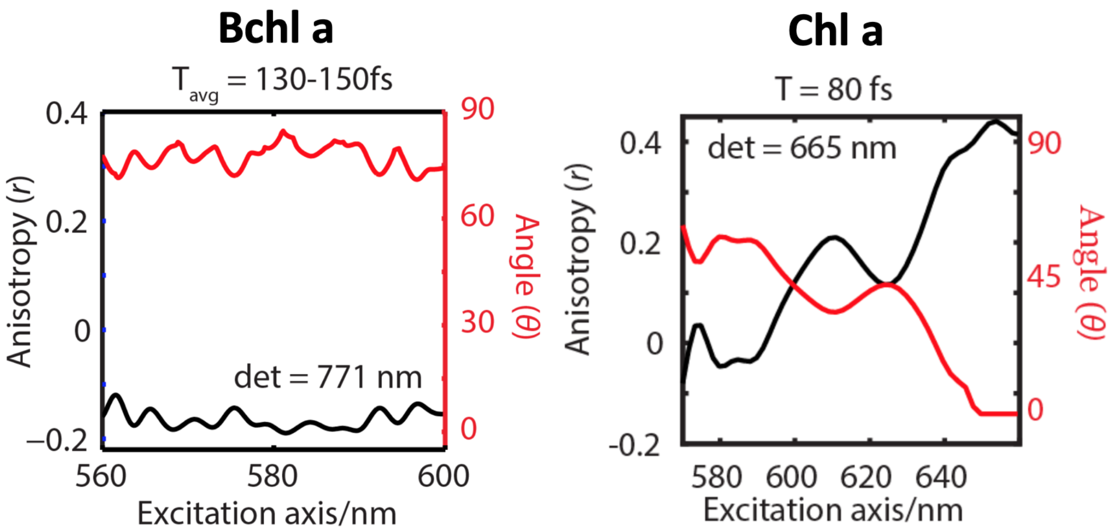

Figure 4.5: Anisotropy and angles calculated for the TDMs of Bchl a and Chl a from slices through the excitation axes of the P-2DES data at the detected wavelengths 771 nm for Bchl a and 665 nm for Chl a.

The anisotropy value for Bchl a is roughly constant across the excitation axis at a value of -0.15. Having a constant anisotropy supports the idea that there are only two TDM in this region. The value of the anisotropy also suggests that the Q_x and Q_y TDMs are nearly perpendicular, but not 90°, as predicted in the Gouterman model. It should be noted that the studies in references [78] and [79] suggest that there could be excited state absorption (ESA) contributions in this region hidden under ground state bleach (GSB) signals that could influence the obtained anisotropy value [80]. However, anisotropy measurements on the Q_y peak performed in references [81] and [82] report anisotropy values of 0.4 and 0.42, respectively, suggesting either the ESA extinction coefficient is small or that it is oriented in the same direction at the Q_y TDM. Either way, this does not influence the validity of our anisotropy values.

Calculating the angle between the Q_x and Q_y TDM of Bchl a, we find a roughly constant angle of 75°. Ab initio calculations calculated with the OT-SRSH-PCM TD-DFT method by our collaborators (discussed below) calculate an angle of 77.6°, in excellent agreement with our findings. Other studies find similar deviations from the expected 90°. For example, the studies in references [83] and [84] find angles of 68-72° for measurements of BChl a of an unknown coordination measured in cyclohexanol and castor oil. Another study performing semi-empirical calculations of the Bchl a finds a 70° angle [85]. Taken together, these other studies support our finding that the angle between the Q_x and Q_y TDMs is approximately 75° in penta-coordinated Bchl a. To the best of our knowledge, this is the first measurement of this angle for the penta-coordinated case.

Panels D, E, and F of Figure (4.4) show the measured parallel and cross polarized 2DES spectra with the calculated cross-peak specific spectrum for Chl a. From the parallel and cross polarized 2DES spectra, three cross peaks become apparent at a detection wavelength of 665 nm: CP1 at 650 nm excitation wavelength, CP2 at 625 nm, and CP3 at 588 nm. However, CP1 disappears in the resulting cross peak specific spectrum. This means that the TDM of this state is parallel with S_1 and we therefore ascribe it to be a vibrational overtone of S_1. This also indicates that CP2 and CP3 belong to separate electronic/vibrational transitions.

As was done with Bchl a, the anisotropy and angle between TDMs was calculated as a function of excited wavelength at a detected wavelength of 665 nm. According to the results of references [86–88] ESA contributions to the signal should be $<$ 5%, thus lending confidence to our calculated anisotropy and angle values. Figure (4.5) shows that, in contrast with Bchl a, the anisotropy and TDM angles of Chl a have a strong wavelength dependence, where CP2 is approximately 45° and CP3 is approximately 60°. Using polarized fluorescence measurements on hexa-coordinated Chl a, references [89] and [90] report an angle of 56° between S_1 and S_2. Furthermore, another study using linear dichroism and polarized fluorescence measurements on Chl a in a unknown coordinateion in liquid crystals finds an angled of 90° between S_1 and S_3. To the best of our knowledge, our measurements are the first reported for penta-coordinated Chl a.

TD-DFT calculations made by our collaborators on tetra-, penta-, and hexa-coordinated Chl a find an axial ligation dependence in the angle values between to adiabatic electronic states where the angles are 79.7°, 75°, and 73.8° respectively. This dependence was absent in the BChl a case. These calculated values are notably larger than either the 45° of CP2 or 60° of CP3 obtained from our measurements. This can be explained by examining the calculated spectra (produced by our collaborators). This spectrum plots the overtones calculated from two electronic transitions. In the CP1 region at 650 nm, there is contribution from only one electronic transition, giving it the same polarization as S_1, and hence it disappears in the cross peak specific spectrum. However, the CP2 and CP3 regions have contributions from both electronic transitions and the varying degrees of overlap in these regions, which alters the dipole orientations. Considering this spectrum in the context of Q_x and Q_y, it can be deduced that CP2 contains an overlap in contributions from the Q_x 0th overtone, and the Q_y 1st overtone. CP3, on the other hand, has contributions from Q_x first overtone and Q_y second overtone.

Many previous studies argue that the Q-band structure can be explained in the context of vibronic coupling [73, 89, 91, 92]. In particular, Reimers et al. [73] make a particularly compelling case in requiring a vibronic model to fit their magnetic circular dichrosim measurements. Our results do not contradict a vibronic model. The overlap seen in the $S_0 \to S_1$ and $S_0 \to S_2$ transitions of the calculated spectrum can have vibronic mixing from weak electronic/vibronic coupling. For Bchl a, the energy gap between Q_x and Q_y is too large to experience similar vibronic coupling. This raises interesting questions regarding how electronic/vibornic coupling influence photoexcited dynamics in Chl a and Bchl a. Moreover, the underlying mechanisms of Q-band energy transfer raise interesting questions in considering big-picture energy transfer in the reaction center.

4.4 Internal Conversion

The temporal resolution of our ultrafast P-2DES experiments affords us the ability to calculate internal conversion rates between the states found in Chl a and Bchl a. We do this by using the parallel and cross polarized spectrum to calculate the spectrum that would be obtained under the magic angle condition $S_{MA} = 2S_{cp} + S_p$. Therefore the data are not influenced by an orientational dependence. From this data, we take traces through time at the cross peaks present in both Chl a and Bchl a data, which are presented in Figure (4.6) with the performed fitting.

From the traces in Figure (4.6) there is a clear strong solvent response within the first 50 fs of both pigments. Since internal conversion times are expect to be fast, we attempt to exclude these contributions from the fitting by applying an extra term developed by Ernsting [16]. In doing so, an internal conversion rate for $Q_x \rightarrow Q_y$ in Bchl a is found to be 11 ps^{-1} (89 fs). In Chl a $S_2 \rightarrow S_1$ is 50 ps^{-1} (20 fs) and $S_2 \rightarrow S_1$ is 38 ps^{-1} (26 fs).

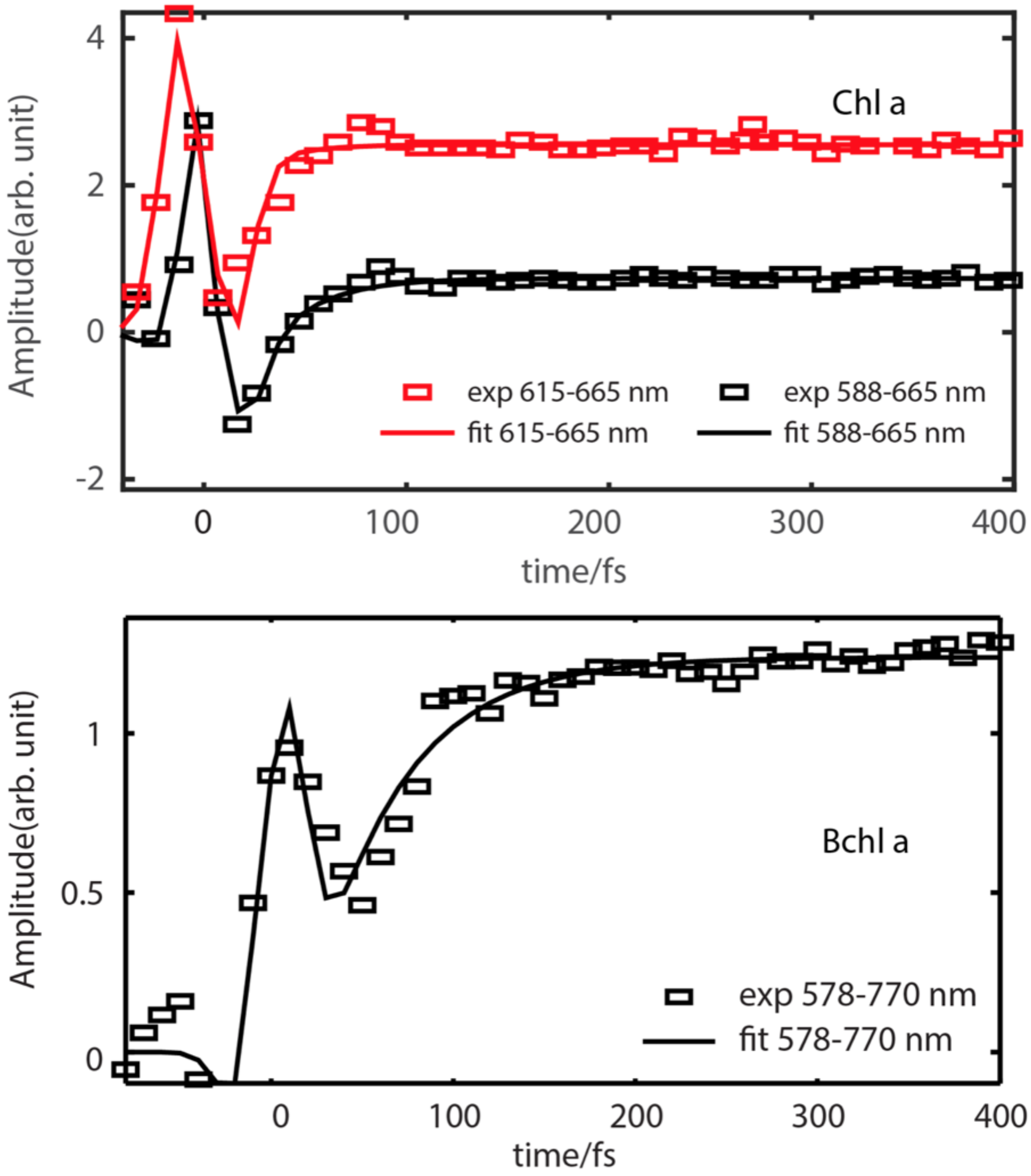

Figure 4.6: Time traces from P-2DES experiments reconstructed to produce the magic angle condition. Fits were made applying an extra term described by Ernsting [16] to remove solvent response contributions.

Several other studies have reported internal conversion rates in Chl a and Bchl a. Studies estimating internal conversion from absorption linewidths and fluorescence line narrowing data find hexa-coordinated Bchl a to have a rate of 30 fs^{-1} [73,92] and the hexa-coordinated Chl a $S_2 \rightarrow S_1$ transition (at 4K) to have a rate of 16-32 fs^{-1} [91].

These rates are much faster than those found in our study and nearly the same for both pigments. This suggests a possible underestimation of the inhomogeneous broadening contribution in their calculations. On the other hand, studies using pump-probe measurements report internal conversion rates of both Chl a and Bchl a occur in less than 100 fs, which approaches the resolution limit of these experiments [80, 93–96]. 2DES studies on hexa-coordinated Chl a with a narrow spectral bandwidth over Q_y have also been done [97–99]. The study in [99] uses an all parallel pulse polarization scheme to measure the rephasing spectra covering the whole Q_y peak of 625-690 nm. This study finds a vibrational relaxation pathway occur within 170 fs in the S_1 band and a 40 fs transition from S_2 to a higher lying vibrational mode of S_1. This faster $S_2 \rightarrow S_1$ 40 fs transition is in good agreement with our values obtained via a similar experimental method.

Calculations performed by our collaborators use a Fermi's Golden Rule calculation to find the effective electronic coupling values of Bchl a and Chl a. From this it is found that Bchl a has an effective electronic coupling of 53 meV and Chl a one of 45 meV. These values fall within the weak-to-intermediate coupling regime [100], which is still strong enough to have mixing of vibronic states. This is in support of the Reimers vibronic coupling framework which can lead to mixing of the Q_x and Q_y states in Chl a [73]. However, the scope of our study cannot offer irrefutable evidence for this model and more work must be done before making such claims.

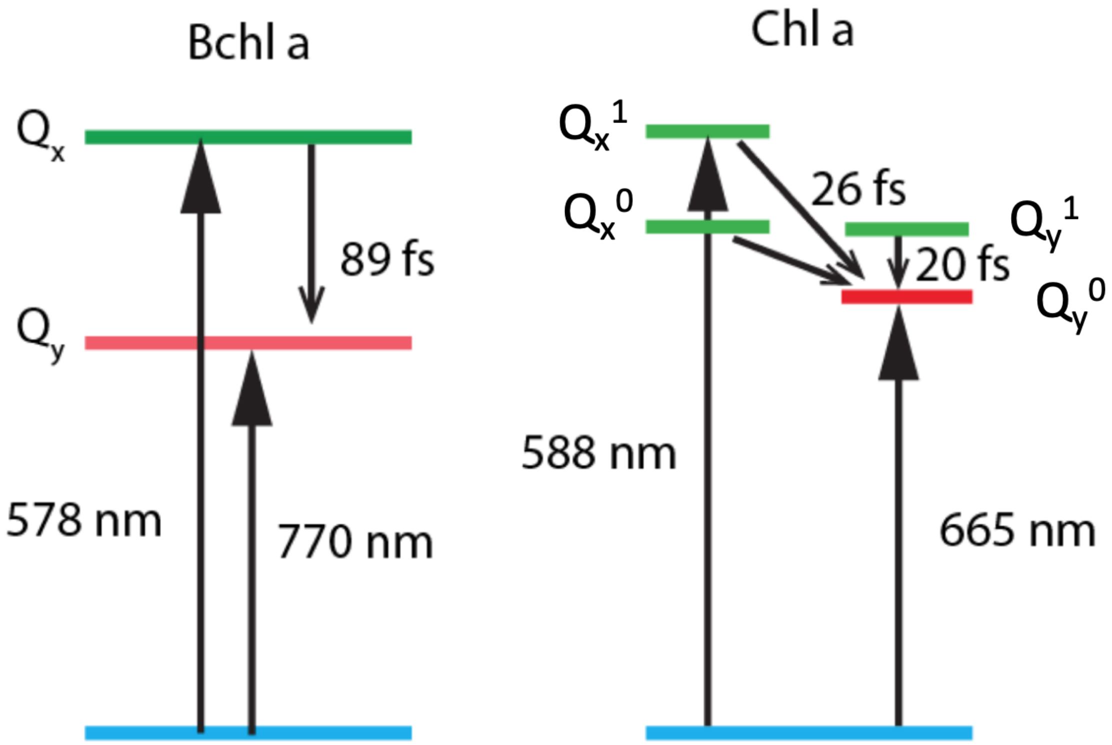

Figure 4.7: Energy diagrams including internal conversion rates for the Q-band of Bchl a and Chl a as found using our P-2DES data and TD-DFT calculations.

From the results of our study, we can at least suggest a possible model for the underlying energy landscape of the Q-band in Bchl a and Chl a, as is shown in Figure (4.7). In this figure, the Chl a $Q_x, 0$ level and $Q_y, 1$ level are energetically close, which leads to internal conversion pathways from $Q_x, 1$,$Q_x, 0$, and $Q_y, 1$ into $Q_y, 0$. The mixing of these states also leads to faster internal conversion than is experienced in Bchl a because of the smaller energy gap. This provides support for the argument to think beyond the Gouterman model.

4.5 Ab initio Calculations

The computational work presented in this chapter was primarily performed by the post-doc Alexander Schubert working in the group of Professor Eitan Geva in the Chemistry Department at the University of Michigan with additional guidance from Barry Dunietz at Kent State University. All of the figures contained in this section were made by Dr. Schubert, with exception of the linear absorption spectra used in panels A and C of Figure (4.8), which were measured by us. Electronic structure was calculated using the Q-Chem software version 4.4 with the group's novel TD-DFT framework with a polarizable continuum model (PCM) using the PCM-optimally-tuned screend range-separated hybrid approach (OT-SRSH-PCM). Details of the method can be found in references [101–111].

Using the OT-SRSH-PCM method, the exchange correlation energy and the electronic excited states of Bchl a and Chl a were calculated with tetra-, penta-, and hexa-coordination with the central magnesium atom in the chlorin ring by including 0,1, or 2 solvent molecules, respectively. In the calculations the phytyl side groups of Bchl a and Chl a were omitted to reduce computational cost. This omission does not influence the resulting spectra since the phytyl groups do not influence the electronic structure in the Q-band. For both pigments, vibrational normal modes for the S_1 and S_2 electronic states were also calculated. Figure (4.8) panels B and D show the Huang-Rhys factors calculated using these methods for Bchl a and Chl a, respectively. Panels A and C of the same figure show the Huang-Rhys factors against the linear absorption spectra of Bchl a and Chl a, respectively. Figure (4.8) panel C shows a clear overlap of the S_1 first vibrational replica (i.e., $Q_{y,1}$, in the context of the Gouterman terminology) and the S_2 fundamental, which forms the E_2 peak in the linear absorption spectrum of Chl a. Moreover, there is an overlap of the S_1 second vibrational replica and S_2 first vibrational replica, corresponding to an overlap of $Q_{y,2}$ and $Q_{x,1}$, leading to the formation of E_3 in the linear absorption spectrum. This finding leads to the energetic placement of $Q_{X,0}$ and $Q_{y,1}$ in our proposed model shown in Figure (4.7).

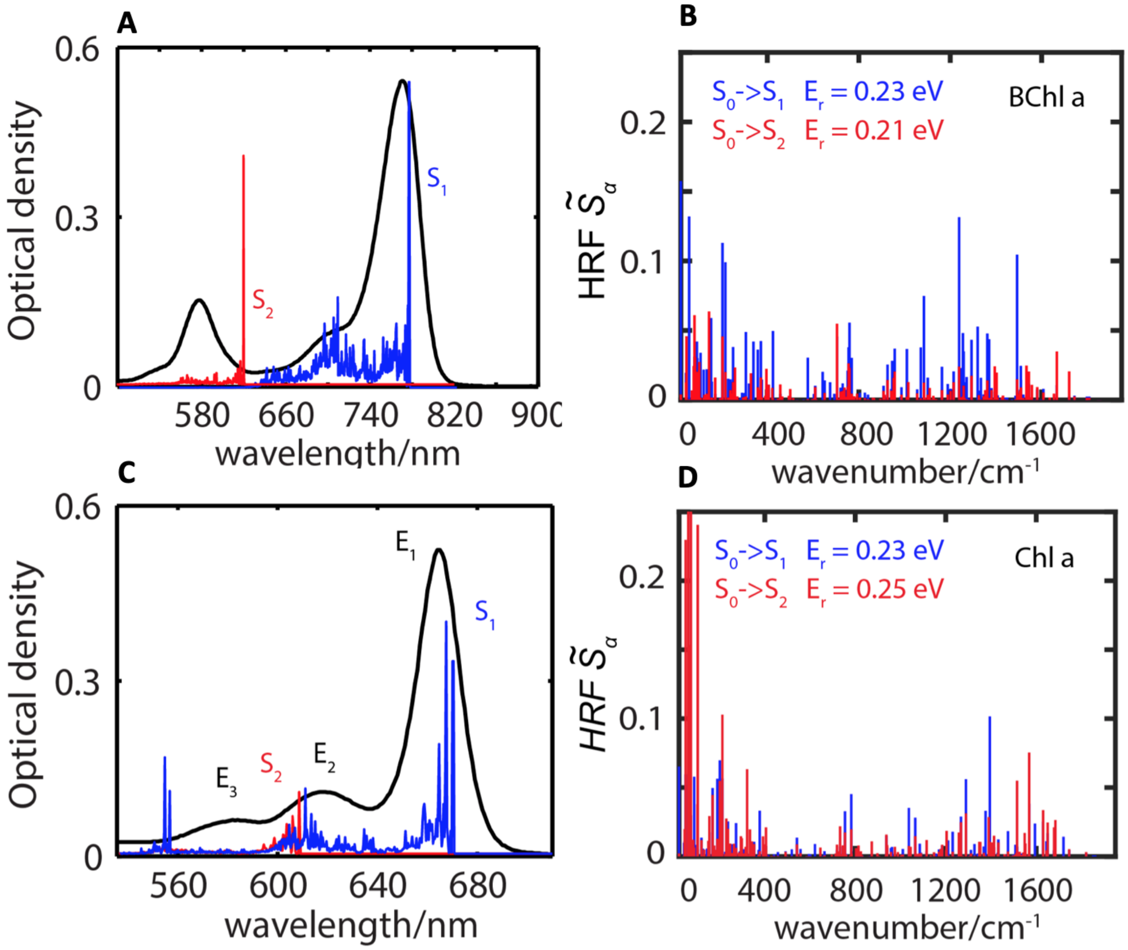

Figure 4.8: Linear absorption spectra of Bchl a (panel A) and Chl a (panel C) with the calculated Huang-Rhys factors for the S_1 and S_2 electronic transitions. Calculated Huang-Rhys factors of Bchl a (panel B) and Chl a (panel D).

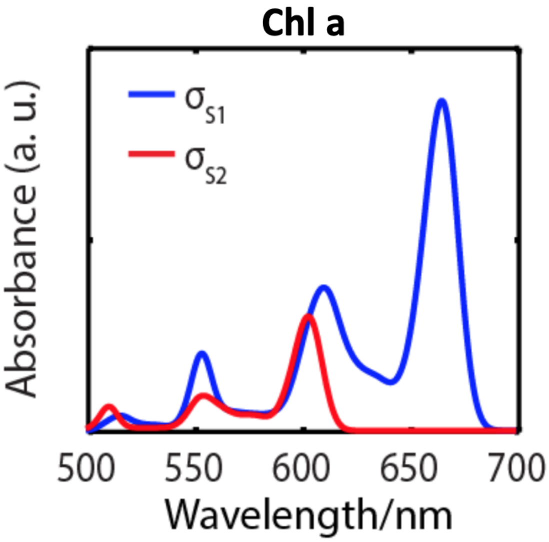

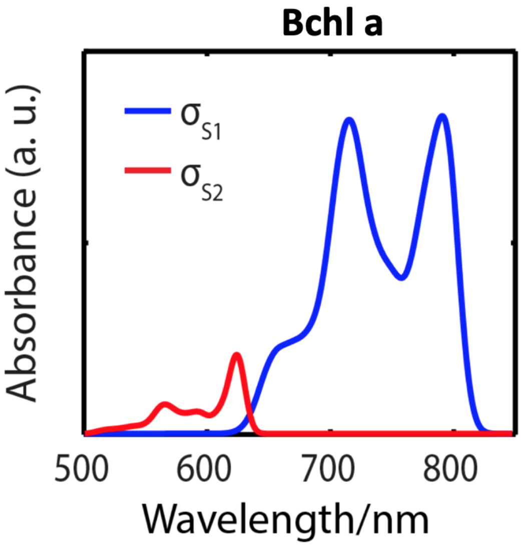

Figure 4.9: Calculated linear absorption spectra with vibrational overtones for the S_1 (blue) and S_2 (red) transitions of Chl a and Bchl a.

Figure (4.9) shows the calculated linear absorption spectra with the vibrational overtones from the S_1 and S_2 transitions of both pigments. These spectra were calculated using the equation:

$$\sigma_i \propto \Omega_{i,S0} \sum_n F_{n,i} f(E_{n,i} - E), i = S_1, S_2 \tag{4.10}$$

where σ_i is the absorption spectrum for the S_1 or S_2 electronic state, Ω is the oscillator strength, $F_{n,i}$ are the Frank-Condon factors determined using the calculated Huang-Rhys factors in Figure (4.8), and $f(E_{n,i} - E)$ is a Gaussian function between the excited and ground state, where the excited state energy was found by including two vibrational quanta. Note the strong overlap of the S_1 overtones with S_2 in Chl a and virtually no overlap with Bchl a. To better visualize this overlap, Figure (4.10) shows the wavelength dependent S_2 contribution normalized to the total at each wavelength. Here it is clear that Bchl a does not have any wavelength dependent overlap of S_1 and S_2, while Chl a experiences greater contribution from S_2 at shorter wavelengths.

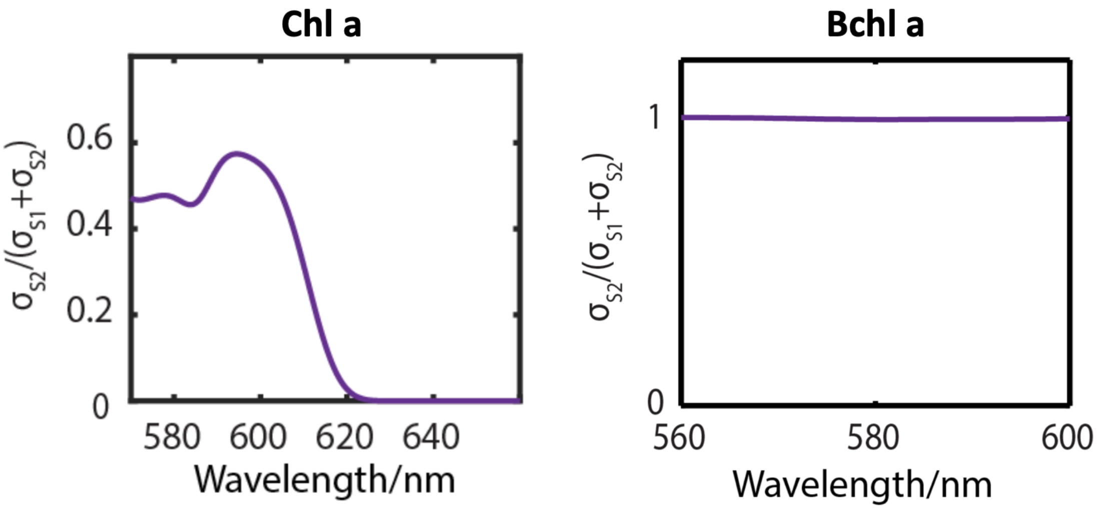

Figure 4.10: Calculations of the S_2 contributions to the total intensity in the calculated linear absorption spectra. Note the strong contribution at shorter wavelengths in Chl a but no wavelength dependence in Bchl a.

Finally, the Fermi's Golden Rule equation used to find the internal conversion rates using the inverse lifetimes τ_{IC} obtained from the data is:

$$V_{el}^2 = \frac{\hbar^2}{\tau_{IC}}\Big\{\int_{\infty}^{\infty} dtExp[-\frac{i}{\hbar}\Delta Et + \sum_{\alpha} -S_\alpha(2n_\alpha+1) + S_\alpha[(n_\alpha+1)e^{-i\omega_\alpha t} + n_\alpha e^{i\omega_\alpha t}]]\Big\}^{-1} \tag{4.11}$$

for the optimized potential energy $\Delta E = S_2 - S_1$, S_α Huang-Rhys factors, and n_α room temperature vibrational mode phonon density with frequency ω_α.

4.6 Conclusions

In conclusion, this study used P-2DES measurements on the photosynthetic pigments Bchl a and Chl a to obtain cross peak specific spectra sensitive to the TDM orientation. This information was used to calculate the relative angle of the TDM as a function of excitation wavelength. It study found the Chl a pigment to have excitation dependence in the relative TDM angle, while Bchl a does not. TD-DFT calculations performed by our collaborators find strong overlap of the higher vibrational levels of the Q_y transition with the Q_x fundamental and lower vibrational levels in Chl a, but virtually no overlap in the case of Bchl a. Estimates of internal conversion rates for the two pigments support the idea that the energetic proximity of the electronic transitions and their vibrational modes in Chl a enables faster energy transfer, while the larger separation in Bchl a slows it down. Overall, these results lend support to theories of vibronic mixing in Chl a, but further studies need to be performed to obtain and definitive conclusion.

CHAPTER 5

Broadband Two-Color 2DES Studies of the PSII RC

In this chapter I briefly present the method used for purifying PSII RC complexes from spinach leaves. Then I explain the optical setup for the broadband two-color 2DES experiment performed on the purified samples. Previous 2DES experiments by our group [36, 38] and others [40, 112] have focused on the Q_y region. Here we excite across the Q_y region and utilize a broadband probe that spans the Q_x and carotenoid transitions. I presents the results of these experiments and discuss how the data illuminates current exciton models and proposed charge separation mechanisms of the PSII RC. This work is currently in the process of being written up and the data is being carefully examined for possible flaws in our interpretation. It is likely that the experiment may need to be performed again before publication to corroborate our current results as the functionality of the cryostat used has recently was called into question during the writing of this thesis. Initial investigation by other lab members suggests that the data may have been taken at 140K instead of the intended 77K.

5.1 Sample Preparation from Spinach

The process to obtain D1-D2-Cytb$_{559}$ reaction center complexes (referred to as PSII RC or RC in this thesis) begins with approximately 40 ounces of store-bought, locally sourced mature spinach leaves and ends with purified RC sample concentrated to experimental conditions. This whole endeavor requires 3-4 days of lab work. Details for the practices I followed can be found in Appendix A of this thesis and of Anton Loukianov's thesis [6]. Here I include a brief description.

The procedure begins by following the method of Berthold, Babcock and Yocum [22] (colloquially referred to as the BBY prep as per the authors' names), whereby de-stemmed spinach leaves are first ground by a blender and then subjected to a series of pelletings and buffer washes. Thylakoid membrane fragments containing PSII complexes (of BBY particles) are extracted and can be stored long term in a -80°C freezer. Frozen BBY particles are thawed and treated with n-dodecyl-β-D-maltopyranoside (β-DM) detergent at room temperature following the procedure described by van Leeuwen [23]. PSII core complexes are retrieved after washing on a Q-sepharose anion-exchange column. Continuing to follow the van Leeuwen procedure, core complexes are treated with Triton-X100 detergent on ice to remove CP43 and CP47 antenna complexes. Isolated D1-D2-Cytb$_{559}$ reaction center complexes are retrieved and diluted with column elution buffer following a second wash on a Q-sepharose anion-exchange column. The purity of the eluted RC is verified by measuring the ratio of the absorption peaks at 417 nm and 435 nm. A ratio of 1.2 ensures the correct 6:2:2 chlorophyll a:pheophytin a: carotenoid stoichiometry of RC pigments [113]. Additionally, this ratio has been shown to be sensitive to unbound chlorophyll or pheophytin pigments or other excess complexes that may compromise the purity of the sample [113]. The linear absorption spectra for the four major steps in the purification process are show in Figure (5.1).

At this point the dilute RC sample is concentrated in a centrifuge. It then undergoes a buffer exchange with a storage buffer containing a weak concentration of β-DM to stabilize the complexes for long term storage (RC samples are reported to degrade over time when not prepared with β-DM). Finally, the RC samples are further concentrated such that the OD measured at 544 nm (pheophytin Q$_x$ 0-0 peak) will measure 0.1-0.2 at room temperature (and therefore $\sim$0.3 at 77 K) for a pathlength of 380 μm when at a 50% dilution with glycerol-ethylene glycol 1:1 (volume:volume) cryo-protectants.

5.2 Experimental Setup of Continuum Probe 2DES

The primary objective in studying the PSII RCs is to understand its structure-function relationship and to resolve its highly efficient charge separation mechanism. To that end, we perform 2D excitation spanning the Q_y band to initiate the charge separation process and employ a broadband visible continuum to probe Q_x excitonic structure and the charge separation intermediates. These measurements require two separate light sources covering different regions of the visible spectrum. Such spectral ranges are typically challenging to cover simultaneously. However, these experiments were performed in the Laboratory for Ultrafast Multidimensional Optical Spectroscopy (LUMOS) at the University of Michigan, which has perfected the ability to control the timing and pulse compression of highly stable light sources covering the electro-magnetic spectrum from UV to near IR regions [15].

Experiments on the PSII RCs were carried out in the pump-probe geometry, as depicted in Figure (3.14) in Chapter 3, with a continuum probe [114]. The laser source is a Spectra Physics Spitfire Pro regenerative amplifier Ti:Sapphire laser (regen) with an output power of 2 W centered at 800 nm operating at a 500 Hz rep rate to avoid build up of long-lived triplet states in the PSII RC. Immediately after the laser output, the regen beam was split into separate pump and probe paths. The pump path seeded a home-built non-collinear optical parametric amplifier (NOPA) [115]. The NOPA was tuned to have a central wavelength at 655 nm with a bandwidth covering 620-680 nm. The pump pulse temporal profile from the NOPA was precompressed using a grism [69]. Following the grism, further pulse manipulations were made with a Fastlite Dazzler acousto-optic modulator, which enables control over both the amplitude and phase of the pump pulses [116]. Such control is essential in performing two-dimensional spectroscopy as it allows for the generation of the two pump pulses and executes the scan that define the t_1 axis. Additionally, it can apply a relative phase value to each waveform, thereby enabling the four-step phase cycling that subtracts out undesirable un-modulated signal and separates rephasing and non-rephasing signals (Equation (3.33)). The Dazzler is also used to compress to approximately 20 fs width pulses using the CRT/SPEAR method [117]. Following the Dazzler, the pump beam is focused to a spot size of 100 μm at the sample position.

Prior to the sample, the probe beam is directed to a delay stage that controls the timing of the third experimental pulse which controls the t_2 time delay. Upon exiting the delay stage, the probe beam is focused onto a crystal to generate a continuum white light source [118]. Fused silica ($\Delta\lambda$ = 475-725 nm) and calcium fluoride ($\Delta\lambda$ = 375-725 nm) crystals were both used in separate experiments on the PSII RCs. Light from these continuum sources was too weak and broadband to easily apply methods of pulse pre-compression. Instead, the probe pulse chirp was removed in post-processing as will be described below. Finally, the continuum probe beam is focused at the sample location, where it crosses with the pump pulse and is then coupled into the spectrometer (Horiba Jobin Yvon iHR320). Light into the spectrometer was incident on a grating with a groove spacing of 150 grooves/mm and was then measured with a CCD camera (Pixis, Princeton Instruments).

Both pump-probe and 2D scans were performed on the PSII RCs from -8000 fs up to 1 ns delay times using a semi-log time scale. In the pump-probe scans t_1 is set equal to zero (i.e., the Dazzler diffracts a single pump pulse), and the t_2 axis is scanned by moving the delay stage. ΔA absorption difference measurements were taken where a chopper operating at 250 Hz is used to block every other pump pulse exiting the Dazzler and $\Delta A = A_{unblocked} - A_{blocked}$ is measured at each t_2 point, averaging over 200 spectra for each $A_{unblocked}$. The resulting scans were analyzed using the CarpetView software (by Light Conversion, version 1.1.7-3D). Chirp correction of the probe pulses was also performed in CarpetView by applying a polynomial fit to the chirp profile around $t_2 = 0$. To most accurately apply the chirp correction it is crucial to take fine t_2 steps encompassing the entire chirped profile. This was achieved by scanning from -200 to 1000 fs with time steps of 10 fs for the calcium fluoride crystal and scanning -200 to 500 fs with 20 fs time steps for fused silica.

In 2D scans, unlike their pump-probe counterparts, for each t_2 value the t_1 axis must also be scanned. In addition, for each t_1 point, the four-step phase cycling is performed. Furthermore, 400 spectra are averaged for each phase-cycled waveform. A further 200 spectra for each waveform are also taken with the probe light blocked to subtract out pump scatter signals in post-processing as a way to achieve the best signal-to-noise. Similar to the pump-probe scans, finer t_2 steps ($\Delta t_2 = 20$ fs) are taken for the region across time zero (-200 to 800 fs) to provide the highest resolution from post-processing chirp correction. Post-experimental analysis and chirp correction are executed using custom written MatLab code. The chirp correction follows that described by Tekavec et al. [119] which uses a pump-probe profile to fit a polynomial and apply it over all t_2 values (a numerical equivalent to that used in CarpetView).

As previously mentioned, the PSII RC samples were concentrated such that the OD at 544 nm is 0.1-0.2 at room temperature in a 380 μm path length sample cell. 2D measurements were taken using an Oxford Instruments (MicrostatN) cooled with liquid nitrogen (77K), at which the OD increases to about 0.3. Such high concentrations are necessary for observing signal from the higher energy pigment transitions. However, this means that the OD for the Chl and Phe Q_y transitions covered by the NOPA had OD values nearing 1.0. Signals measured around the Q_y therefore exhibit overpoweringly strong signal and suffer from distorted lineshapes [120]. Detection wavelengths longer than 645 nm were therefore cut out of the 2D spectra and hence excluded from the data analysis to be able to observe the kinetic features of the higher energy transitions.

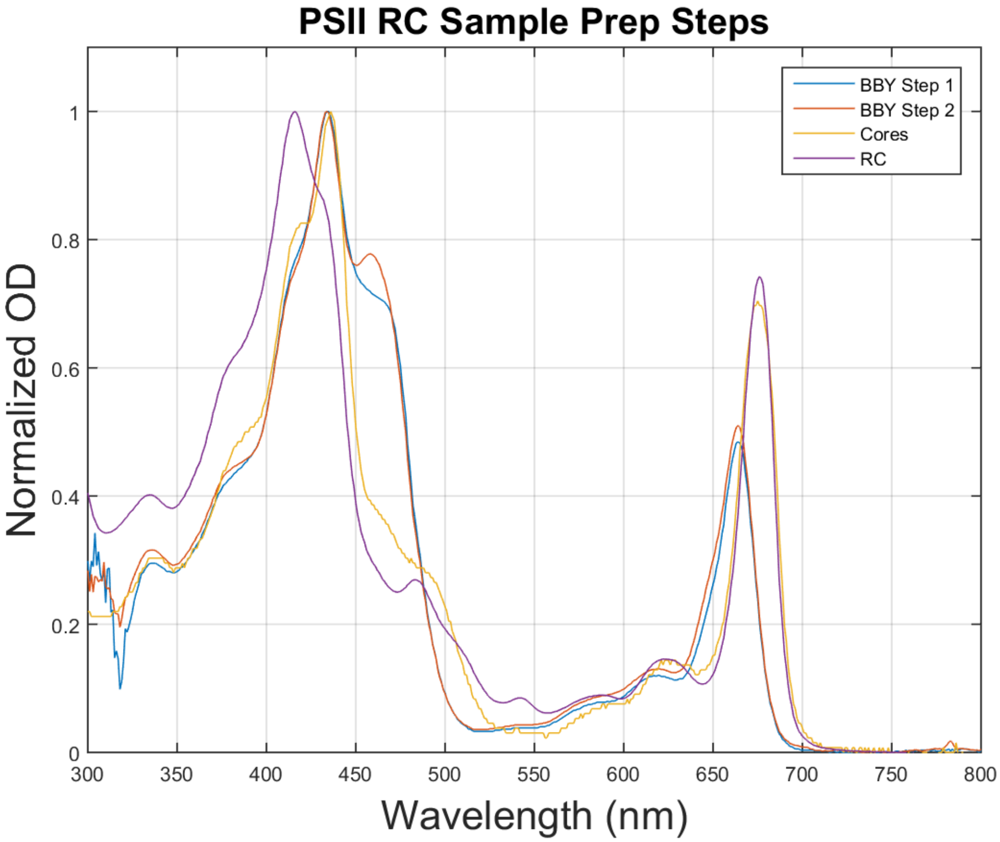

Figure 5.1: Linear absorption for the four main stages of the PSII RC purification preparation.

5.3 Excited State Absorption in the PSII RC

A significant challenge in analyzing the results of ultrafast spectroscopy experiments on the PSII RC, in particular when probing wavelengths shorter than the Q_x region, is the strong contributions from excited state absorption (ESA) [4, 121]. As can be seen by the overwhelming presence of negative signal in Figure (5.2), the measurements in this study are no exception. From this figure, one can discern the expected increase in Phe Q_x 0-0 bleach at 544 nm (18382 cm^{-1}) that appears after a few picoseconds and continues to grow more positive over the length of the experiment, indicating the formation of a charge separated species. Similarly, the 455 nm (21978 cm^{-1}) region, corresponding to the formation of the Phe$^-$ anion state, becomes increasingly negative, in agreement with charge separation models. However, from these plots it is difficult to discern possible bleach contributions from the other pigments that populate this region. A strategy that has been used to remove the ESA contribution has been to employ a constant background subtraction at 557 nm where it is believed that there are no spectroscopic contributions from other pigments [121]. In the original implementation of this method by Greenfield et al. [121], the goal was to specifically view the relative increase in Phe Q_x bleach without the influence of ESA at different waiting times for a transient absorption measurement. It was therefore logical to choose a wavelength close to the feature of interest where it was believed that there were no other pigment contributions. Background subtraction at 557 nm has since been applied to studies measuring a broader probing region, all the way up to 425 nm [4]. Another background subtraction method that has been used on the bacterial reaction center (BRC) over a broad detection bandwidth in a 2D study involved fitting a polynomial to minima along the detection axis corresponding to strong ESA contributions [122]. The robustness of this method in removing wavelength-dependent variable ESA behavior makes it more ideal than implementing a constant background. However, the increased spectral congestion in the PSII RC proved to be much more challenging to implement the polynomial fit method than the BRC case and created more uncertainty in the spectral shapes. We elected to refrain from using the polynomial ESA subtraction method to avoid distortions to the spectra. In our study, we opted for the simpler approach to aid in visualization of absorption features by subtracting a constant background as determined by taking a slice across the excitation axis at 557 nm (17953 cm^{-1}) at each t_2 time point. The resulting 2D data are shown in Figure (5.3). Immediately, one can see absorption peaks corresponding to the pigment transitions indicated in the linear absorption spectrum presented in Chapter 1 (and re-plotted on the right of the figure with labels for the pigment transitions). Namely, these features are Chl Q_x 0-1 at 585 nm (17094 cm^{-1}), Phe Q_x 0-0 at 544 nm (18382 cm^{-1}), Phe Q_x 0-1 at 512 nm (19531 cm^{-1}), Car D2 0-0 at 506 nm (19763 cm^{-1}), Car D2 0-1 at 474 nm (21097 cm^{-1}), and Car D1 0-0 at 489 nm (21978 cm^{-1}).

To highlight the advantage this affords in visualizing the pigment features, Figure

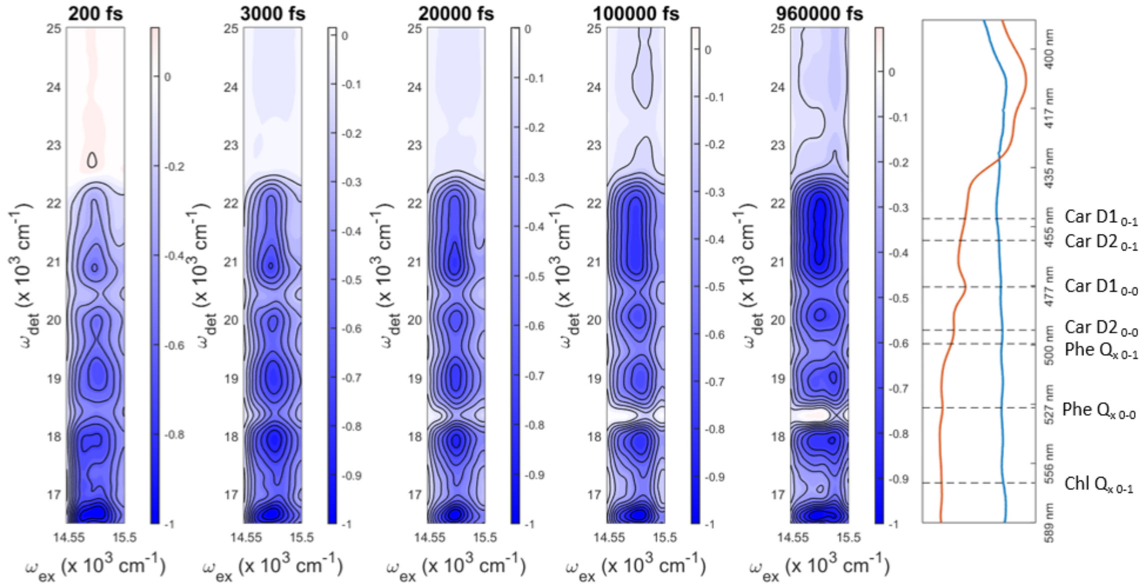

Figure 5.2: 2D plots with strong ESA contribution. Contributions from Phe Q_x 0-0 at 544 nm (18382 cm^{-1}) and radical pair formation from the anion band at 455 nm (21978 cm^{-1}) grow in over time. The right most panel shows the sample linear absorption in orange and probe spectrum in blue with pigment absorption peak labels.

(5.4) shows the background subtracted 2D plot at 100 ps with horizontal lines along the excitation axis corresponding to the pigment features. Vertical lines in this plot represent the exciton transitions obtained from the Gelzinis model. For increased visualization, the linear absorption spectrum is also plotted in the orange line in both the excited (top) and detected (right) regions. The pump and probe spectra are also plotted in blue.

5.4 PSII RC Power Dependent Features

A point of concern when performing ultrafast spectroscopy experiments on the PSII RC in seeking to resolve the kinetics of charge separation is the pump power used in the experiment. A previous transient absorption study by Donovan et al. [123] has shown that the PSII RC can exhibit different decay times, dependent on the pump power. Namely, the study found that using a higher pump power can lead to the presence of faster dynamics, which the authors attribute to contributions from multiply excited states leading to singlet-singlet annihilation. It should be noted that

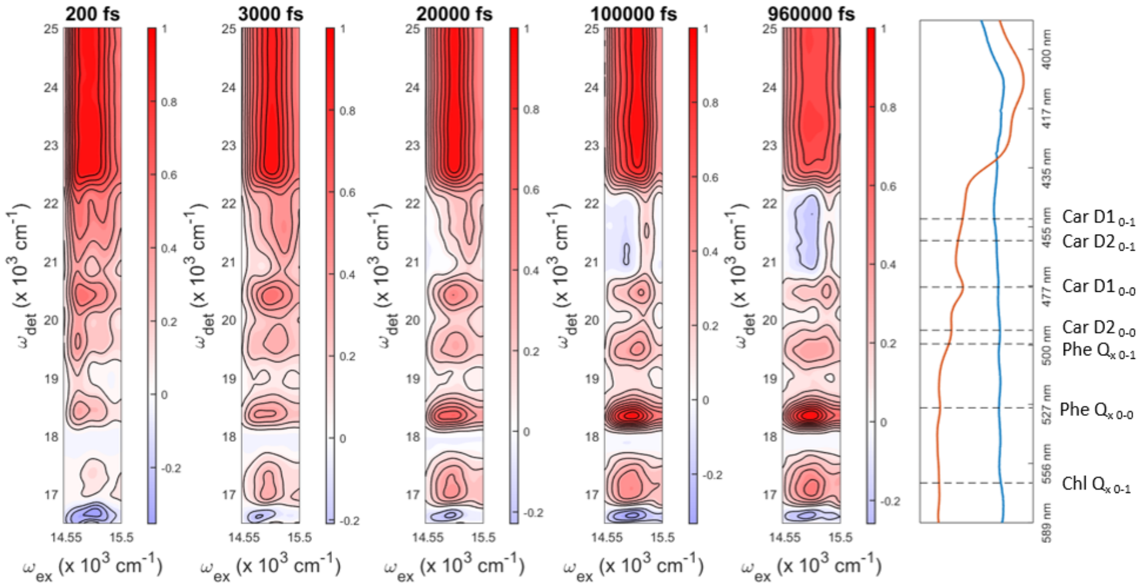

Figure 5.3: 2D plots implementing a constant ESA background subtraction at 557 nm. With the background subtraction, ground state bleach features from RC pigments and the negative anion band contribution at 21978 cm^{-1} become easier to visualize. The right most panel shows the sample linear absorption in orange and probe spectrum in blue with pigment absorption peak labels.

in the Donovan study the authors perform the experiment by pumping in the Soret band region at 400 nm and probing at 680 nm. The authors qualify their conclusion with the caution that pumping in the Soret region could encourage more excitations because of the increased strength of the Chl and Phe cross sections in this region as compared to the Q$_y$ region. Nevertheless, they advocate for performing ultrafast spectroscopy on the PSII RC in a linear power regime to avoid unwanted processes such as exciton-exciton annihilation.

Heeding the advice of Donovan et al., I performed a power study by taking a series of pump-probe measurements using the same pump and probe conditions of the 2D study and varying the pump energy via controls on the Dazzler pulse-shaper. Measurements were taken at 20 nJ, 40 nJ, 50 nJ, 60 nJ, 80 nJ, and 100 nJ pulse energies. Representative kinetics from this study are shown in Figures (5.5) and (5.6). These plots show consistent kinetics over the range of the power used. We therefore performed our 2D measurements using 50 nJ pulse energies, which is comfortably in

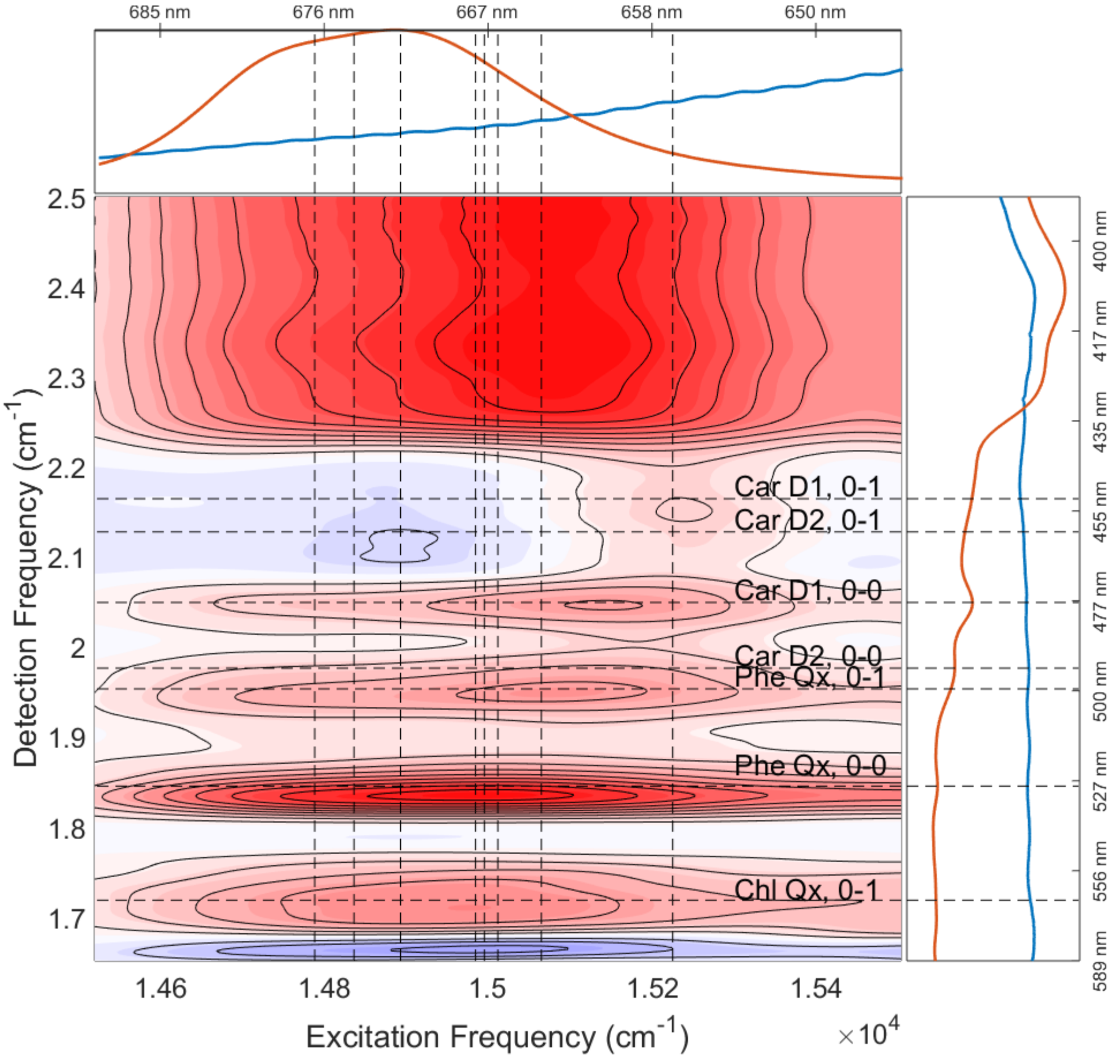

Figure 5.4: 2D plot at 100 ps with horizontal lines indicating relevant pigment absorption peaks and vertical lines indicating Gelzinis model exciton transitions. The plot on the right shows the PSII RC linear absorption (orange) and the probe spectrum (blue). The top plot shows the linear absorption around Q_y (orange) with the pump spectrum (blue).

this linear regime.

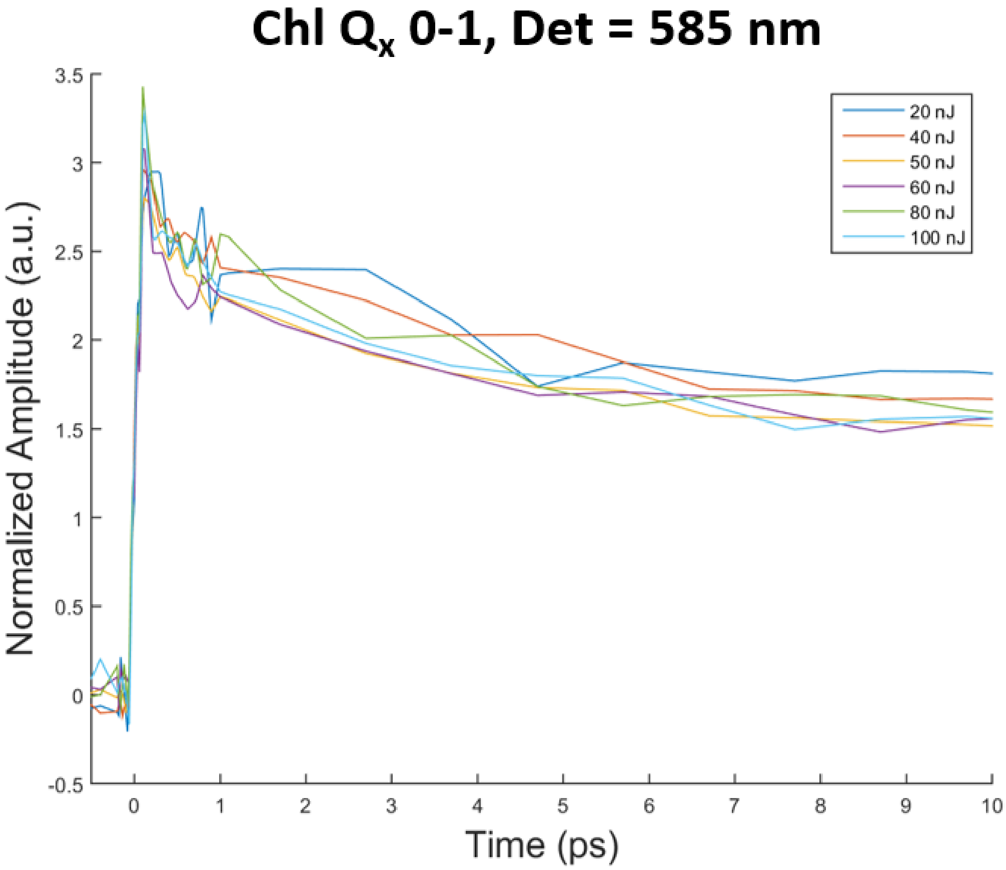

Figure 5.5: Pump-probe traces through the Chl Q$_x$ 0-1 peak at 585 nm varying the pulse energy. Traces are normalized to the value at 50 ps.

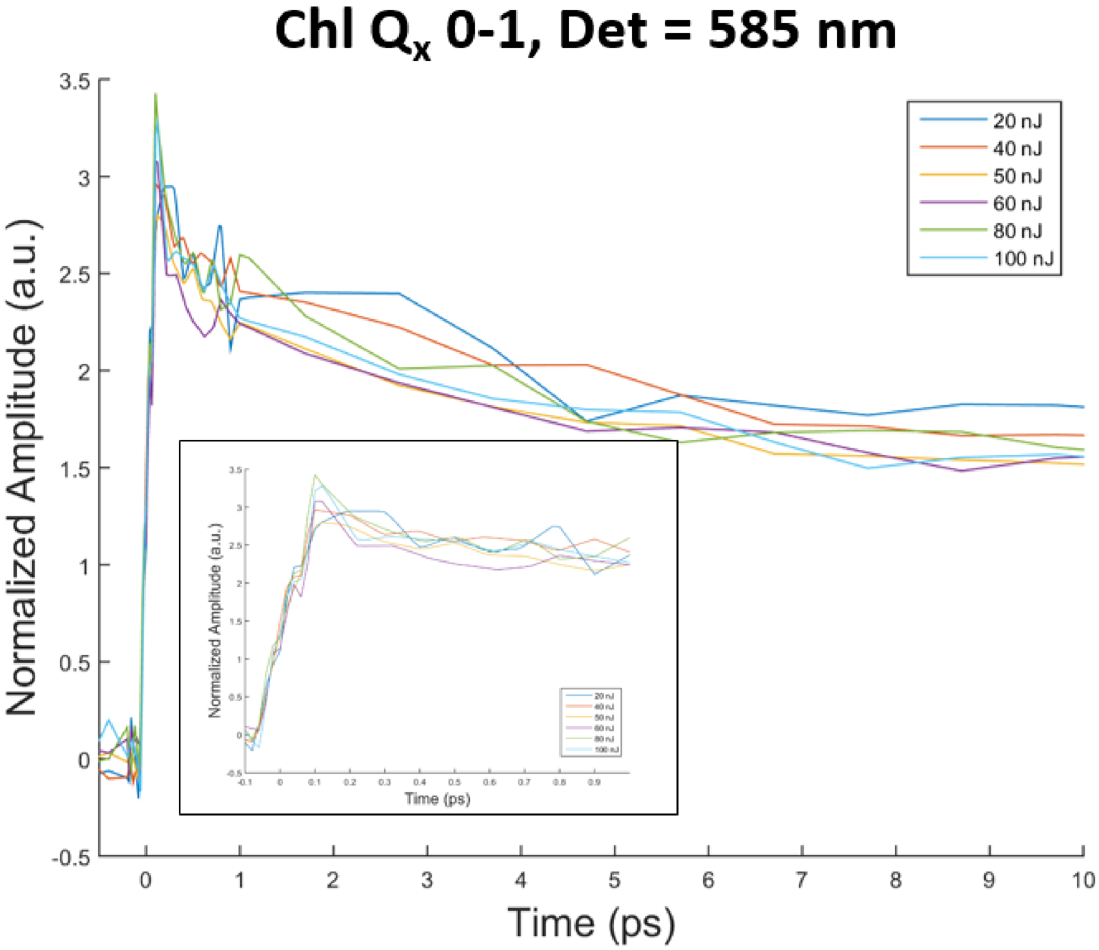

Figure 5.6: Pump-probe traces through the Chl Q_x 0-1 peak at 585 nm varying the pulse energy showing times out to 10 ps and 1 ps (inset).

5.5 Evaluating Exciton Models Using Excitation Dependence of 2DES

One of the main advantages of the Q_y pump, broadband probe 2D experiment is the ability to resolve the excitation dependence of cross peaks of pigment transitions outside of the Q_y region. This becomes particularly useful when seeking to understand the contributions from the Chl and Phe pigments, which suffer from spectral congestion in Q_y, but have better spectral separation in Q_x (see Chapter 1). In the context of exciton models, the excitation dependent information obtained in a 2D measurement allows for insight into the pigment contributions of the excitonic states.

Below I compare the different exciton models against slices along the excitation axis at the detection frequencies corresponding to the ground state bleach of the Chl Q_x 0-1 and the Phe Q_x 0-0 transitions.

Tables (5.1),(5.2),and (5.3) present the percent contribution of the pigments in the designated model for each exciton in the model. These values were calculated from the eigenvector matrix that results from diagonalizing the Hamiltonian presented in Chapter 2 for each model (Table (2.1)). The square root of each element was taken and then the fractional contribution of each pigment was determined from the total for each exciton. The sum of the percent contributions from all the chlorophyll pigments was taken to indicate the Total Chl, as indicated in the third column from the right. The same was done for the Phe contribution. The right-most column indicates if the exciton has a greater than 25% contribution from Phe. This value is used as an arbitrarily assigned benchmark to indicate the excitons with "high" Phe concentration. This value seems appropriate when considering the total Chl concentration is tallied from 6 pigments, while the total Phe contribution is tallied from only 2 pigments.

To directly compare how the predicted exciton composition compares with the experimental data, Figures (5.7),(5.8), and (5.9) show a top panel of sticks representing the exciton transition wavelengths with a bottom panel showing excitation dependent slices of the ground state bleach for Chl Q_x 0-1 at a detection wavelength of 585 nm (17094 cm^{-1}) and Phe Q_x 0-0 at a detection wavelength of 544 nm (18382 cm^{-1}). The exciton sticks are colored red if they have a >25% Phe contribution, and blue if not.

In Figure (5.7) we consider the Gelzinis model in which there are three distinct exciton clusters; excitons 2-4 cluster around the Phe peak with excitation dependence at 675 nm, excitons 5-8 around the Chl peak at 666 nm, and exciton 9 is alone at 657 nm. Of the 2-4 exciton cluster, excitons 2 and 3 favor Phe, as might be expected. Exciton 4 favors Chl, which falls to the red edge of the Chl peak. In the 5-8 excitons, 6 and 7 contain substantial Phe content, but their predicted excitation wavelengths are in poorer agreement with the data, which exhibits a shoulder in the Phe Q_x 0-0

Gelzinis Model													
nm	Exciton	PD1	PD2	Chl D1	Chl D2	Phe D1	Phe D2	Chl z D1	Chl zD2	CT	Total Chl	Total Phe	>25% Phe
703	Ex 1	3.7	4.3	22	0.4	19.4	0.7	0.4	0.3	48.6	31.1	20.1	No
676.2	Ex 2	7.9	15.6	29.3	4.4	18.7	8.8	3.5	0.7	11.1	61.4	27.5	Yes
674	Ex 3	13.5	10.3	11.6	16.4	6	31.8	1.9	3.7	4.7	57.4	37.8	Yes
671	Ex 4	25.8	27.7	15.1	1.3	4.7	15.4	1.6	2	6.4	73.5	20.1	No
667.3	Ex 5	1.2	5.6	11.5	5.6	17.3	2.7	45.5	1.9	8.7	71.3	20	No
666.9	Ex 6	3.4	9.4	16.4	11	28	6.2	11.8	0.3	13.5	52.3	34.2	Yes
666.3	Ex 7	10.4	11.9	9	29.1	11.2	15	2.9	4.6	5.9	67.9	26.2	Yes
663.8	Ex 8	1.5	3.9	2.5	10.8	3.7	5.6	3	67.2	1.8	88.9	9.3	No
656.8	Ex 9	31.1	28.1	12.6	16.5	1.7	1.8	1.7	1.9	4.6	91.9	3.5	No

Table 5.1: Table of the percent pigment participation from the Gelzinis exciton model [3]. Percentages were calculated based off the eigenvectors from diagonalizing the Hamiltonian presented in Chapter 2. Contributions from all 6 of the Chl pigments are summed to indicate the total Chl contribution. The same was done for the Phe D1 and D2 pigments. A label of “yes” or “no” indicates the excitons with a greater than 25% contribution from the two Phe pigments. The left-most column lists the transition wavelength of the corresponding exciton.

van Grondelle Model													
nm	Exciton	PD1	PD2	Chl D1	Chl D2	Phe D1	Phe D2	Chl z D1	Chl zD2	CT	Total Chl	Total Phe	>25% Phe
672.2	Ex 1	16.1	18	20.6	10.7	10.1	9.1	1.6	0.9	12.9	67.9	19.2	No
669.3	Ex 2	14.2	12.3	14.7	10.1	18.1	9.2	1	1	19.4	53.3	27.3	Yes
667.5	Ex 3	15.5	11.7	16.3	12.2	19.2	12.1	2	1.4	9.5	59.1	31.3	Yes
665.1	Ex 4	14.1	16.4	9.7	17.3	8.9	25.1	1	2.7	4.7	61.2	34	Yes
659.5	Ex 5	4	17.5	6.1	32.2	7.4	25.1	0.1	0.6	7	60.5	32.5	Yes
654.3	Ex 6	10.9	8	19.8	7.6	22.1	3.4	1.5	0.8	26	48.6	25.5	Yes
647.2	Ex 7	24.9	24.6	12.7	13.6	4.9	2.9	2.8	5.1	8.4	83.7	7.8	No
645.8	Ex 8	9	9.1	4.3	2.2	1.5	6.1	1.3	63.8	2.7	89.7	7.6	No
642.9	Ex 9	6	5.6	3.9	2.6	6.3	0.6	71.6	0.9	2.6	90.6	6.9	No

Table 5.2: Table of the percent pigment contribution from the van Grondelle exciton model [9].

Renger Model										
nm	Exciton	PD1	PD2	Chl D1	Chl D2	Phe D1	Phe D2	Total Chl	Total Phe	>25% Phe
679	Ex 1	9.2	19.1	38.6	5	19	9	71.9	28	Yes
676.1	Ex 2	20.6	17.5	12.6	17.9	3.2	28.1	68.6	31.3	Yes
674.6	Ex 3	24.1	24.2	12.3	10.5	5.9	23.1	71.1	29	Yes
669.7	Ex 4	8.8	16.1	3.4	33.7	17.6	20.3	62	37.9	Yes
669.5	Ex 5	9.6	5.8	18.1	18.3	37.6	10.6	51.8	48.2	Yes
660.3	Ex 6	31.4	31.3	13.6	17.1	4	2.6	93.4	6.6	No

Table 5.3: Table of the percent pigment participation from the Renger exciton model [7].

slice to the blue of their predicted wavelengths. Exciton 9 falls over the blue shoulder of Ph Q_x at ∼657 nm, which is in disagreement with our data when considering that it is composed of 92% Chl content. Overall, the Chl content of the Gelzinis model is spread throughout the Q_y band but has larger contributions on the blue side. The trend is in rough agreement with the data extracted at the Chl Q_x 0-1 ground state bleach position.

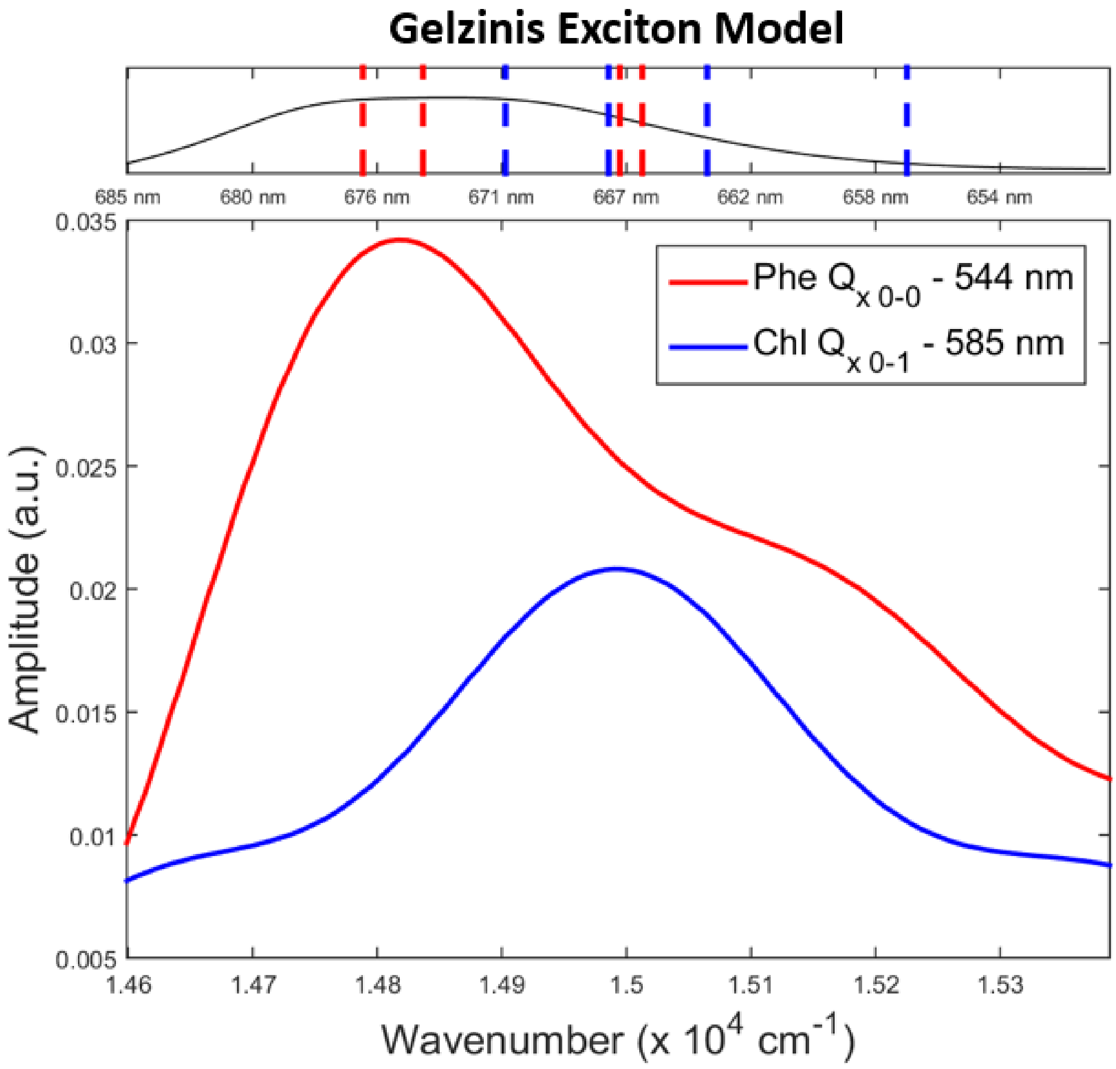

Figure 5.7: **Gelzinis Model -** Excitation dependent slices of Phe Q_x 0-0 (red) and Chl Q_x 0-1 (blue) transitions. The panel above shows the 676.2, 674, 671, 667.3, 666.9, 666.3, 663.8, 656.8 nm excitons in order from left to right with the sample linear absorption in black. Exciton sticks in red indicate a >25% Phe contribution. The lowest energy 703 nm exciton is omitted since it does not fall within the excitation region.

In comparison with the Gelzinis model, the van Grondelle model exhibits less clustering of the exciton transitions (Figure (5.8)). In addition, the three highest energy excitons 7-9 are out of the resolvable range. A reason for the observed shift of the exciton transitions to higher energy is the fact that the van Grondelle model as presented in literature [9] does not include the reorganization energy in the site energies reported (as discussed in Chapter 2). The authors make note of this, and indicate that should the reorganization energy be included, the exciton transition values will red shift. However, the authors fail to report exactly how much of a red shift it would be and point out that the amount would not be uniform for each exciton. This is further complicated by the fact that the coupling values used in the Hamiltonian are not in fact those presented by the authors, but ones estimated by another group [48]. All of this makes it difficult to determine how this model compares with the results of our study without making gross assumptions. Nonetheless, in rough agreement with our data, we see that the excitons with the largest Phe content have lower energies than the majority of the other exciton states. This is consistent with the maximum of the Phe Q_x 0-0 slice lying on the red side of the Q_y band and the maximum of the Chl Q_x 0-1 lying on the blue side.

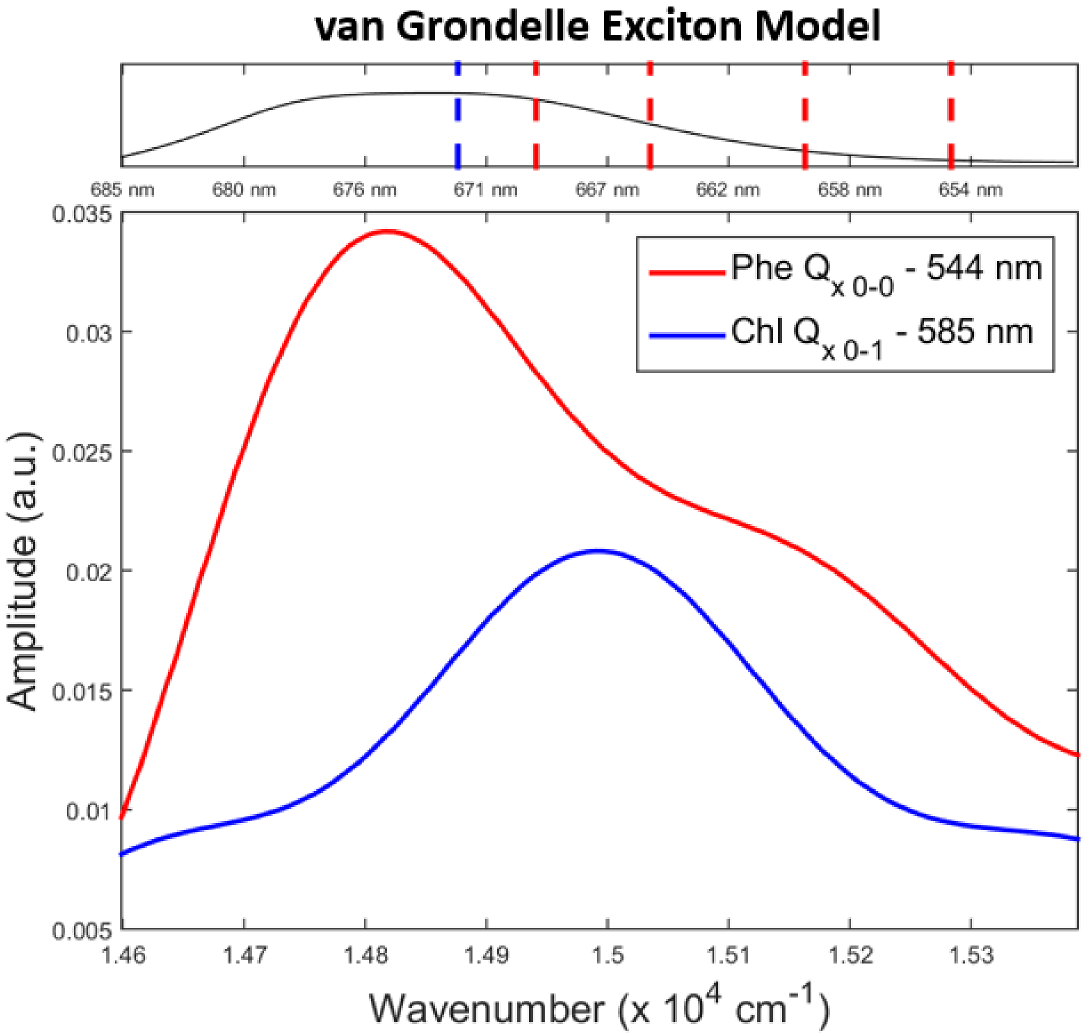

Figure 5.8: **van Grondelle Model** - Excitation dependent slices of Phe Q_x 0-0 (red) and Chl Q_x 0-1 (blue) transitions. The panel above shows the 672.2, 669.3, 667.5, 665.1, and 659.5 nm excitons in order from left to right with the sample linear absorption in black. Exciton sticks in red indicate a >25% Phe contribution. The higher energy 654.3, 647.2, 645.8, and 642.9 nm excitons are omitted since they do not fall within the excitation region.

Figure (5.9) shows the comparison of the Renger model excitons with the excitation slice of Chl and Phe. Similar to the Gelzinis model, the lowest energy exciton is strongly favored by Chl, despite the excitation slices showing strong contributions from Phe in this region. Excitons 2 and 3 are centered nicely over the Phe peak and both favor Phe. Excitons 5 and 6 also favor Phe, but fall in a region with strong overlap of the Phe and Chl peaks. Interestingly, none of the excitons in the Renger model are centered over the Chl peak. Exciton 6 also falls in a region with more Phe contribution but has composition from the blue shoulder at 657 nm that strongly favors Chl.

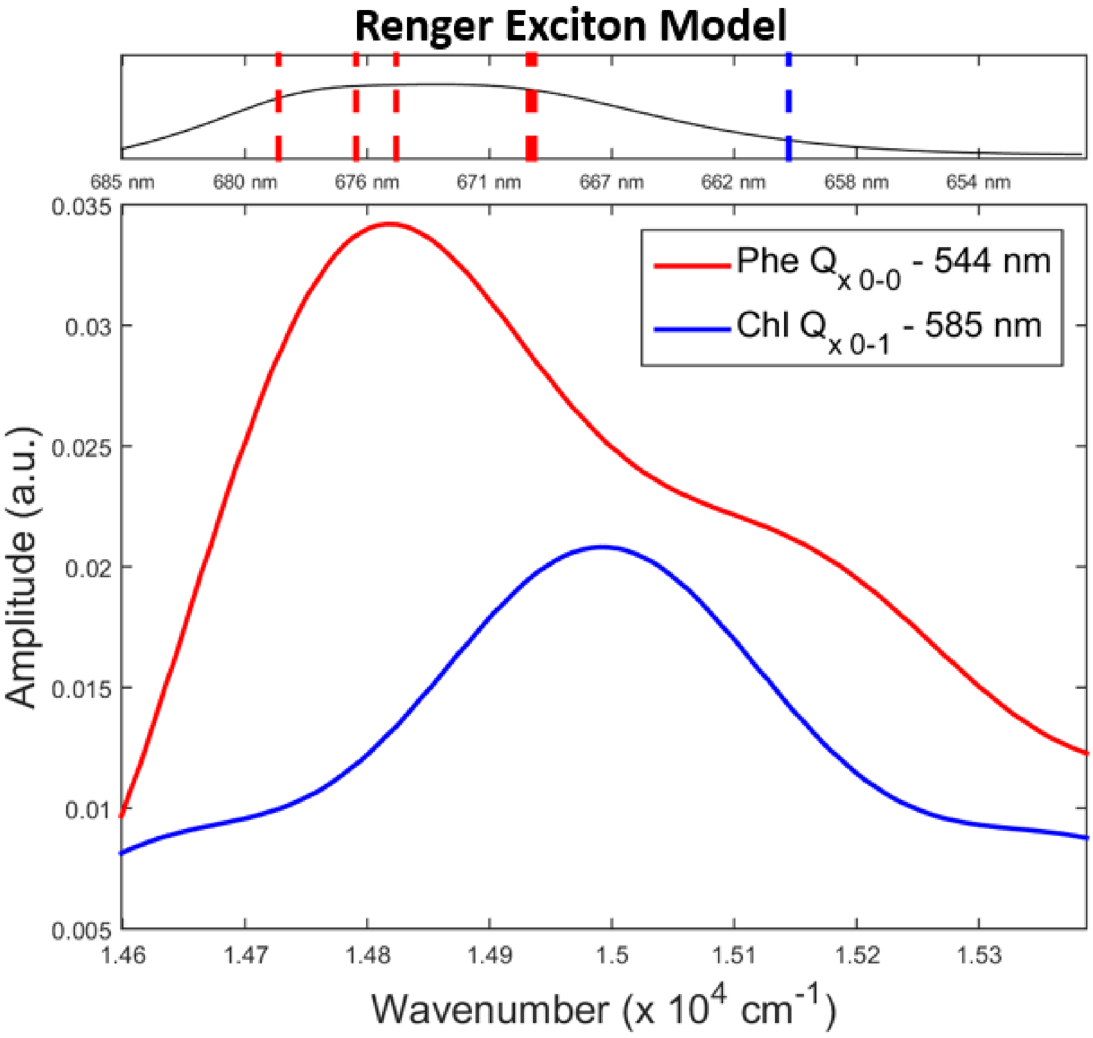

Figure 5.9: **Renger Model -** Excitation dependent slices of Phe Q_x 0-0 (red) and Chl Q_x 0-1 (blue) transitions. The panel above shows all the excitons of the model which have transitions at 679, 676.1, 674.6, 669.7, 669.5, and 660.3 nm in order from left to right with the sample linear absorption in black. Exciton sticks in red indicate a >25% Phe contribution.

From the exciton models evaluated in this thesis, no one model seems to stand out as an indisputable match with the data. A notable similarity between all of them is that the highest energy excitons favor Chl and yet none of these excitons have transitions near the Chl peak. On the other hand, the lowest energy excitons of the Gelzinis and Renger models favor Phe, and these transitions fall in regions with more Phe than Chl contribution. For these reasons, and based on the information provided for these models, the data appears to support the Gelzinis and Renger models best.

5.6 Testing the Two-pathway Model of Charge Separation in the PSII RC

The leading kinetic model describing the primary charge separation mechanism for the PSII RC was developed by Romero et al. [4]. To form this model, the authors perform a series of transient absorption experiments at 77K, using a continuum probe (425-730 nm), and a pump spectrum with a 5 nm bandwidth that is incrementally scanned across the Q_y band from 655 nm to 695 nm in subsequent experiments. The authors then performed a global analysis, simultaneously fitting to the measurements taken at each excitation wavelength. Their global analysis method defines the number of compartments, or species (such as the charge separated states in the PSII RC), believed to exist with certain lifetimes. Exponential functions are then fit to the data in sequence, in parallel, or a combination of both sequential and parallel pathways to find the lifetimes with which one species evolves into another. Evolution associated difference spectra (EADS) represent the difference spectra of species that exist at generic times without assigning a specific pathway. Upon correctly resolving a sequential scheme with increasing lifetime values the EADS becomes a species associated difference spectrum (SADS) [32]. The Romero study relies on the results of their EADS to draw two significant conclusions: 1) the Chl D1 pathway is not unique, prompting the proposal of a parallel PD1 pathway; 2) auxiliary Chlz's also transfer energy into the RC on a time scale of ∼20 ps. These conclusions leads the authors to suggest a combined parallel-sequential model (depicted in Figure (5.10)) involving 8 compartments, in which energy from the D1 and D2 Chlz's contribute to both the Chl D1 and PD1 pathways on ∼25 ps timescales. At the same time, the two pathways experience an initial fast transfer from an excited state, (Chl D1 Phe D1)* for the Chl D1 path and (PD1 PD2 Chl D1)* for the PD1 path, to their primary charge separated states, Chl D1$^+$Phe D1$^-$ and PD1$^+$Chl D1$^-$ for the Chl D1 and PD1 paths, respectively. Both pathways then relax to the same secondary charge separated state, PD1$^+$Phe D1$^-$, which subsequently relaxes over long time scales to (PD1$^+$Phe D1$^-$)$_{relaxed}$ state.

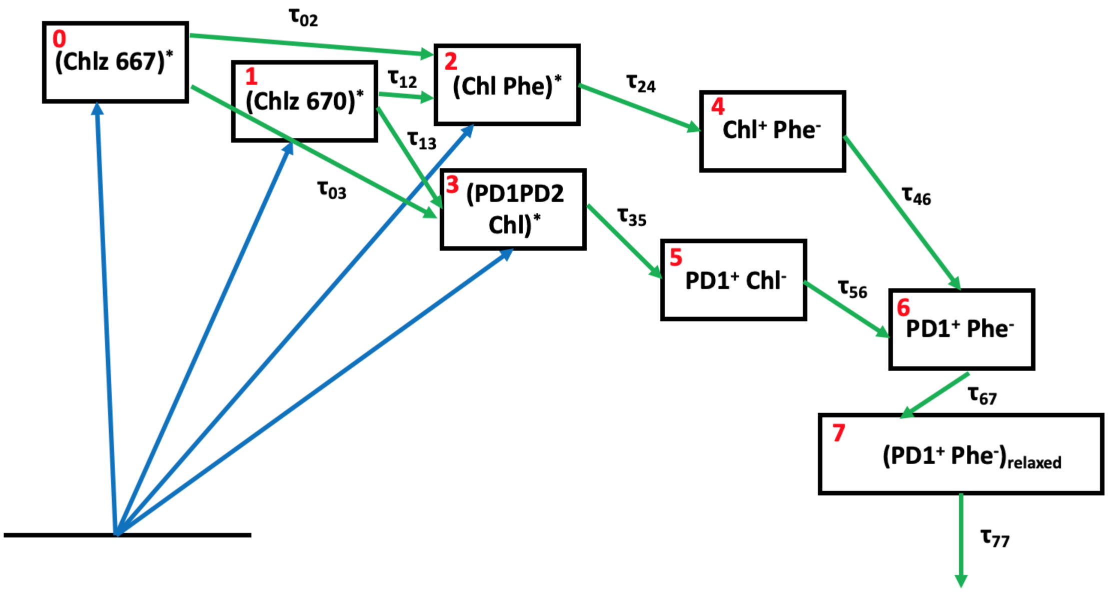

Figure 5.10: **8 Compartment Model Kinetic Pathway** proposed by Romero et al. [4]. This model includes the Chl D1 (compartments 2 & 4) and PD1 (3 & 5) pathways that exist in parallel.

In an attempt to evaluate the validity of the two-pathway model (also described in Figure (1.6)), I performed 2DES experiments with a pump covering the entire Q_y band and continuum probe over the visible spectrum (Figure (3.15)). This experiment essentially mimics the Romero experiment but with the added advantage of continuous excitation across Q_y. This reduces noise contributions from laser fluctuations between experiments and affords the excitation selectivity and time resolution of 2D spectroscopy. Data from the 2D experiment was analyzed using using the Carpetview software to fit the kinetic pathways in Figures (5.10) and (5.15).

8 Compartment Model Lifetimes										
	τ_{02}	τ_{12}	τ_{03}	τ_{13}	τ_{24}	τ_{35}	τ_{46}	τ_{56}	τ_{67}	τ_{77}
Romero Lifetimes	25 ps	25 ps	25 ps	25 ps	3 ps	1 ps	58 ps	37 ps	500 ps	17 ns
Float Lifetimes	23 ps	23 ps	27 ps	27 ps	2.5 ps	0.7 ps	68 ps	47 ps	400 ps	19 ns

Table 5.4: **8 Compartment Model Lifetimes** reported by Romero et al. [4] and lifetimes found allowing the values to float in the Carpetview software after performing a global analysis on the broadband probe 2D data.

In my initial analysis, I applied the 8-compartment kinetic model (schematically represented in Figure (5.10)) proposed by Romero et al. [4] and generated 1D SADS similar to those in the study, performing the analysis using the lifetime values reported in their paper (re-printed in Table (5.4)) and allowing the values to float (also in Table (5.4)). SADS can be generated from our 2D data by recognizing that a 2D spectrum, which is a function of the excitation frequency ω_{ex}, detection frequency ω_{det}, and t_2 scan time, can be expressed as a sum of n species that are each a product of a time-dependent concentration and a frequency-dependent basis functions [13]:

$$S(\omega_{ex}, \omega_{det}, t_2) = \sum_{i}^{n} C_i(t_2) f_i(\omega_{ex}, \omega_{det}). \tag{5.1}$$

In performing the global analysis, the time and frequency variables are separated to find the spectra of each species after a given lifetime. By integrating across the excitation axis of the 2D SADS that resulted from this analysis, I was able to recover 1D SADS spectra to directly compare my results with the Romero study. Although the Romero study reports that a constant background was taken at 557 nm to improve visualization of the bleach features, the spectra presented all show positive features at that wavelength, suggesting a background was not in fact subtracted out. Because of this, I performed the analysis on data without taking a background at 557 nm. In addition, I truncated the excitation and detection axes of the data to mimic the Romero study as closely as possible. The global analysis was therefore performed on a data set with an excitation range of 655-690 nm and a detection range of 400-609 nm. Quality of the Carpetview fitting was evaluated by examining the kinetic traces through time for a given excitation and detection point (Figure (5.19)). Carpetview produces 2D species associated difference spectra (SADS) for each compartment, revealing the spectral features of the various intermediate states in the model. These data were then read by a Matlab script and integrated along the excitation axis to produce 1D SADS that could be compared with those reported by Romero et al. [4].

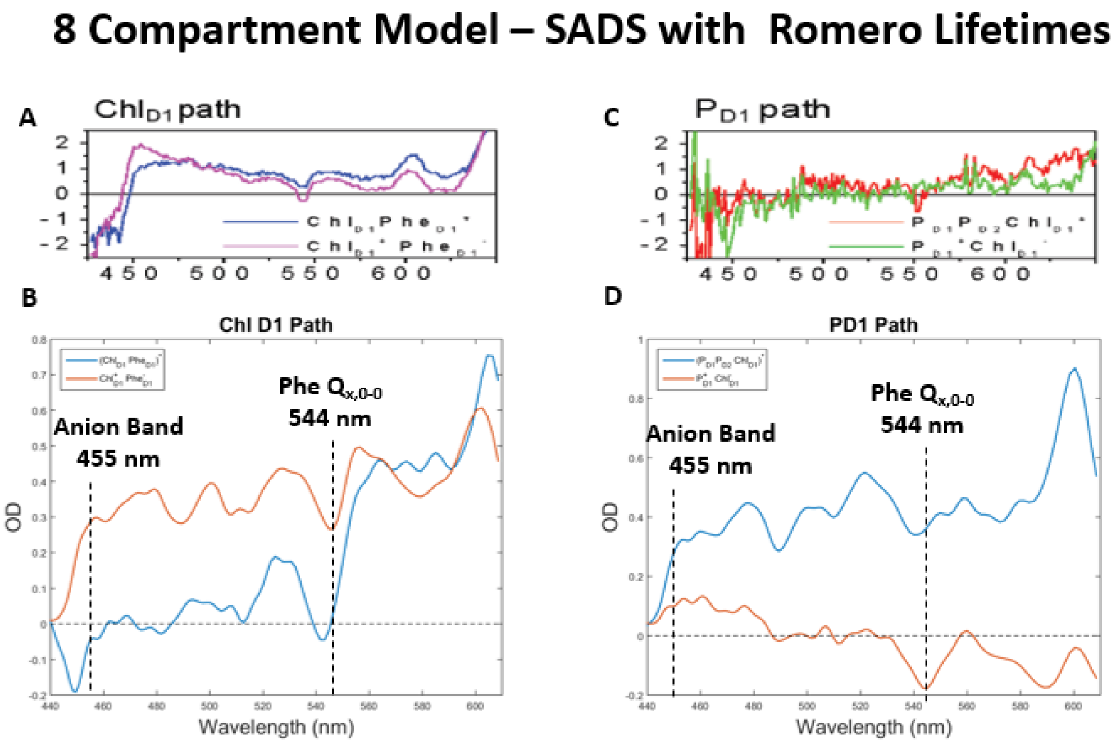
8 Compartment Model – SADS with Romero Lifetimes

Figure 5.11: **8 Compartment Model** - comparing the SADS spectra for the Chl D1 and PD1 pathways reported by Romero et al. [4] (panels A and C) and the SADS spectra obtained in this study (panels B and D) applying the Romero lifetime values from Table (5.4).

Figure (5.11) shows the resulting 1D SADS obtained using the lifetime values reported by Romero et al. for the Chl D1 and PD1 pathways using the 8 compartment model. Based on the pigments and charge separated states involved, it is expected that the Chl D1 pathways will show a bleach at 544 nm, corresponding to Phe Q_x 0-0 transition, which indicates either an absorption event or that the pigment is reduced following delocalized excitation over (ChlD1 PheD1)*. This bleach should then become stronger (i.e., increasingly negative in the 1D SADS) and show increased contribution from the anion band at 455 nm (i.e., increasingly positive in 1D SADS) with the formation of the ChlD1$^+$PheD1$^-$ primary charge separated state (Figure 5.11, panel A). The results from my study when applying the Romero model and lifetimes (Figure (5.11), panel B) instead show the Phe Q_x bleach to decrease between the two species of the Chl D1 path and an overall rise in the spectrum between 450 and 540 nm, rather than a selective increase in the anion band region. In the case of the PD1 pathway, one expects no bleaching of Phe Q_x or anion band contributions since both are signatures originating from the Phe pigment, which is not active in this pathway (Figure (5.11), panel C). However, results from my study show contributions from both (Figure (5.11), panel D).

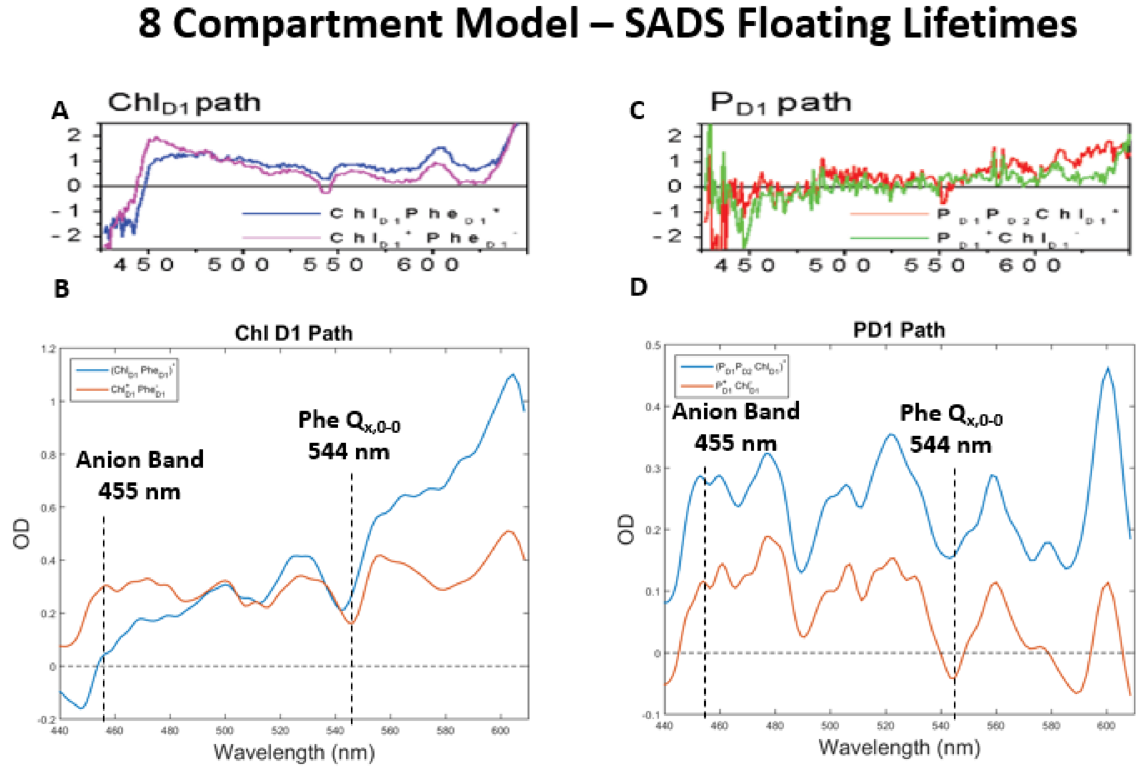

Figure 5.12: **8 Compartment Model** - SADS spectra for the Chl D1 and PD1 pathways obtained using Carpetview after allowing the lifetimes to float (panels B and D) compared with the SADS obtained by Romero et al. (panels A and C). Recovered lifetime values are listed in Table (5.4).

The expected spectral characteristics for the two pathways seem to improve slightly when the lifetimes values are allowed to float (Figure 5.12). In the Chl D1 pathway (panel B), there is a clear increase in the Phe Q_x bleach and the anion band region between the first and second species, as is expected. However, the Phe Q_x feature seems to exhibit red-shift between the first and second species, which is not expected. Additionally, in considering the SADS of the PD1 path, there are clear Phe Q_x contributions, which should not exist in this path. Hence, there is still a lack of complete agreement between the expected qualitative features corresponding to the expected physical processes and those recovered from our data analysis for this model.

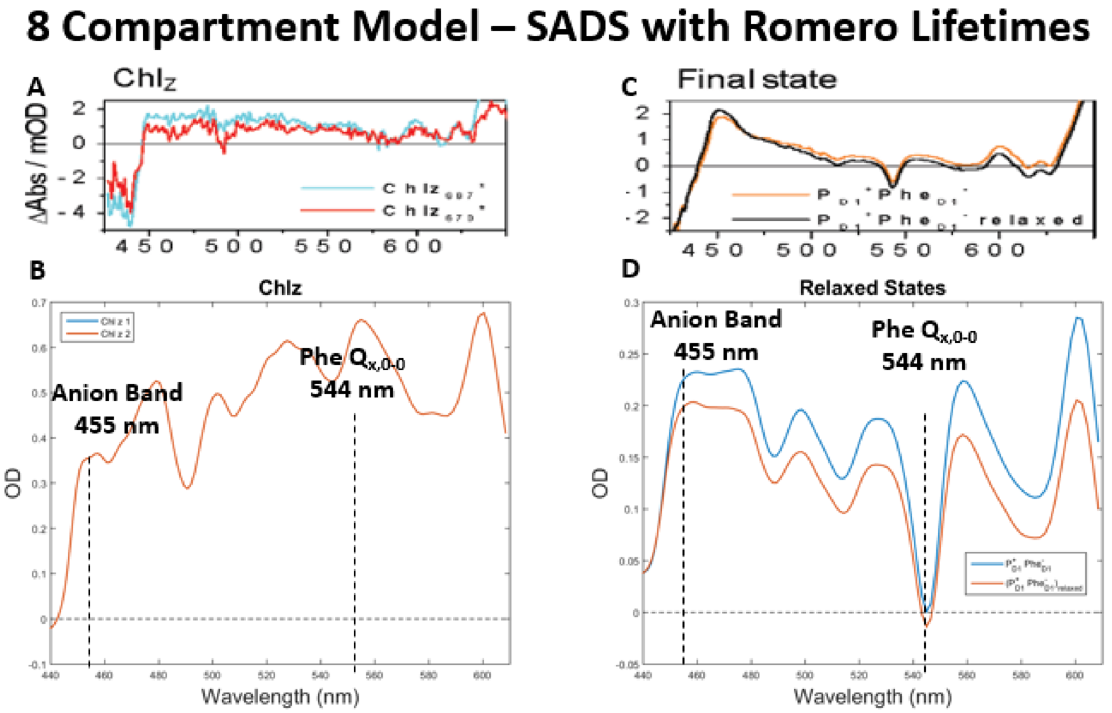

Figure 5.13: **8 Compartment Model** - comparing the SADS spectra for the Chlz's and the final charge separated states reported by Romero et al. [4] (panels A and C) and the SADS spectra obtained in this study (panels B and D) applying the Romero lifetime values from Table (5.4). Note that the SADS in panel B show the Chlz spectra to be exactly overlapped.

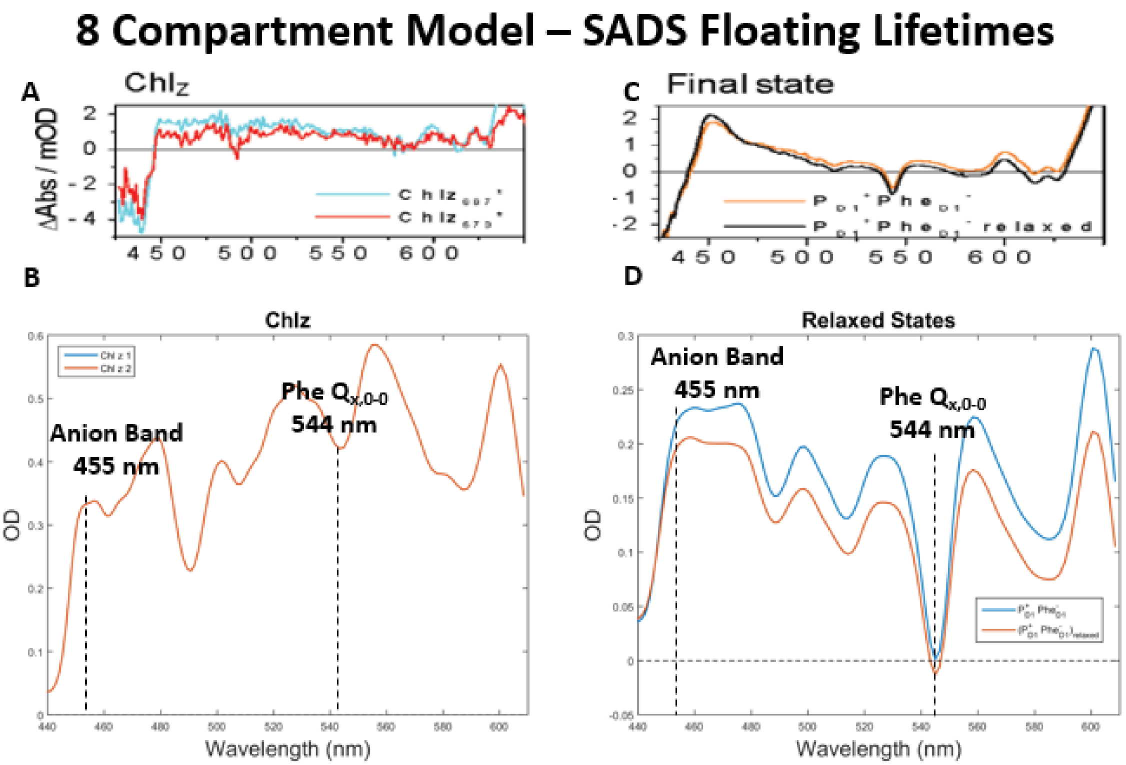

Figure 5.14: **8 Compartment Model** - SADS spectra for the Chlz's and the final charge separated states obtained using Carpetview after allowing the lifetimes to float (panels B and D) compared with the SADS obtained by Romero et al. (panels A and C). Recovered lifetime values are listed in Table (5.4). Note that the SADS in panel B show the Chlz spectra to be exactly overlapped.

Agreement does not improve when we consider the 1D SADS from the initial Chlz's and the final relaxed states using both the Romero lifetimes (Figure (5.13)) and allowing the lifetimes to float (Figure (5.14)). In fact, the results of both SADS for both lifetime values are identical. It is challenging to draw any conclusions about agreement between the Chlz spectrum reported by Romero et al. and the one obtained in our study, as the Romero spectrum does not have any defining features in this region. SADS for the final relaxed states (D panels in Figures (5.13) and (5.14)) show the expected strong Phe Q_x bleach and anion band contribution, but also additional positive amplitude at 475 nm, and bleaches at 489 nm and 512 nm. Incidentally, 475 nm corresponds to the Car D2 0-1 transition [124], 489 nm to the Car D1 0-0 transition [125], and 512 nm to the Phe Q_x 0-1 transition [125]. A later study, also by Romero et al., found that the features that appear at 475 nm and 489 nm can be explained by a change in the local carotenoid environment that induces a local Stark shift [126]. The authors go on to further suggest that this could perhaps be an indication that the carotenoids could play a role in assisting energy transfer. This claim has yet to be vigorously tested, but could perhaps provide some incentive for including carotenoids when modeling the energy transfer process.

In an attempt to seek better agreement with the expected spectral characteristics that would fit the physical description of the two-pathway model, a 6 compartment model was applied to our data. In this 6 compartment model states representing the Chlz contributions are removed, as shown in the kinetic scheme of Figure (5.15). This model begins with the parallel Chl D1 and PD1 pathways that both contribute to a final sequential pathway. Figure (5.17) shows the SADS obtained in the 6 compartment model in which the lifetime values are allowed to float. The Chl D1 pathway seems to show a strong broadband bleach across the 520-600 nm region, which is not consistent with the known linear absorption structure. This suggests that the lifetime values obtained by allowing the parameters to float does not improve the model. However, we do see significant improvement in the agreement of the expected physical features in the SADS when the 6-compartment model is fit using the Romero lifetimes (Figure (5.16)). Panels B and D of Figure (5.16) show the SADS for the Chl D1 and PD1 pathways obtained when applying the Romero lifetimes, where the Chl D1 SADS have increased contributions from the Phe Q_x bleach and anion band, and the PD1 SADS do not have exhibit any Phe contributions. We believe this isolation of Phe signatures between the two pathways is a key indication that our results support the two-pathway model. It must be emphasized that this agreement arises when using the lifetimes reported in the Romero study only when using the 6-compartment model.

There are other spectral features worth noting in the 6-compartment model. First, the Chl D1 path shows the Phe Q_x 0-1 bleach feature that becomes stronger in the second species. This emphasizes the isolation of the Phe features in the Chl D1 path. Second, negative features corresponding to Car D1 (489 nm) and Car D2 0-1 (475 nm) transitions that were found in the later Romero study [126] are also present, and notably strongest in the PD1 pathway. This suggests that if the carotenoids do play a role in ultrafast energy transfer processes, it is possible that they do so only on the PD1 pathway.

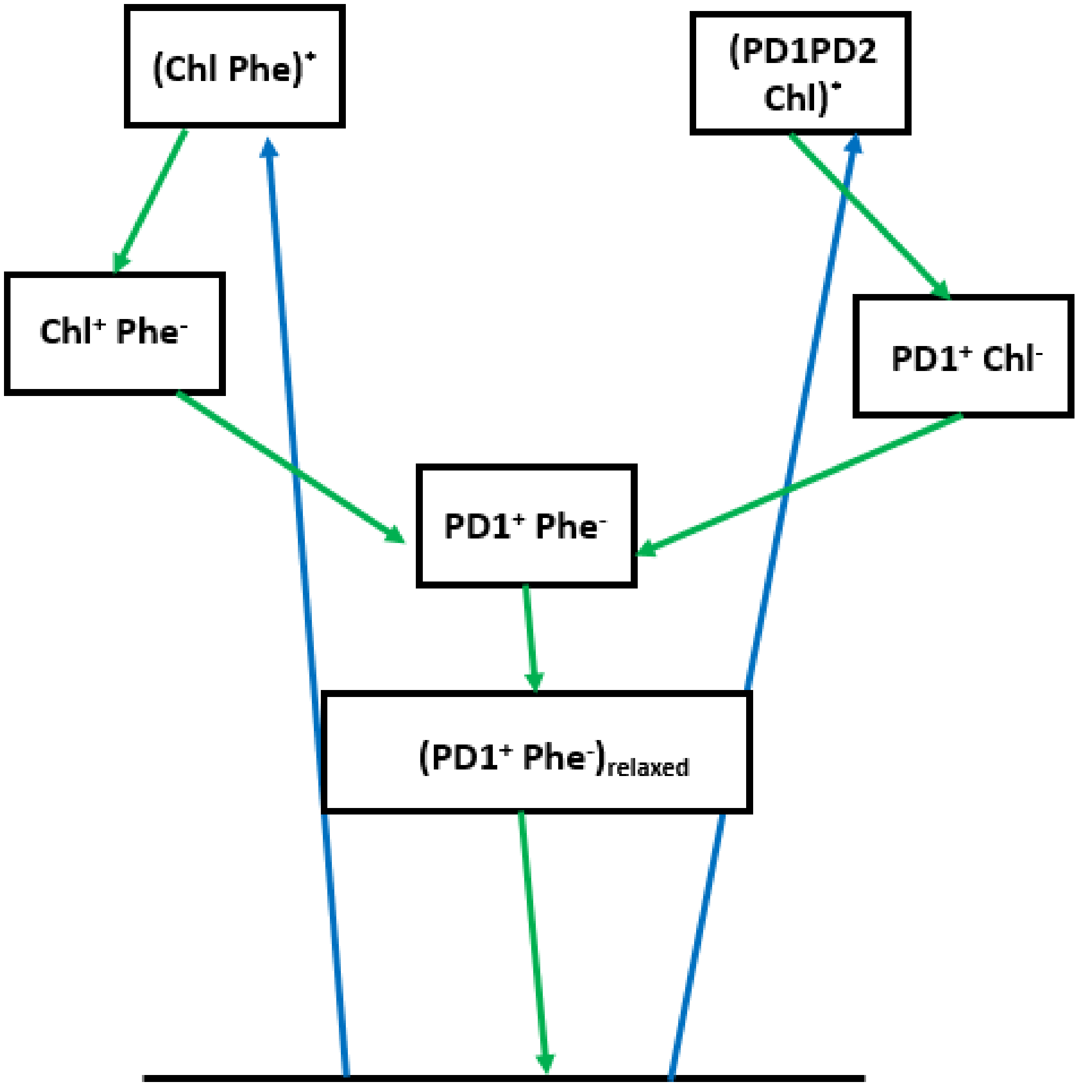

Figure 5.15: **6 Compartment Model** - a modification of the 8 compartment Romero model in which the two initial Chlz states are removed.

6 Compartment Model Lifetimes						
	τ_{02}	τ_{13}	τ_{24}	τ_{34}	τ_{45}	τ_{55}
Romero Lifetimes	3 ps	1 ps	58 ps	37 ps	500 ps	17 ns
Float Lifetimes	4.6 ps	0.2 ps	74.2 ps	48 ps	138 ps	90 ns

Table 5.5: **6 Compartment Model** - lifetimes reported by Romero et al. [4] and lifetimes found by the Carpetview software after performing a global analysis on the broadband probe 2D data.

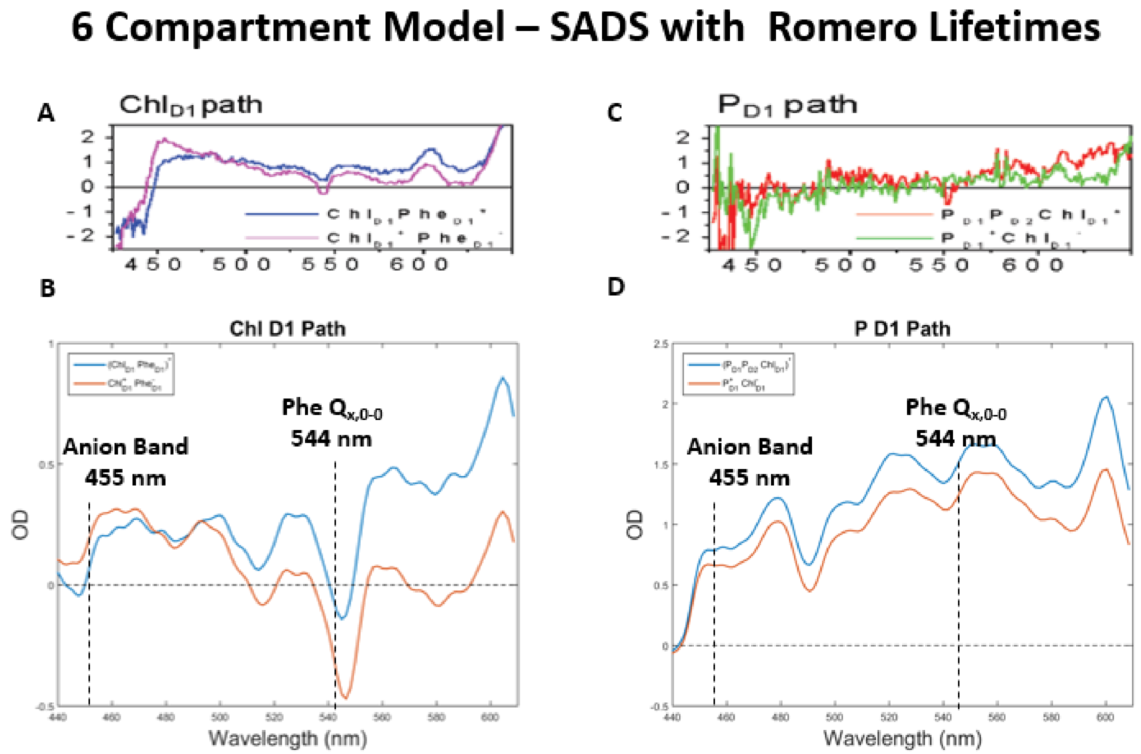

Figure 5.16: **6 Compartment Model** - comparing the SADS spectra for the Chl D1 and PD1 pathways reported by Romero et al. [4] (panels A and C) and the SADS spectra obtained in this study (panels B and D) applying the Romero lifetime values from Table (5.5).

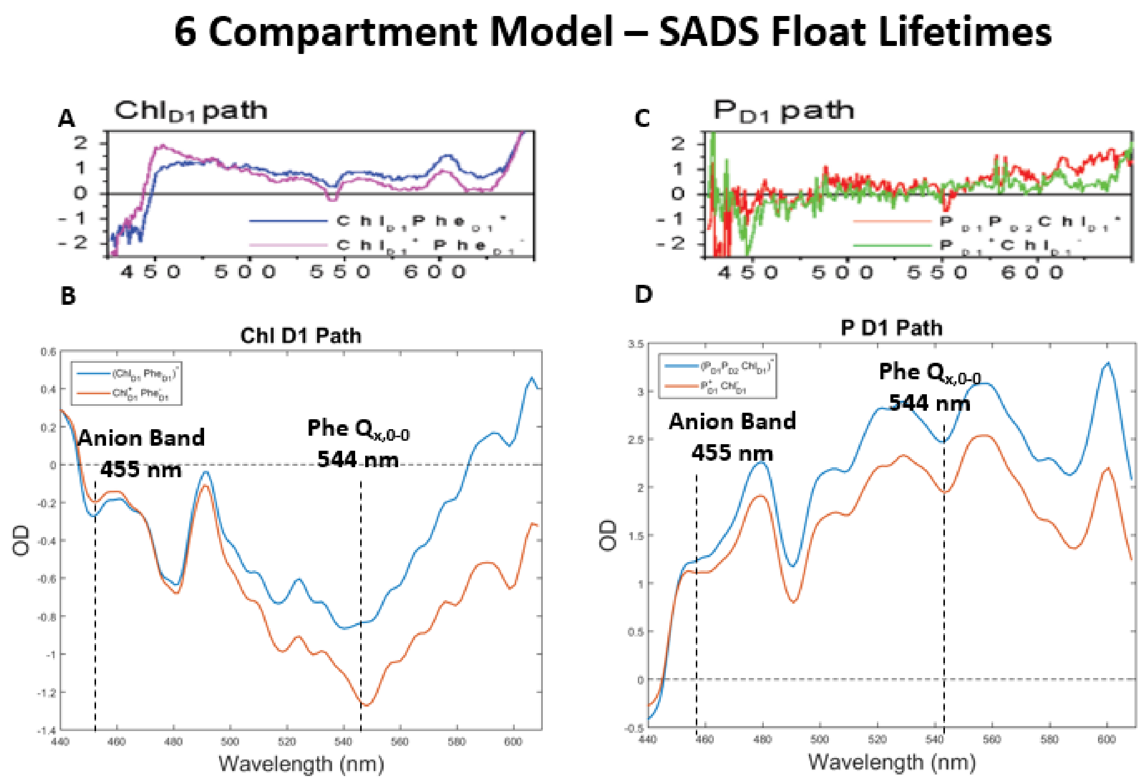

Figure 5.17: **6 Compartment Model** - SADS spectra for the Chl D1 and PD1 pathways obtained using Carpetview after allowing the lifetimes to float (panels B and D) compared with the SADS obtained by Romero et al. (panels A and C). Recovered lifetime values are listed in Table (5.5).

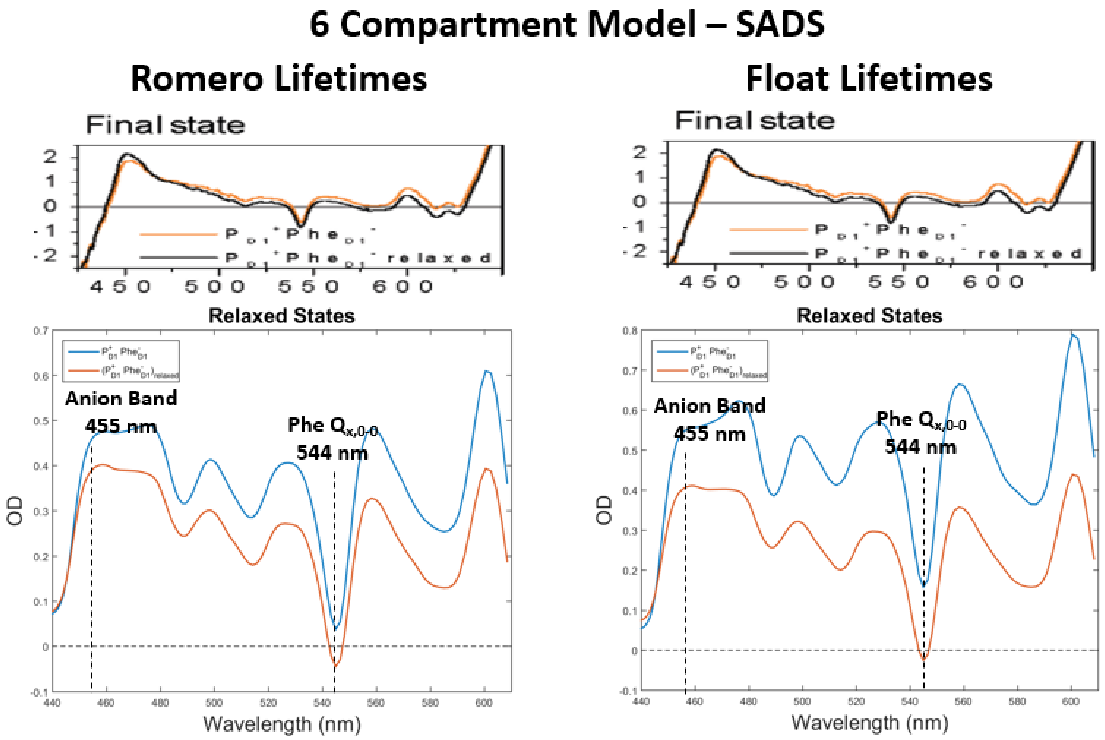

Figure 5.18: **6 Compartment Model** - comparing the SADS spectra for the the final charge separated states reported by Romero et al. [4] (left) and the SADS spectra obtained in this study (right) floating the lifetime values from Table (5.5).

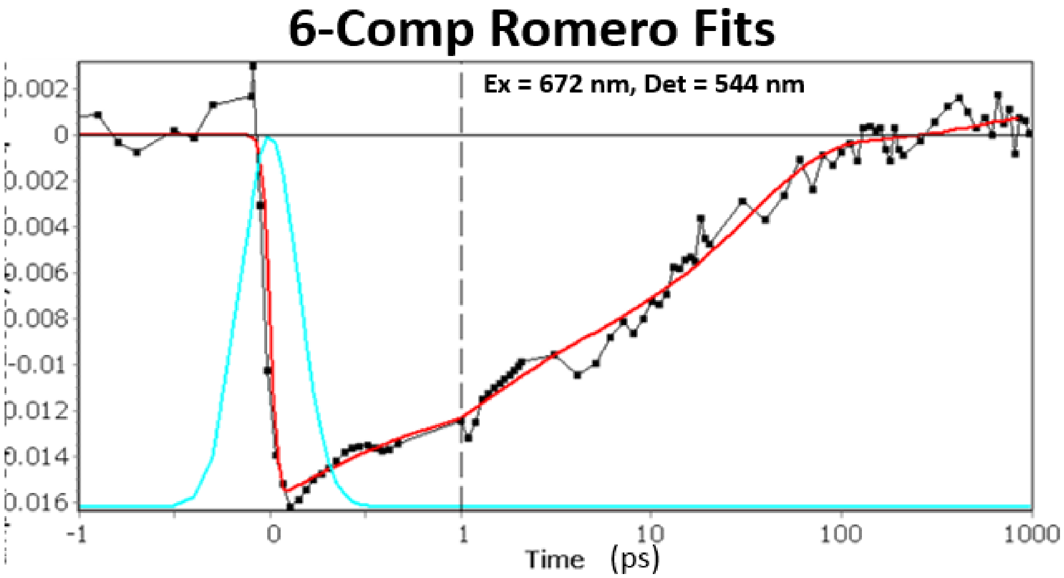

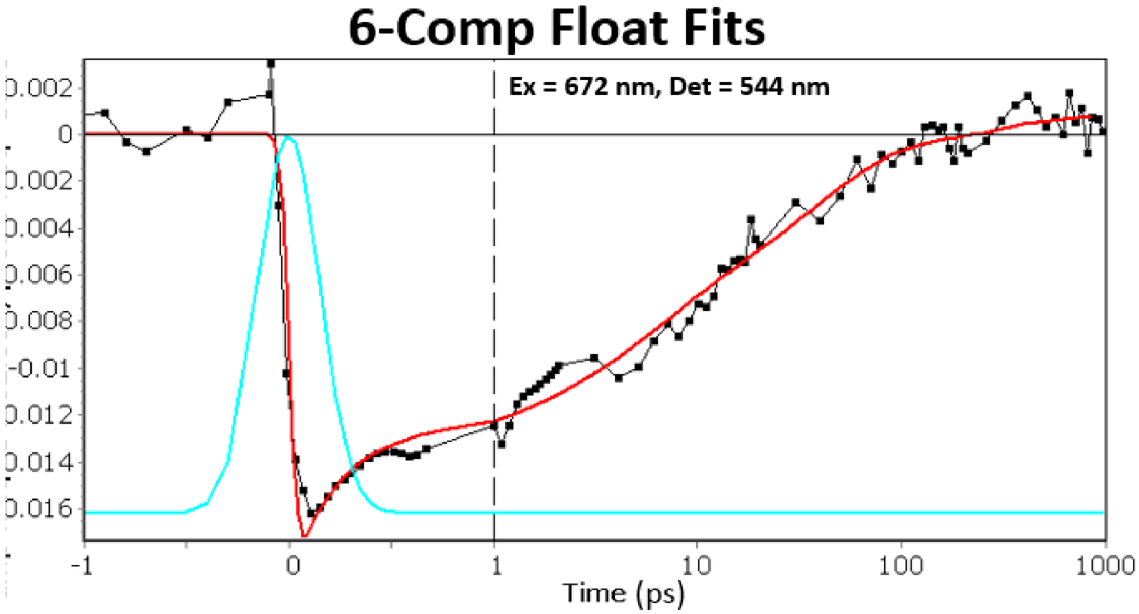

Figure 5.19: Comparison of fits to 2D time traces at excitation = 672 nm and detection = 544 nm (corresponding to exciting at Q_y and detecting at the Phe Q_x 0-0 transition) through t_2 using the Romero lifetime values and the floated values for the 6 compartment model. Black dots are the data, red lines are the fit, and cyan curves around time zero indicate the region exclude from the fit to remove contributions from the instrument response function.

5.7 Understanding the 6-Compartment Model

An explanation for the Romero model requiring the Chlz's in their model lies in their selective excitation of Q_y. The study uses data from consecutive experiments with the pump spectrum finely tuned to cover only a 5 nm bandwidth of Q_y to achieve an effective bandwidth covering 655-690 nm, when considering their experiments all together. However, the authors mention that they intentionally exclude their measurements in the 675-690 nm range when performing their global and target analysis. The authors also note that it is the blue region, or 655-675 nm bandwidth, they use in their analysis that specifically excites the Chlz's. Therefore, it could be said that the analysis of the Romero study favors contributions from Chlz, over contributions from the P680 exciton trap, which is established as the excitation required for initiating the PSII RC charge separation mechanism [20]. Our study, instead simultaneously excites all of Q_y, rather than favoring the blue edge.

We find further support for a 6-compartment model by considering the fits to the 2D data through time (Figure (5.19)). From these figures it can be seen that the 6-compartment model using the Romero lifetime values has the best fit (Figure (5.19), top panel), particularly at early times. This model also has the lowest χ^2 value of 5.08 x 10^{-7}, compared with 4.49 x 10^{-7} for the 8-compartment Romero lifetime model, 4.78 x 10^{-6} for the 8-compartment floated lifetime model, and 4.7 x 10^{-7} for the 6-compartment floated lifetime model.

At the same time, it must be mentioned that the data of our study is also incomplete. Due to the high sample concentrations used we could not include the Q_y region into our global analysis. Spectral features on the red or blue sides of this region inform Chl and Phe involvement of the different compartments. We anticipate future studies from our group will focus on providing an expanded view of the charge separation mechanism in the PSII RC, incorporating Q_x, Q_y, and mid-IR spectral regions.

While our data exhibits agreement with the two-pathway model of charge separation in the PSII RC when contributions from the Chlz's are not included in the kinetic model, we are not completely satisfied with its physical interpretation. The most troubling aspect of this model is the absence of definable spectral features in the PD1 SADS that point to distinct participation of the PD1, PD2, and Chl D1 pigments that are supposedly responsible for this path. In fact, the SADS published in the Romero study seem to be devoid of any defining spectral features. Since PD1, PD2, and Chl D1 pigments are all chlorophyll pigments, one might then expect to see features in the SADS around 512 nm, corresponding to the Chl Q_x 0-1 transition that would indicate an electrochromic shift from local charge separation. Since such a signature is not present, it is possible that the SADS of this pathway represents contributions from RC's that fail to undergo charge separation. This possibility is worth investigating in the future by using a kinetic model where the Chl D1 and PD1 pathways are entirely parallel and do not converge at the $\mathrm{Phe}^{-}\mathrm{PD1}^{+}$ state.

Another concerning aspect of the two-pathway model is the existence of the two final states that both the Chl D1 and PD1 pathways feed into. Both states are described as being composed of the final $\mathrm{Phe}^{-}\mathrm{PD1}^{+}$ charge separated state, but the justification for including the two distinct states is unclear. Romero et al. [4] aruge for including the second state because the SADS of the Q_y region and the visible region indicate an increase in the Phe population that occurs between these two states. This suggests there is an additional slow channel feeding into the charge separated state. However, this begs the question as to whether the final state is entirely necessary to uniquely perform the global analysis. The inclusion of this final state is worthy further investigation.

In summary, the data presented here offers support to the pre-existing two-pathway model when using a 6-compartment model. However, we call into question the physical interpretation of this model and suggest that further studies are needed to rule out other models.

5.8 Evaluating Charge Separation Pathways with 2D SADS

Until this point, my analysis has focused on the qualitative agreement of the 1D SADS obtained in this study with those reported in the Romero study. The nature of our 2DES data allows us to generate 2D SADS, which provides the additional excitation frequency dependence of the SADS spectra. A glance at the 2D SADS for the states in the Chl D1 and P D1 pathways in the 6 compartment model (Figures (5.20) and (5.21)) shows distinctive excitation dependence between the pathways of the two models. [Note: transient absorption measurements have a sign flip difference from 2D data. I have multiplied the 1D SADS from our study by -1 to directly compare with the Romero SADS. The 2D SADS have not been multiplied by -1. This means that the bleach features are positive in the 2D SADS.]

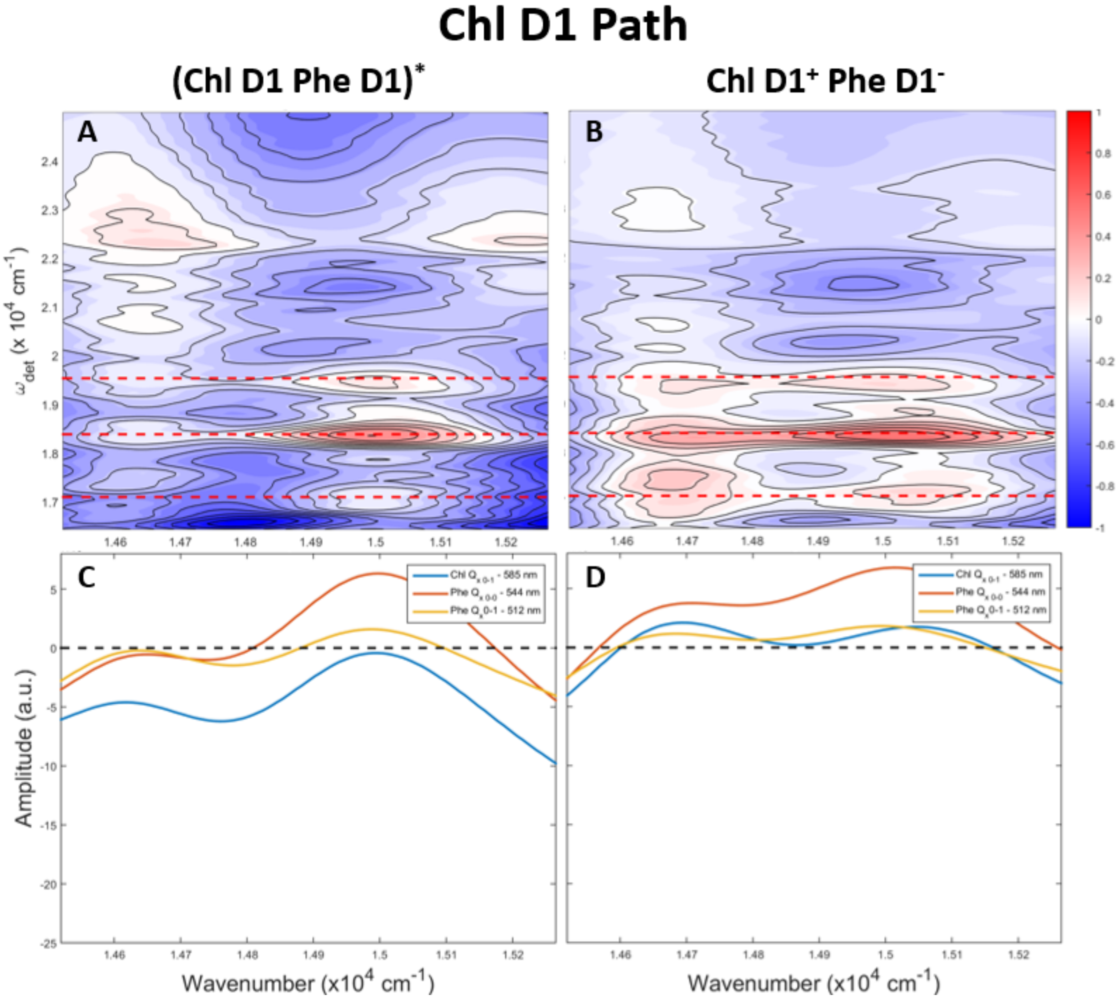

Figure 5.20: 2D SADS for the Chl D1 pathway (panels A and B) with excitation dependent slices (panels C and D). Dashed red lines in the 2D contour plots of A and B indicate the slices represented in C and D. These slices correspond to the Phe Q_x 0-1 transition at 19531 cm^{-1} (512 nm), Phe Q_x 0-0 at 18382 cm^{-1} (544 nm), and Chl Q_x 0-1 transition at 17094 cm^{-1} (585 nm).

Examining the Chl D1 path, Figure (5.20) exhibits bi-modal excitation dependence, similar to the excitation dependence of the Phe peak in the background subtracted 2D data (Figure (5.7)). However, there are two important differences between the 2D slices and the 2D SADS slices. The first is that the location of the peaks in the 2D SADS are red-shifted from those in the 2D spectra. In the 2D spectra the Phe peaks are at 14800 cm^{-1} (675 nm) and 15200 cm^{-1} (658 nm), while in the 2D SADS the peaks are at 14600 cm^{-1} (685 nm) and 15000 cm^{-1} (667 nm). The second difference is that the relative amplitudes of the peaks in the excitation dependent slices are flipped. In the case of the 2D spectra, it is the lower energy peak with greater amplitude, but in the 2D SADS it is the higher energy peak with greater amplitude. A reason for this could be that due to the fact that the SADS reflect contributions from the pigments directly participating in the charge separation pathway and therefore represent only a subset of the pigments in the RC. This could therefore lead to a different excitation dependent contribution configuration that favors the lower energy pigments and hence red-shifts the peaks.

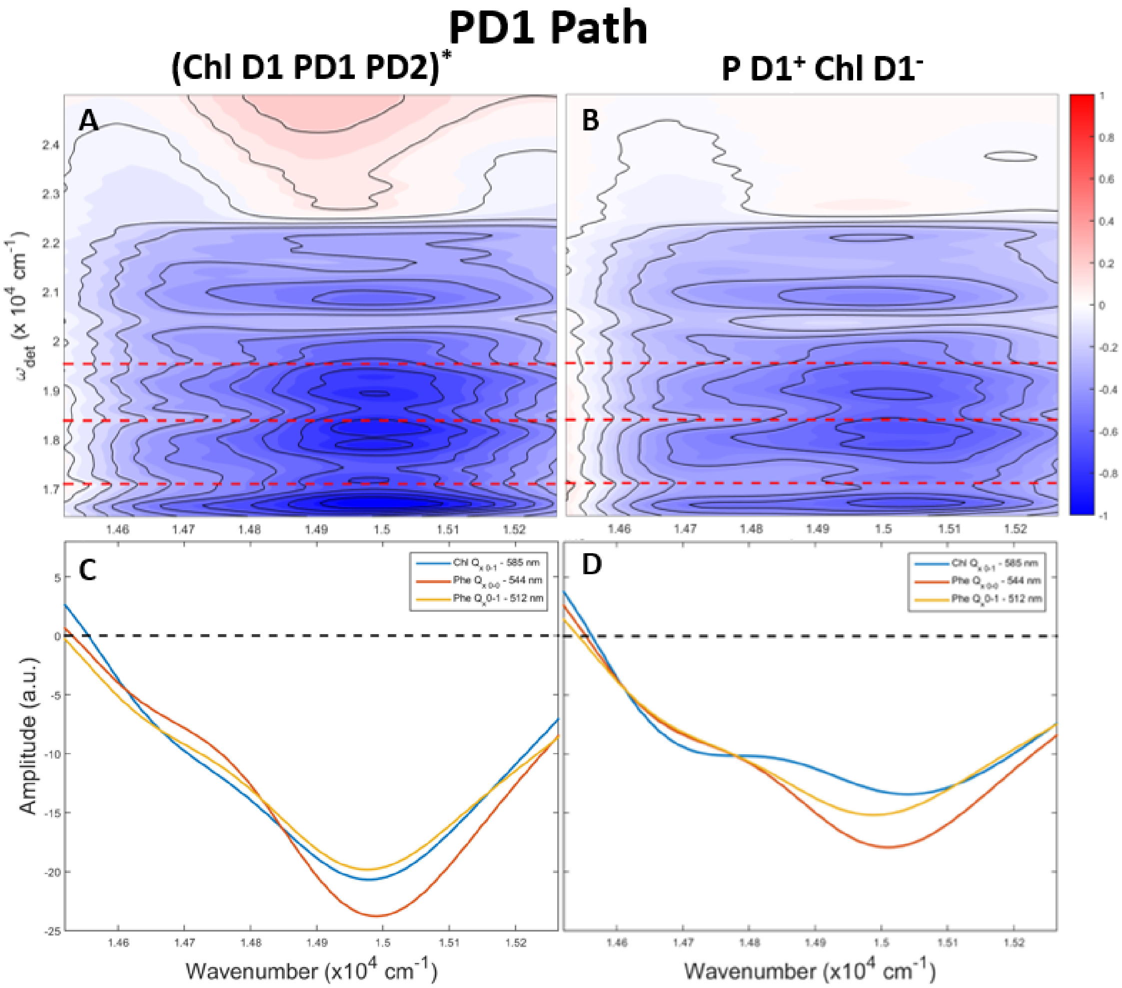

Figure 5.21: 2D SADS for the P D1 pathway (panels A and B) with excitation dependent slices (panels C and D). Dashed red lines in the 2D contour plots of A and B indicate the slices represented in C and D. These slices correspond to the Phe Q_x 0-1 transition at 19531 cm^{-1} (512 nm), Phe Q_x 0-0 at 18382 cm^{-1} (544 nm), and Chl Q_x 0-1 transition at 17094 cm^{-1} (585 nm).

For the PD1 path (Figure (5.21)), the excitation dependent slices of the 2D SADS shows a strong negative feature at 15000 cm^{-1} (667 nm) in the initially excited species (panel C). Consulting Table (2.2), this corresponds well with the PD1 and PD2 site-energies observed in the Renger and Gelzinis exciton models. This further agrees with the predicted participation of PD1 and PD2 from the initial delocalized excitation in the PD1 pathway. The charge separated species then shows a peak at 14700 cm^{-1} (680 nm) (panel D), which is close to the Chl D1 site-energy, while the 15000 cm^{-1}

peak loses some amplitude. This is in good agreement with the model's prediction of the formation of the $PD1^+ChlD1^-$ charge separated state where contribution from Chl D1 becomes stronger, but PD2 no longer participates and the 15000 cm^{-1} peak loses amplitude. As was presented earlier in the chapter, the 1D SADS provided very little spectral evidence for the pigments participating in the PD1 path. However, using the 2D SADS we are able to obtain clear spectral markers for a given species in support of the two-pathway model.

5.9 Conclusions

From the data presented on the exciton models compared with excitation dependent slices of Phe and Chl, no single model seems to stand out as best representing the data. It does appear that all the models exhibit, to some degree, a split in the exciton compositions such that excitons with a >25% Phe contribution fall to the lower energy region, while those will <25% Phe contribution fall to the higher energy region. The Gelzinis model has excitons that fall between the Phe and Chl peaks with <25% Phe contribution, but the contribution does not fall below 20%, making these excitons of a more mixed Chl/Phe character. Overall, the Gelzinis model shows interesting clustering of the exciton transition energies around the Phe and Chl peaks. This, in consideration with the exciton compositions, agrees best with our data. The Renger model also shows clustering around the Phe peak, but deviates from our data in that a cluster fails to form around the Chl peak. The van Grondelle model shows large separation between the excitons, which may change with the inclusion of reorganization energy values, and no obvious clustering. For this reason, the van Grondelle model does not appear to fit well with our data.

Regarding analysis of the PSII RC kinetic model, the results of this study are in general support of the two-pathway model of charge separation in the PSII RC. We suggest a slight modification to the 8-compartment two-pathways model of Romero et al. [4]. We find the best spectral agreement of the SADS for the Chl D1 and PD1 pathways suggested in the Romero study when excluding the two Chlz compartments to form a 6-compartment model. Floating the lifetimes does not improve spectral agreement, suggesting that the lifetimes reported in the Romero study are accurate. In addition to this, we resolve features associated with a Stark shift experienced by the Car D2 0-1 and Car D1 0-0 transitions, as well as a bleach signal from the Phe Q_x transition. Identifying the function played by these additional features requires further study, but these results add support for including them in future modeling work.

CHAPTER 6

Conclusions and Future Work

This thesis seeks to resolve ambiguities in charge separation and energy transfer processes in oxygenic photosynthesis. It examines photosynthetic pigments on two length scales: the single pigment and PSII RC unit. Below I describe the conclusions reached in both studies and the vision for further studies.

6.1 Chl a and Bchl a Study

Chapter 4 presents 2DES studies implementing polarization control between the pump and probe beams to resolve cross peak specific 2D spectra. This experimental method was applied to the Q_x and Q_y regions of penta-coordinated Chl a and Bchl a pigments to contribute to the long existing debates about the underlying electronic structure of the Q-band transitions of Chl a (exhibiting three peaks at 587, 620, and 667 nm) versus Bchl a (exhibiting two well separated peaks at 578 and 770 nm) [73]. Despite these spectral differences in the Q-band, both pigments have predominantly been described by the Gouterman model, which holds that the Q-band is composed of two perpendicularly polarized electronic transitions in the chlorin plane.

Analysis of the cross peak specific spectra find the transition dipole moment angle of Bchl a to be nearly constant at 75°. In contrast, Chl a exhibits considerably more complex wavelength dependent behavior of the relative transition dipole orientation of Q_y and Q_x (Figure (4.5)). Ab initio TD-DFT calculations on Chl a show this excitation wavelength dependence as arising from strong overlap between two electronic transitions S_1 and S_2 and their higher vibrational modes. This suggests that the 578 nm and 620 nm peaks of Chl a are of mixed Q_x and Q_y character, while they remain two well separated electronic transitions in Bchl a. Further support for this model is provided by our internal conversion calculations, which show the rates to be much faster for Chl a than Bchl a (Figure (4.6)). The faster internal conversion in Chl a may arise from a combination of the smaller Q_x-Q_y energy gap, as well as vibronic mixing between Q_x and Q_y transitions. Figure (4.7) shows our proposed energy state model with internal conversion for Bchl a and Chl a.

The polarization scheme for the P-2DES measurements of this study are only a small taste of the kinds of signals that can be extracted utilizing polarization control. Measurements here required performing two separate scans in the parallel and cross polarized schemes. Full polarization control over all the pulses in the 2DES experiments, which is difficult to accomplish in our current setup, is desirable since it would enable higher signal-to-noise measurements [75]. Moreover, it also allows for the collection of a coherence-specific spectrum. The interpretation of coherent signals in 2DES experiments and their role in photosynthetic energy transfer has been a hotly debated topic over the past decade [38, 127–132]. Implementing a double-cross polarization capability into our setup would allow us to more easily assign the physical origin of the various signals to vibrational, electronic, or vibronic coherence. Nearly a year of my graduate student work was spent on building such a setup. So far, only very preliminary results have been obtained and therefore have not found their way into this thesis. However, we expect this to be a central focus in the lab's future work.

6.2 Broadband 2DES Study on PSII RC

Chapter 5 presents broadband, two-color 2DES data taken on the PSII RC, resolving Q_x and carotenoid transitions, adding to the limited spectroscopic data available in these regions. The study used the ability of 2DES measurements to resolve the excitation dependence of the 2DES signal at the detection frequency of the Chl $Q_{x,01}$ and Phe $Q_{x,0-0}$ transitions. This enabled us to compare our data with the trends expected based on the pigment composition of the Gelzinis, Renger, and van Grondelle exciton models presented in Chapter 2. Based on the exciton compositions (detailed in Figures (5.7)-(5.9)) and the spectral locations of the exciton transitions for each model, the Gelzinis model seems most consistent with the data presented in this thesis. However, it is only fair to admit that van Grondelle model may not have been adequately evaluated because of the limited published information available on crucial elements to the model, like the appropriate reorganization energy and pigment couplings. In future work, we would like to use the data presented in this thesis to fit to the van Grondelle excitons to recover the reorganization energies used.

We also performed a global analysis of the two-color 2DES data on the PSII RC to test the two-pathway model of Romero et al. [4]. Our study finds overall agreement with the two-pathway charge separation mechanism, but finds that a 6 compartment model, instead of their proposed 8 compartment model (Figures (5.11)-(5.17)). This 6 compartment model excludes contributions from the auxiliary Chlz pigments. We believe the primary reason for the differences in the studies arise from the different excitation conditions used in the experiments. Our 2DES experiments employ pump pulses that space the Q_y region, while because the transient absorption measurements used in the Romero study selectively excite the blue region of the PSII RC Q_y peak, which favors Chlz excitation. Their data is therefore contains increased Chlz contribution, which likely over-emphasize the importance of Chlz in the model. We hope to further refine our understanding of the two-pathway model by incorporating data from Q_x, Q_y, and mid-IR vibrational regions in future studies. This large multi-spectral dataset would contain additional spectroscopic signatures of charge separation that would help futher refine the charge separation mechanism. In fact, the experimental implementation of this work is already well underway utilizing the multi-spectral 2DES capabilities of the LUMOS lab at the University of Michigan.

Results of our species associated difference spectra (SADS) show contributions from features that have not been well represented in previous models. In particular, we see strong contribution in the region of the Car D1 0-0 transition in the final relaxed state. Evidence of this transition in PSII RC related studies has been weakly observed [126,133] in previous studies and is believed to be due to a local Stark effect.

We also resolve similar contributions from the Phe Q_x 0-1 transition in the longer lived species, not observed in the Romero model. We hope that we may gain more insight into these features, and possible contributions from exciton models through further analysis of our 2D SADS data as well as multi-spectral 2DES experiments.

Advancing our understanding of the structure-function relationship of the PSII RC requires better experimental and theoretical methods for identifying charge transfer states. Recent work by our group in developing 2D electronic Stark spectroscopy (2DESS) [6, 39] provides a way forward that may enable the identification of specific charge transfer states involved in the two-pathway mechanism. Further quantum chemical calculations, like those implemented with the Chl a/Bchl a monomer study, are needed that extend beyond a single pigment to describe the coupled PSII RC pigment system, capturing the effect of the surrounding protein environment.

APPENDIX A

PSII Sample Preparation Procedure

This procedure serves as a more detailed supplement to the procedure detailed in Appendix A of Anton Loukianov's thesis, which is based off the work in references [22, 23, 113]. It is included in this thesis in the interest of posterity and includes equipment and language particular to our lab at the time of writing that may not be universally relevant. It deviates from Anton's procedure after the Core prep B-β wash. At this step, this procedure elutes the Core samples off the column and preforms the Triton-X incubation (to break off antennae complexes and retrieve the D1-D2-Cyt b559 Reaction Center (RC) complexes). The sample is then loaded onto a smaller volume column and washed to extract the RC complexes. The entire process, starting from spinach and ending with Reaction Center complexes concentrated to experimental conditions, takes about four days of work.

A.1 BBY Particle Procedure

Notes Before Starting: This part of the procedure starts with store-bought spinach and ends with BBY particles prepared for long term storage in a -80 °C freezer. When working alone the whole process takes approximately 11 hours. Procedure time is reduced to about 8 hours when working in a pair.

Initial Preparations

The Day Before:

- Prepare appropriate buffers from stock solutions.
- Purchase approximately 40 oz of organic, locally sourced mature spinach. I use seven 6 oz packages of spinach purchased at Busch's Market.
- Prepare access to a liquid nitrogen source.

The Day of:

- Start 25 g Triton-X + BBY-3 solution spinning. Let solution spin until smooth and white with bubbles (can take up to 1 hr). Put on ice until used in procedure.
- Add bovine serum albumin (BSA) to BBY-1 and BBY-2. Shake gently a few times to homogenize and store in fridge until used.
- Turn on large centrifuge to cool down.
- Fill a large cooler with ice.
- Prepare 2L Erlenmeyer flask on ice with large funnel and cheesecloth.
- De-stem all spinach and collected a bucket. Takes ∼1.5-2.0 hrs when working alone, ∼1 hr when working in a pair.

Procedure:

1. Add roughly half a blender volume of spinach and add a splash of BBY-1 buffer. Chop to make rough slurry and then add more spinach. Add spinach and chop several times until blender filled to approximately 3/4 volume. Blend for ∼20 seconds to make a final smooth mixture and strain through cheesecloth into E. flask. Repeat until all spinach is chopped.
    (a) Not always necessary to use all BBY-1 buffer.
    (b) Squeeze solution through cheesecloth to increase yield (spending extra time to get as much juice out as possible here can help significantly increase the final sample concentration). Be careful not to burst cheesecloth.

2. Divide sample equally among six 250 mL centrifuge bottles. Spin for 10 min at 6,000 xg. **Work under green light after spinning and for all the remaining procedures that follow.**
    (a) Discarded supernatant and re-suspended with 30 mL BBY-2. Optimize BBY-2 usage to extract as much of the pellet as possible.
    (b) Side Note: Spending extra time at each re-suspension step to ensure the centrifuge tubes are as clean as possible results in a higher final sample yield.
3. Homogenized in 50 mL tube.
4. Divide homogenized solution between eight 40 mL centrifuge tubes. Spin for 10 min at 12,000 xg.
    (a) Discard supernatant and re-suspend with < 40 mL BBY-3.
    (b) Measure final volume of the sample.
5. Prepare three 1.5 mL centrifuge tubes to measure the sample spectrum. In each centrifuge tube, add 3 μL to 1.5 mL 80% acetone. Vortex and then spin samples in table-top centrifuge for 3 min at 1,300 g.
    (a) Measure spectra in 1 cm cuvette (compare against Figure (A.1)). Add measured absorption values from the spectra to the Triton Solubilization (Step 1, Option A) page in the RC Sample Log Google Sheet to determine the chlorophyll concentrations.
    (b) Identify the spectrum measurement that yielded the median value in the Chl Concentration column between the three measurements. Apply the previously measured total volume, and Chl Concentration from Step 1 to the appropriate cells in Step 2.
    (c) Note the resulting amount of BBY-3, BBY-3T and Final Volume determined in Step 2.

   (d) Record the results of Step 1 on the Prep Log BBY page.

6. Add the necessary amount of BBY-3 buffer to the previously homogenized sample. Pour the sample into a 250 mL E. flask on ice with a stir bar. Measure out the necessary amount of BBY-3T. Be sure to measure from the meniscus below the line of bubbles (may need to let bubbles settle for a few minutes). With the stir bar spinning, slowly and steadily add BBY-3T drop-wise with a pipette ensuring not to create a stream (the process works best when two people add BBY-3T together). Incubate for a total of 28 minutes, beginning the timer as soon as the first drop hits the sample. Distribute sample among four 40 mL centrifuge tubes and spin for 30 min at 48,000 xg.

   (a) Side Note: I generally add all the BBY-3T, leave stirring on ice for 25 min, then distribute between four 40 mL centrifuge tubes and start spinning in centrifuge as soon as the 28 min timer goes off. Essentially, time is of the essence. It is key that the sample not be left incubating longer than 28 min.

7. Discard supernatant and re-suspended in 25 mL A buffer. Homogenize in 30 mL homogenizer tube.

8. Distribute homogenized sample between four 40 mL centrifuge tubes and spine again for 5 min at 2,000 xg.

9. **Retain supernatant** by pouring directly into four clean centrifuge tubes. Spin for 30 min at 48,000 xg.

10. Discard supernatant and re-suspend in 20 mL of A buffer. Measure the final volume and measure out three 1.5 mL centrifuge tubes for sample spectra as before.

11. Measure absorption spectra in 1 cm cuvette and apply absorption values to Step 3 of the Triton Solubilization page (compare spectra against Figure (A.2), Figure (A.3) shows the spectral differences between BBY Step 1 and BBY

Step 2). Determine measurement that yields the median Chl concentration value. Record the results in the Prep Log BBY page and measure the final concentration as follows: $V_f = 1/3(\text{Chl Concentration})(V_{sample})$.

12. Dilute homogenized sample to the final volume with A buffer.

13. Prepare a Styrofoam container with liquid nitrogen and a cheesecloth. Add diluted sample dropwise with a pipette into liquid nitrogen to form frozen balls of sample.

14. Remove cheesecloth and quickly add sample to 15 mL Falcon tubes. Store in -80 °C freezer as soon as possible. Once in the frozen state the sample is stable and can be left indefinitely until one is ready for the Core prep.

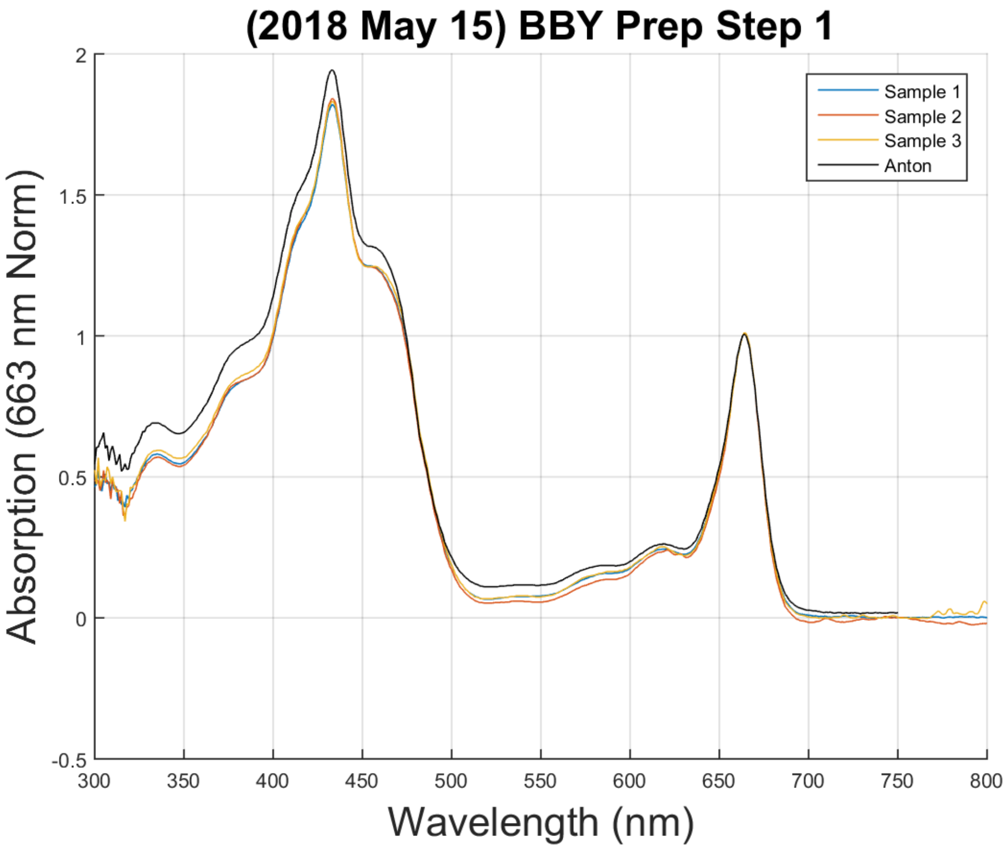

Figure A.1: Linear absorption spectrum of BBY-step1. The measurements are compared against those obtained by Anton, a previous lab member.

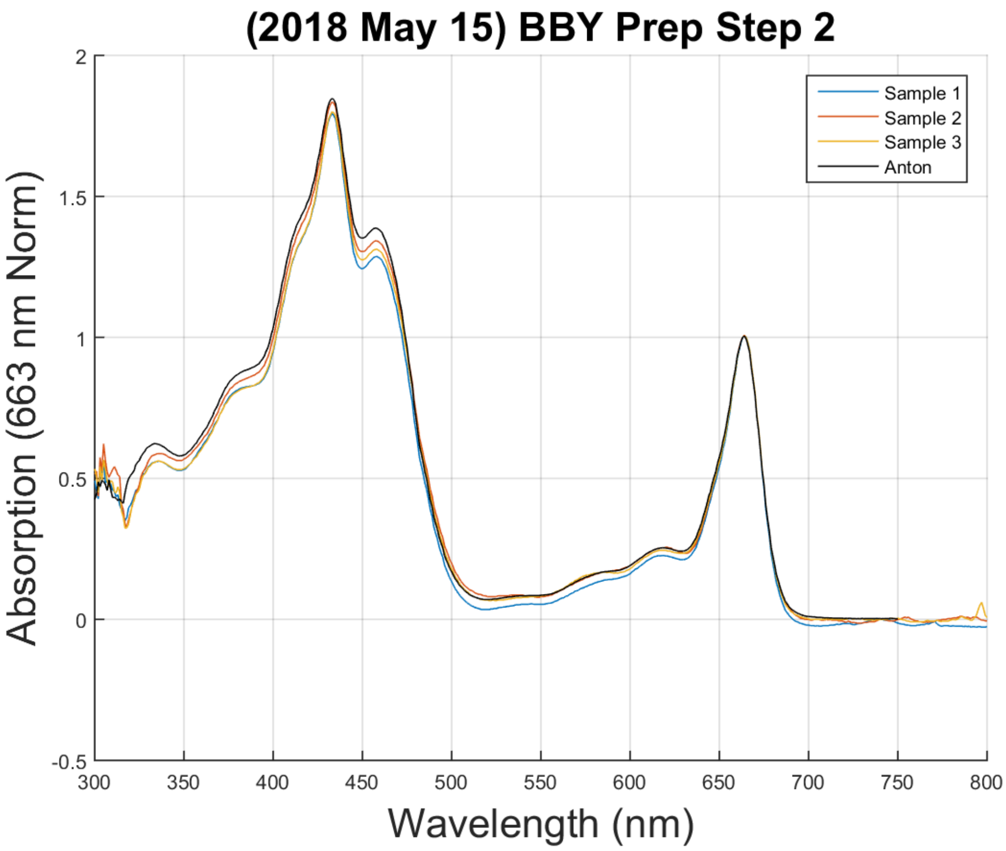

Figure A.2: Linear absorption spectrum of BBY-step 2.

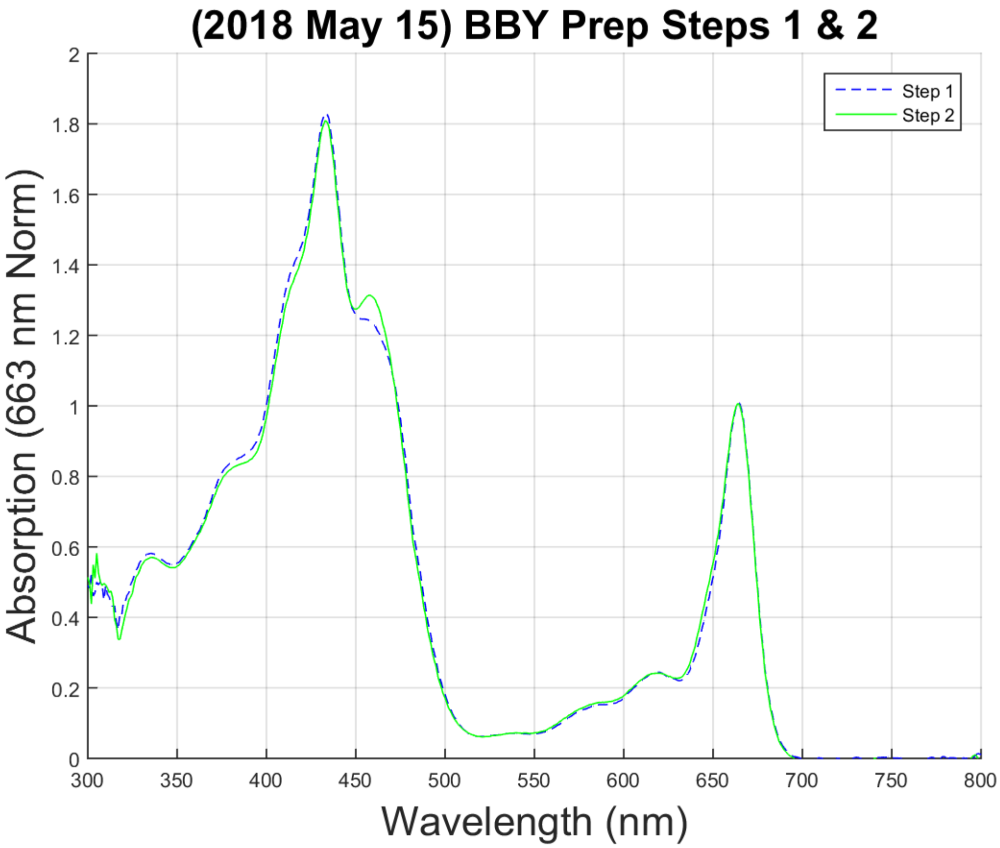

Figure A.3: Comparison of linear absorption spectra of step 1 and step 2 of the BBY preparation.

A.2 Cores Isolation Procedure

Notes Before Starting: This part of the procedure starts with thawing two 15 mL Falcon tubes of the final yield of the BBY prep, incubates the BBY particles with an X treatment, and washes the sample so that only Core complexes (i.e., CP47 + CP49 + D1D2) remain. It is generally good practice to perform this Core Prep and the Reaction Center prep on consecutive days to prevent sample degradation.

Initial Preparations

The Day Before:

- Pack the large anion exchange column. Leave both the intake and waste lines submerged in DI water to prevent bubbles from entering the system. Also ensure that the plunger gasket is tight.

- Prepare A and B buffers.
- Ensure appropriate amounts of β-DM are aliquoted to make A-β, B-β, C2-β and 3 mL of X buffers.

The Day Of:

- Acquire ice.
- Prepare A-β (830-1000 mL), B-β (500 mL), and C2-β (200 mL) buffers.
- Turn on large centrifuge to cool down.
- Move column and pump system to refrigerator so the loading a wash processes stay cool.

Procedure:

1. Thaw two 15 mL Falcon tubes of BBY balls and make note of the total volume. Calculate the amount of X needed by dividing the total volume by 5.
2. Dilute each Falcon tube of thawed sample to 15 mL with A-β. (To extract as much sample as possible, I generally fill each Falcon tube to the 13 mL mark with A-β, then rinse with 2 mL A-β and used 1 mL pipetter to gather final thawed sample collected at bottom of Falcon tubes.)
3. Transfer diluted sample to 50 mL homogenizer and homogenize.
4. Split volume between two 40 mL centrifuge tubes.
5. Spin 3,000 xg for 3 min.
6. Transfer supernatant to new 40 mL centrifuge tubes and dilute each to about 40 mL with A-β.
7. Spin at 48,000 xg for 30 min.

   1. Prepare necessary amount of X solution while spinning. (It can take 30-60 min for β-DM to completely dissolve. Periodically vortexing can help speed up the process.)
   2. Start equilibrating the column with A-β. Usually set for 45-50 minutes at a moderate speed, which displaces about 300 mL).
   3. Discard supernatant.

8. Re-suspend sample with the original sample volume of A-β + 4 mL extra of A-β to have sample at the proper concentration for incubation. I generally use the extra 4 mL to wash centrifuge tubes well and extract any sample that might not have poured out.

9. Homogenized in 30 mL homogenizer.

10. Incubate with calculated amount of X at room temperature for 25 min. Add X in the same quick, steady, drop-wise fashion as the BBY-3T in the previous procedure, also beginning the timer as the first drop hits the sample.

    (a) Here, as in the BBY prep incubation, time is of the essence. With 3 min left in incubation time I load the sample into 10 mL centrifuge tubes and begin the next spin as soon as the 25 min timer goes off.

11. Spin at 48,000 xg for 20 min.

12. Pour supernatant into 50 mL falcon tube ($\sim$15 mL) and dilute to 50 mL with A-β.

13. Load diluted sample onto equilibrated column. Once the 50 mL Falcon tube has approximately 2 mL left, diluted to 50 mL again with A-β and continue loading. Total loading time for both dilutions should be around 20 min.

14. Wash with A-β for 55 min.

15. Wash with B-β for 55 min.

16. Elute sample off the column using C2-β. Let the initial clear eluant collect as waste. Once the eluant becomes green, begin collecting in 15 mL Falcon tubes. Collect until the green stripe on column has disappeared and the eluant is clear (usually collect about six 15 mL Falcon tubes of core sample).

17. Measure spectrum in 1 cm cuvette (using C2-β for the background measurement) at a 200x dilution (1 mL C2-β, 5 μL sample). Compare results to Figure (A.4).

18. Concentrate by spinning in four 15 mL filter tubes (look like 50 mL Falcon tubes) at 5,000 xg for 40 min. If there is excess sample that does not fit in the filter tubes, add remaining sample after 40 min and let spin for another 40 min. Final concentration should be less than 1 mL in each filter tube.

19. Gather all concentrated sample in one 15 mL Falcon tube. Dilute to 4 mL with C2-β.

20. Store in a light-tight container with ice overnight.

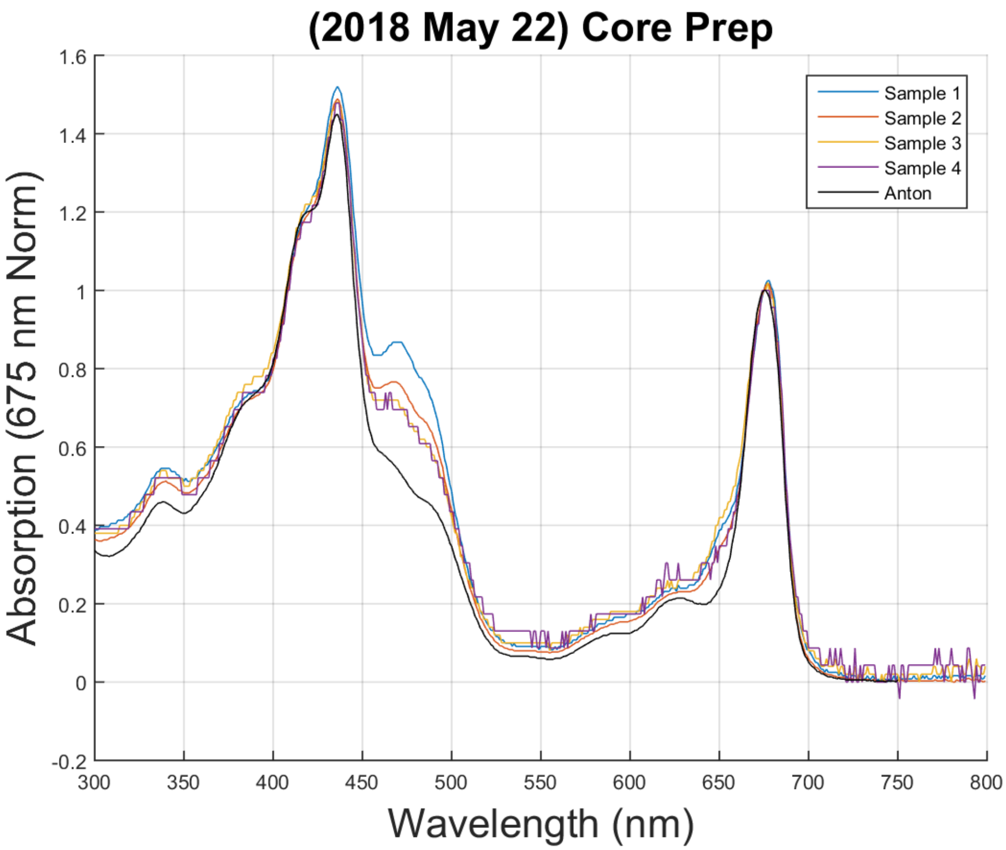

Figure A.4: Linear absorption measurements of diluted core samples collected off the column.

A.3 Reaction Center Isolation Procedure

Notes Before Starting: This part of the procedure starts with the sample resulting from the core prep and ends with a dilute sample of the D1-D2-Cytb559 complex. It is best to do the final concentration after this reaction center procedure so the sample can be stored long term in a stable state. **This is THE most crucial step for getting experiment quality sample with the appropriate 1.2 peak ratio.**

Initial Preparations

The Day Before:

- Pack small column. As before, leave both the intake and waste lines submerged in DI water to prevent bubbles from entering the system. Also ensure that the plunger gasket is tight.
- Prepare B buffer.
- Ensure appropriate amounts of β-DM are aliquoted to make B-β.

The Day Of:

- Acquire ice.
- Prepare B-β (1000 mL), C2-β (200 mL), and B-βT.
- Prepare the B-βT by first zeroing the scale to a 250 mL glass beaker with stir bar. Weigh out 25 g of Triton-X. Place the beaker on the mixing plate, ensuring the spin bar is well centered in the beaker. Quickly pour in B-β up to 100 mL line and begin spinning at high speed as soon as possible to prevent the solution from congealing. Leave solution spinning for 30-60 min until it is smooth (it will also be white with bubbles). Collect and cool on ice for at least 1 hr.
- Move column and pump system to refrigerator.
- Cool large centrifuge.

Procedure:

1. Set column equilibrating with B-β for 45 min.
    (a) Displace ∼25-30 mL volume used in equilibration. (In general, the small column passes solution much slower than the larger column. This is particularly true when loading the very viscous B-βT solution)
2. Prepare for B-βT incubation by setting 50 mL E. flask on ice and centered on mixing plate. Add 4 mL of Core sample from the previous procedure. Beginning the timer as soon as the first drop hits the sample, incubate for 20 min. As before, add the sample quickly and steadily in a drop-wise fashion. It helps to have a partner at this step.

3. Once the incubation is done, collect the sample in a 50 mL Falcon tube and begin loading onto column. The entire loading process can take up to 4 hours. The bead bed height will noticeably decrease as the beads pack tighter from the viscous B-βT solution.

4. Wash with B-β $\sim$90 min. The length of the wash is crucial for getting the final 1.2 ratio. The length of the wash will vary slightly every time depending the column/pump system conditions. Generally the wash is done when the eluant is clear and can be compared against a sample of water. Below are other possible markers that can be used to identify when to end the wash.

    (a) **Monitoring Linear Absorption Peak at 270 nm:** One can take samples of the eluant at different stages of the wash and measure their spectrum. The wash is done when the peak at about 270 nm disappears. However, this is not always the best indicator as the peak at 270 nm can have a nonlinear behavior and increase over time. This measurement is also sensitive to small changes to the column setup that can change the flow rate. (Figure (A.6) shows how the eluant spectrum changes over the wash time. Notice how the 270 nm peak is higher after washing for 160 minutes compared with washing for 145 minutes.)

    (b) **Monitoring Eluted Volume:** If the column is packed to roughly the same bead volume for each RC prep, measuring the volume of wash coming off the column can be a more reliable way to indentify a stopping point. We have had success when eluting the sample after washing with 160 mL of B-β.

5. Elute the sample off the column using C2-β. Let about 7 mL (roughly the volume of beads packed in the column) wash off the column before collecting in 2 mL centrifuge tubes. Collect until eluant is clear and comparable to water. Usually collect 12-15 tubes.

6. Measure spectra in 1 cm cuvette at eluted concentration with C2-β as the

background (compare results with Figure (A.5)). Check ratio of 417/435 nm absorption peaks (a ratio of 1.2 ensures a pure D1-D2-Cytb559 RC sample). Re-collect sample in centrifuge tubes after measurement.

7. Collected sample in 4 mL centrifuge filter tubes and spin at 6,500 xg for 45 min (or as long as it takes to concentrated all of the collect RC sample to an ultimate final volume of 1 mL). (If tight on time, this step can be perform before the final concentration step.)
8. Collect final volume of sample (concentrated or not) and leave in light-tight container overnight on ice.

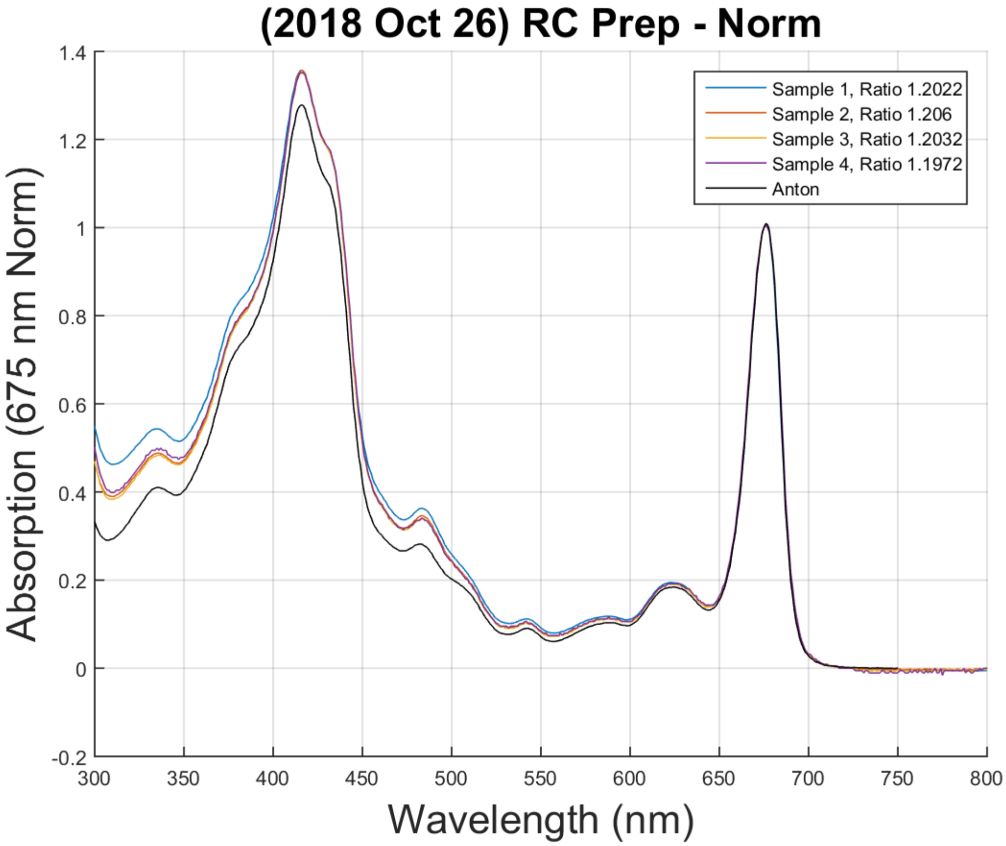

Figure A.5: Linear absorption measurements of purified RC collected in dilute batches off the column. Ratio values indicate the ratio of the absorption at 417/435 nm.

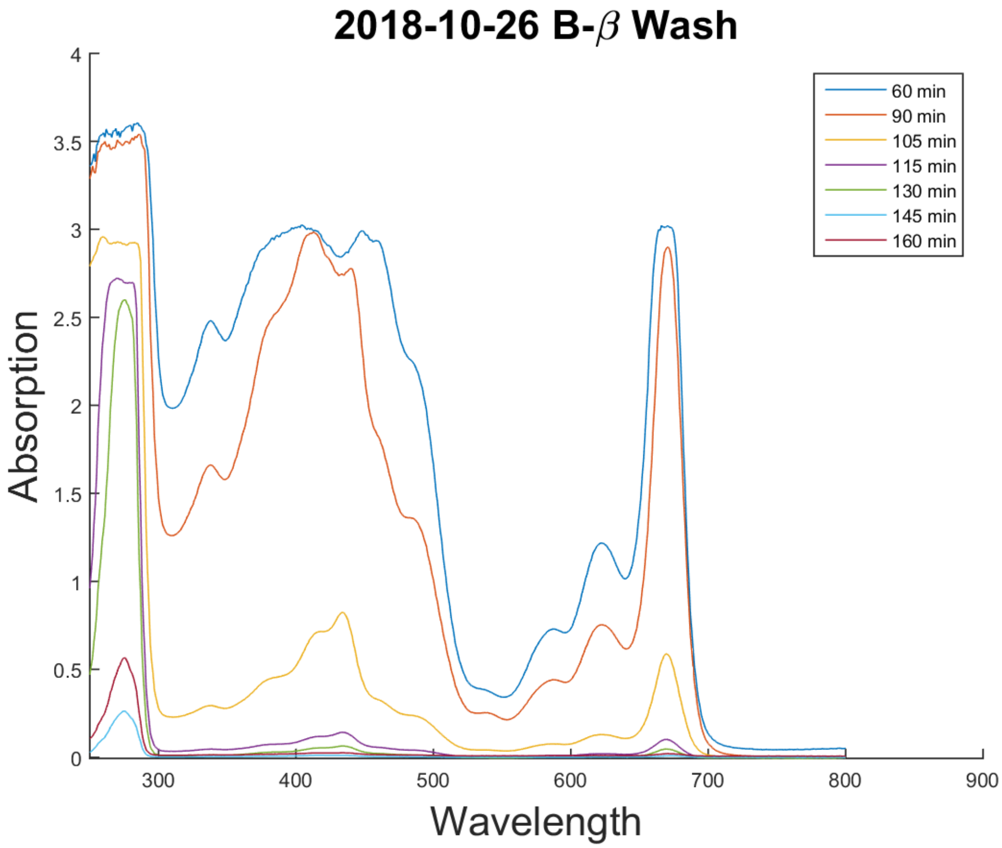

Figure A.6: Linear absorption spectra of waste off the column during the B-β wash at a range of time points. Notice the change in the peak at 270 nm.

A.4 Final Concentration

Notes Before Starting: The RC samples are most stable for long-term is the C2-β buffer is exchanged for Dx2-β. The final RC sample can be left for a few days before doing the buffer exchange, if necessary, but it is generally good practice to do it as soon as possible. I sometimes do it the same day at the RC prep, if I have the time.

Initial Preparations

The Day Before:

- Ensure there is enough β-DM aliquoted to make Dx2-β storage buffer.

The Day Of:

- Cool large and table-top centrifuges.
- Acquire ice.
- Prepare Dx2-β (50 mL).

Procedure:

1. If not already completed, concentrate eluted RC sample down to 1 mL as specified in the final step of the previous procedure.
2. Collect total 1 mL volume in 4 mL filter tube and add 1 mL Dx2-β. Spin at 6,500 xg for 45 min (or until final volume is $\sim$250 mL).
3. Collect filtered sample in small 30 kDa filter tubes for table top centrifuge. Spin at 14,000 xg for 90 min (or, until final volume is $\sim$50 μL).
4. Measure spectra in 1 cm cuvette at a 500x dilution (1 mL Dx2-β, 2 μL sample) and apply desired values to Stark Sample Dilution page of RC Sample Log Google Sheet (compare with Figure (A.7)). (For Stark experiment conditions, have optimal concentration when the OD at 677 nm is 0.6.) Dilute with glass buffer (either glycerol or 1:1 (volume:volume) glycerol:ethelyne-glycol).
5. Divide sample in 30 μL units (or at the appropriate volume to be used in experiments) and store in liquid nitrogen dewer until ready for experiments.

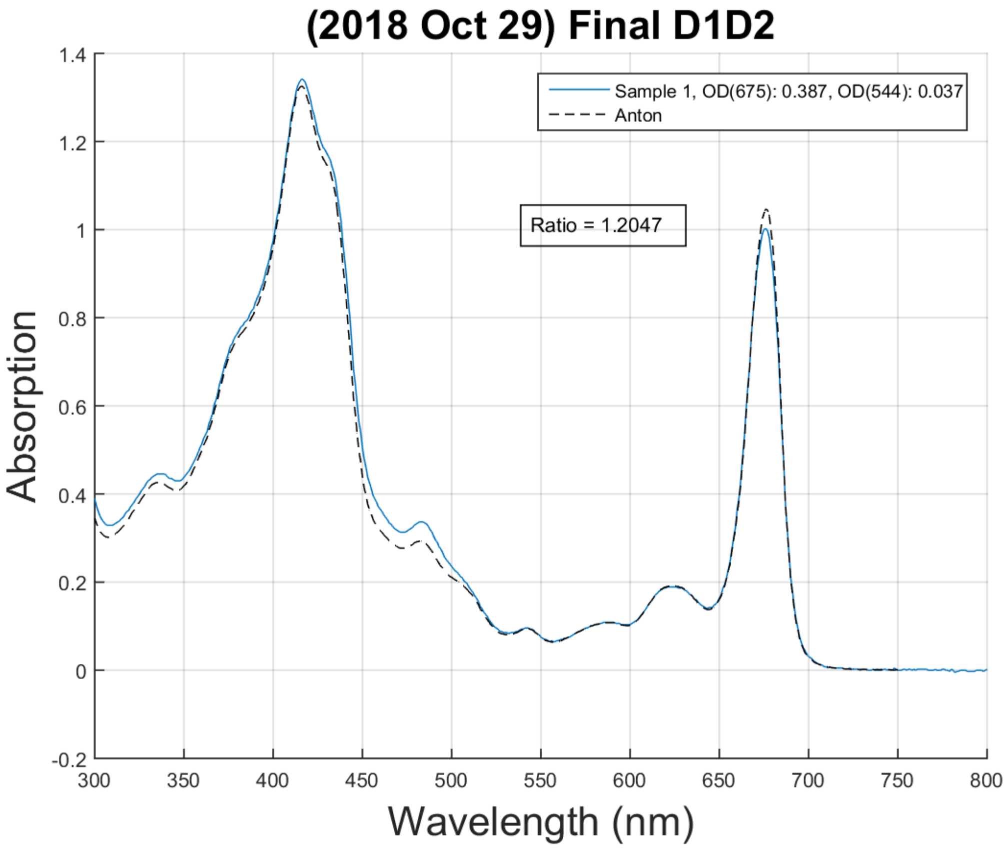

Figure A.7: Linear absorption measurement of the concentrated RC sample.

BIBLIOGRAPHY

BIBLIOGRAPHY

[1] P. Education, “Light Dependent Reactions”, .

[2] Y. Umena, K. Kawakami, J. R. Shen, N. Kamiya, “Crystal structure of oxygen-evolving photosystem II at a resolution of 1.9Å”, *Nature* **473**, 55 (2011).

[3] A. Gelzinis, D. Abramavicius, J. P. Ogilvie, L. Valkunas, “Spectroscopic properties of photosystem II reaction center revisited”, *Journal of Chemical Physics* **147** (2017).

[4] E. Romero, I. H. M. Van Stokkum, V. I. Novoderezhkin, J. P. Dekker, R. Van Grondelle, “Two different charge separation pathways in photosystem II”, *Biochemistry* **49**, 4300 (2010).

[5] V. I. Novoderezhkin, E. Romero, J. P. Dekker, R. Van Grondelle, “Multiple charge-separation pathways in photosystem II: Modeling of transient absorption kinetics”, *ChemPhysChem* **12**, 681 (2011).

[6] A. Loukianov, *Development of Two-dimensional Stark Spectroscopy for the Investigation of Photosynthetic Charge Separation*, Ph.D. thesis (2017).

[7] F. Müh, M. Plöckinger, T. Renger, “Electrostatic Asymmetry in the Reaction Center of Photosystem II”, *Journal of Physical Chemistry Letters* **8**, 850 (2017).

[8] A. Gelzinis, L. Valkunas, F. D. Fuller, “Tight-binding model of the photosystem II reaction center : application to two-dimensional electronic spectroscopy Tight-binding model of the photosystem II reaction center : application to two-dimensional electronic spectroscopy”, (2013).

[9] V. I. Novoderezhkin, J. P. Dekker, R. Van Grondelle, “Mixing of exciton and charge-transfer states in photosystem II reaction centers: Modeling of stark spectra with modified redfield theory”, *Biophysical Journal* **93**, 1293 (2007).

[10] R. van Grondelle, V. I. Novoderezhkin, J. P. Dekker, “Modeling of Light Harvesting and Primary Charge Separation in Photosystem I and Photosystem II”, in A. Laisk, L. Nedbal, Govindjee (eds.), “Photosynthesis in silico: Understanding Complexity from Molecules to Ecosystems”, chapter Modeling L, 33–53, Springer (2009).

[11] T. Renger, “Theory of excitation energy transfer: From structure to function”, *Photosynthesis Research* **102**, 471 (2009).

[12] A. Kell, X. Feng, M. Reppert, R. Jankowiak, "On the shape of the phonon spectral density in photosynthetic complexes", *Journal of Physical Chemistry B* **117**, 7317 (2013).

[13] A. Niedringhaus, *Probing Ultrafast Dynamics of Bacterial Reaction Centers Using Two-Dimensional Electronic Spectroscopy*, Ph.D. thesis (2017).

[14] F. D. Fuller, D. E. Wilcox, J. P. Ogilvie, "Pulse shaping based two-dimensional electronic spectroscopy in a background free geometry", *Optics Express* **22**, 17420 (2014).

[15] Y. Song, A. Konar, R. Sechrist, V. P. Roy, R. Duan, J. Dziurgot, V. Policht, Y. A. Matutes, K. J. Kubarych, J. P. Ogilvie, "Multispectral multidimensional spectrometer spanning the ultraviolet to the mid-infrared", *Review of Scientific Instruments* **90**, 013108 (2019).

[16] S. A. Kovalenko, A. L. Dobryakov, J. Ruthmann, N. P. Ernsting, "Femtosecond spectroscopy of condensed phases with chirped supercontinuum probing", *Physical Review A - Atomic, Molecular, and Optical Physics* **59**, 2369 (1999).

[17] I. E. Agency, "IEA: World Energy Outlook 2016", Technical report, Tech. Rep, Paris (2016).

[18] R. E. Blankenship, "Reaction Center Complexes", in "Molecular Mechanisms of Photosynthesis", chapter Chapter 6, 95–123, Blackwell Science Ltd, ISBN 9780470758472 (2002).

[19] R. E. Blankenship, "Antenna Complexes and Energy Transfer Processes", chapter Chapter 5, 61–94, Blackwell Science Ltd, Williston, VT, ISBN 9780470758472 (2002).

[20] J. Barber, "Photosystem II: the engine of life.", *Quarterly reviews of biophysics* **36**, 71 (2003).

[21] O. Nanba, K. Satoh, "Isolation of a photosystem II reaction center consisting of D-1 and D-2 polypeptides and cytochrome b-559", **84**, 109 (1987).

[22] D. A. Berthold, G. T. Babcock, C. F. Yocum, "A highly resolved, oxygen-evolving photosystem II preparation from spinach thylakoid membranes.", *FEBS Letters* **134**, 231 (1981).

[23] P. J. van Leeuwen, M. C. Nieveen, E. J. van de Meent, J. P. Dekker, H. J. van Gorkom, "Rapid and simple isolation of pure photosystem II core and reaction center particles from spinach", *Photosynthesis Research* **28**, 149 (1991).

[24] T. Kondo, A. Pinnola, W. J. Chen, L. Dall'Osto, R. Bassi, G. S. Schlau-Cohen, "Single-molecule spectroscopy of LHCSR1 protein dynamics identifies two distinct states responsible for multi-timescale photosynthetic photoprotection", *Nature Chemistry* 1–7 (2017).

[25] M. Gouterman, “Spectra of Porphyrins”, *Journal of Molecular Spectroscopy* **6**, 138 (1961).

[26] C. Weiss, “The Pi Electron Absorption Spectra of Chlorophylls in Solution”, *Journal of Molecular Spec* **44**, 37 (1971).

[27] G. Renger, T. Renger, “Photosystem II: The machinery of photosynthetic water splitting”, *Photosynthesis Research* **98**, 53 (2008).

[28] T. Cardona, A. Sedoud, N. Cox, A. W. Rutherford, “Charge separation in Photosystem II: A comparative and evolutionary overview”, *Biochimica et Biophysica Acta - Bioenergetics* **1817**, 26 (2012).

[29] J. R. Reimers, M. Biczysko, D. Bruce, D. F. Coker, T. J. Frankcombe, H. Hashimoto, J. Hauer, R. Jankowiak, T. Kramer, J. Linnanto, F. Mamedov, F. Mueh, M. Raetsep, T. Renger, S. Styring, J. Wan, Z. Wang, Z. Y. Wang-Otomo, Y. X. Weng, C. Yang, J. P. Zhang, A. Freiberg, E. Krausz, “Challenges facing an understanding of the nature of low-energy excited states in photosynthesis”, *Biochimica et Biophysica Acta - Bioenergetics* **1857**, 1627 (2016).

[30] B. A. Diner, F. Rappaport, “Structure , Dynamics , and Energetics of the Primary Photochemistry of Photosystem II of Oxygenic Photosynthesis”, *Annual Review of Plant Biology* **53**, 551 (2002).

[31] A. R. Holzwarth, “Data Analysis of Time-Resolved Measurements”, in J. Amesz, A. J. Hoff (eds.), “Biophysical Techniques in Photosynthesis”, 75–92, Springer Netherlands, Dordrecht, ISBN 978-0-306-47960-1 (1996).

[32] I. H. Van Stokkum, D. S. Larsen, R. Van Grondelle, “Global and target analysis of time-resolved spectra”, *Biochimica et Biophysica Acta - Bioenergetics* **1657**, 82 (2004).

[33] A. R. Holzwarth, M. G. Muller, M. Reus, M. Nowaczyk, J. Sander, M. Rogner, “Kinetics and mechanism of electron transfer in intact photosystem II and in the isolated reaction center: Pheophytin is the primary electron acceptor”, *Proceedings of the National Academy of Sciences* **103**, 6895 (2006).

[34] V. I. Prokhorenko, A. R. Holzwarth, “Primary Processes and Structure of the Photosystem II Reaction Center: A Photon Echo Study”, *The Journal of Physical Chemistry B* **104**, 11563 (2002).

[35] D. M. Jonas, “Two-dimensional femtosecond spectroscopy.”, *Annual review of physical chemistry* **54**, 425 (2003).

[36] J. A. Myers, K. L. Lewis, F. D. Fuller, P. F. Tekavec, C. F. Yocum, J. P. Ogilvie, “Two-dimensional electronic spectroscopy of the D1-D2-cyt b559 photosystem II reaction center complex”, *Journal of Physical Chemistry Letters* **1**, 2774 (2010).

[37] K. L. M. Lewis, F. D. Fuller, J. A. Myers, C. F. Yocum, S. Mukamel, D. Abramavicius, J. P. Ogilvie, "Simulations of the Two-Dimensional Electronic Spectroscopy of the Photosystem II Reaction Center", *The Journal of Physical Chemistry A* **117**, 34 (2013).

[38] F. D. Fuller, J. Pan, A. Gelzinis, V. Butkus, S. S. Senlik, D. E. Wilcox, C. F. Yocum, L. Valkunas, D. Abramavicius, J. P. Ogilvie, "Vibronic coherence in oxygenic photosynthesis", *Nature Chemistry* **6**, 706 (2014).

[39] A. Loukianov, A. Niedringhaus, B. Berg, J. Pan, S. S. Senlik, J. P. Ogilvie, "Two-dimensional Electronic Stark Spectroscopy", *The Journal of Physical Chemistry Letters* acs.jpclett.6b02695 (2017).

[40] H. G. Duan, V. I. Prokhorenko, E. Wientjes, R. Croce, M. Thorwart, R. J. Miller, "Primary Charge separation in the Photosystem II reaction center revealed by a global analysis of the two-dimensional electronic spectra", *Scientific Reports* **7**, 1 (2017).

[41] E. Romero, B. A. Diner, P. J. Nixon, W. J. Coleman, J. P. Dekker, R. Van Grondelle, "Mixed exciton-charge-transfer states in photosystem II: Stark spectroscopy on site-directed mutants", *Biophysical Journal* **103**, 185 (2012).

[42] V. I. Novoderezhkin, E. Romero, R. Van Grondelle, "How exciton-vibrational coherences control charge separation in the photosystem II reaction center", *Physical Chemistry Chemical Physics* **17**, 30828 (2015).

[43] H. Van Amerongen, L. Valkunas, R. van Grondelle, "The Exciton Concept", in "Photosynthetic Excitons", volume 551, chapter Chapter 3, 73–118, World Scientific Publishing, New Jersey, 1 edition, ISBN 9789812813664 (2000).

[44] J. R. Durrant, D. R. Klug, S. L. S. Kwa, R. van Grondelle, G. Porter, J. P. Dekker, "A Multimer Model for P680, the Primary Electron-Donor of Photosystem-II", *Proceedings of the National Academy of Sciences of the United States of America* **92**, 4798 (1995).

[45] B. Loll, J. Kern, W. Saenger, A. Zouni, J. Biesiadka, "Towards complete cofactor arrangement in the 3.0 Å resolution structure of photosystem II", *Nature* **438**, 1040 (2005).

[46] N. Kamiya, J.-R. Shen, "Crystal structure of oxygen-evolving photosystem II from Thermosynechococcus vulcanus at 3.7-A resolution", *Proceedings of the National Academy of Sciences* **100**, 98 (2003).

[47] G. Raszewski, W. Saenger, T. Renger, "Theory of optical spectra of photosystem II reaction centers: Location of the triplet state and the identity of the primary electron donor", *Biophysical Journal* **88**, 986 (2005).

[48] G. Raszewski, B. A. Diner, E. Schlodder, T. Renger, “Spectroscopic properties of reaction center pigments in photosystem II core complexes: Revision of the multimer model”, *Biophysical Journal* **95**, 105 (2008).

[49] V. I. Novoderezhkin, E. G. Andrizhiyevskaya, J. P. Dekker, R. Van Grondelle, “Pathways and timescales of primary charge separation in the photosystem II reaction center as revealed by a simultaneous fit of time-resolved fluorescence and transient absorption”, *Biophysical Journal* **89**, 1464 (2005).

[50] T. Renger, F. Müh, “Theory of excitonic couplings in dielectric media : Foundation of Poisson-TrEsp method and application to photosystem I trimers”, *Photosynthesis Research* **111**, 47 (2012).

[51] T. M. H. Creemers, C. A. De Caro, R. W. Visschers, R. Van Grondelle, S. Volker, “Spectral Hole Burning and Fluorescence Line Narrowing in Subunits of the Light-Harvesting Complex LH1 of Purple Bacteria”, *J. Phys. Chem. B* **103**, 9770 (1999).

[52] Y. Shibata, S. Nishi, K. Kawakami, J. R. Shen, T. Renger, “Photosystem II does not possess a simple excitation energy funnel: Time-resolved fluorescence spectroscopy meets theory”, *Journal of the American Chemical Society* **135**, 6903 (2013).

[53] S. Mukamel, *Principles of nonlinear optical spectroscopy*, Oxford series in optical and imaging sciences, Oxford University Press, ISBN 9780195092783 (1995).

[54] P. Hamm, M. Zanni, *Concepts and methods of 2D infrared spectroscopy*, Cambridge University Press, ISBN 9781107000056 (2011).

[55] A. Tokmakoff, “Nonlinear Spectroscopy”, *MIT OpenCourseWare* (2009).

[56] M. Cho, “Coherent two-dimensional optical spectroscopy.”, *Chemical reviews* **108**, 1331 (2008).

[57] A. M. Weiner, *Ultrafast Optics*, ISBN 9780471415398 (2009).

[58] K. L. M. Lewis, J. P. Ogilvie, “Probing Photosynthetic Energy and Charge Transfer with Two-Dimensional Electronic Spectroscopy”, *The Journal of Physical Chemistry Letters* **3**, 503 (2012).

[59] J. D. Hybl, Y. Christophe, D. M. Jonas, “Peak shapes in femtosecond 2D correlation spectroscopy”, *Chemical Physics* **266**, 295 (2001).

[60] J. D. Hybl, A. Albrecht Ferro, D. M. Jonas, “Two-dimensional Fourier transform electronic spectroscopy”, *The Journal of Chemical Physics* **115**, 6606 (2001).

[61] F. D. Fuller, J. P. Ogilvie, “Experimental Implementations of Two-Dimensional Fourier Transform Electronic Spectroscopy”, *Annual Review of Physical Chemistry* **66**, 667 (2015).

[62] L. Lepetit, G. Chériaux, M. Joffre, “Linear techniques of phase measurement by femtosecond spectral interferometry for applications in spectroscopy”, *Journal of the Optical Society of America B* **12**, 2467 (1995).

[63] C. Dorrer, N. Belabas, J.-P. Likforman, M. Joffre, “Spectral resolution and sampling issues in Fourier-transform spectral interferometry”, *Journal of the Optical Society of America B* **17**, 1795 (2000).

[64] J. A. Myers, K. L. M. Lewis, P. F. Tekavec, J. P. Ogilvie, “Two-color two-dimensional Fourier transform electronic spectroscopy with a pulse-shaper.”, *Optics express* **16**, 17420 (2008).

[65] L. P. DeFlores, R. A. Nicodemus, A. Tokmakoff, “Two-dimensional Fourier transform spectroscopy in the pump-probe geometry”, *Optics Letters* **32**, 2966 (2007).

[66] S.-h. Shim, M. T. Zanni, “How to turn your pump-probe instrument into a multidimensional spectrometer: 2D IR and Vis spectroscopies via pulse shaping.”, *Physical chemistry chemical physics : PCCP* **11**, 748 (2009).

[67] N. Krebs, I. Pugliesi, J. Hauer, E. Riedle, “Two-dimensional Fourier transform spectroscopy in the ultraviolet with sub-20 fs pump pulses and 250-720 nm supercontinuum probe”, *New Journal of Physics* **15** (2013).

[68] G. Cerullo, S. De Silvestri, “Ultrafast optical parametric amplifiers”, *Review of Scientific Instruments* **74**, 1 (2003).

[69] S. Kane, J. Squier, “Grism-pair stretcher–compressor system for simultaneous second- and third-order dispersion compensation in chirped-pulse amplification”, *Journal of the Optical Society of America B* **14**, 661 (1997).

[70] D. E. Wilcox, J. P. Ogilvie, “Comparison of pulse compression methods using only a pulse shaper”, *Journal of the Optical Society of America B* **31**, 1544 (2014).

[71] J. H. Easter, J. A. Nees, K. Krushelnick, Z. He, B. Hou, A. G. R. Thomas, “Compressor optimization with compressor-based multiphoton intrapulse interference phase scan (MIIPS)”, *Optics Letters* **37**, 1385 (2012).

[72] P. A. Tekavec, K. L. Lewis, F. D. Fuller, J. A. Myers, J. P. Ogilvie, “Toward broad bandwidth 2-d electronic spectroscopy: Correction of chirp from a continuum probe”, *IEEE Journal on Selected Topics in Quantum Electronics* **18**, 210 (2012).

[73] J. R. Reimers, Z.-L. Cai, R. Kobayashi, M. Rätsep, A. Freiberg, E. Krausz, “Assignment of the Q-bands of the chlorophylls: coherence loss via Qx - Qy mixing.”, *Scientific reports* **3**, 1 (2013).

[74] R. E. Blankenship, “Genetics, Assembly and Regulation of Photosynthetic Systems”, in “Molecular Mechanisms of Photosynthesis”, chapter Chapter 4, 204–219, Blackwell Science Ltd, Williston, VT, ISBN 9780470758472 (2002).

[75] M. T. Zanni, N.-H. Ge, Y. S. Kim, R. M. Hochstrasser, “Two-dimensional IR spectroscopy can be designed to eliminate the diagonal peaks and expose only the crosspeaks needed for structure determination”, *Proceedings of the National Academy of Sciences* **98**, 11265 (2001).

[76] G. S. Schlau-Cohen, A. Ishizaki, T. R. Calhoun, N. S. Ginsberg, M. Ballottari, R. Bassi, G. R. Fleming, “Elucidation of the timescales and origins of quantum electronic coherence in LHCII.”, *Nature Chem.* **4**, 389 (2012).

[77] N. S. Ginsberg, J. A. Davis, M. Ballottari, Y.-C. Cheng, R. Bassi, G. R. Fleming, “Solving structure in the CP29 light harvesting complex with polarization-phased 2D electronic spectroscopy”, *Proceedings of the National Academy of Sciences* **108**, 3848 (2011).

[78] S. Savikhin, W. S. Struve, “Femtosecond pump-probe spectroscopy of bacteriochlorophyll a monomers in solution”, *Biophysical Journal* **67**, 2002 (1994).

[79] M. Becker, V. Nagarajan, W. W. Parson, “Properties of the Excited-Singlet States of Bacteriochlorophyll a and Bacteriopheophytin a in Polar Solvents”, *Journal of the American Chemical Society* **113**, 6840 (1991).

[80] Y. J. Shiu, Y. Shi, M. Hayashi, C. Su, K. L. Han, S. H. Lin, “Femtosecond spectroscopy study of electronically excited states of Chlorophyll a molecules in ethanol”, *Chemical Physics Letters* **378**, 202 (2003).

[81] P. Martinsson, V. Sundstroem, A. Eva, “An ultrafast time-resolved anisotropy study of bacteriochlorophyll a in pyridine”, **465**, 107 (2000).

[82] S. Savikhin, H. van Amerongen, S. L. Kwa, R. van Grondelle, W. S. Struve, “Low-temperature energy transfer in LHC-II trimers from the Chl a/b light-harvesting antenna of photosystem II”, *Biophysical Journal* **66**, 1597 (1994).

[83] J. GOEDHEER, *Visible Absorption and Fluorescence of Chlorophyll and Its Aggregates in Solution*, ACADEMIC PRESS INC. (2014).

[84] T. G. EBREY, R. K. CLAYTON, “Polarization of Fluorescence From Bacteriochlorophyll in Castor Oil, in Chromatophores and As P870 in Photosynthetic Reaction Centers”, *Photochemistry and Photobiology* **10**, 109 (1969).

[85] J. Petke, G. Maggiora, L. Shipman, R. Chistoffersen, “Stereoelectronic properties of photosynthetic and related systems - VI. ab initio configuration interaction calculations on the ground and lower excited singlet and triplet states of ethyl bacteriochlorophyllide-a and ethyl bacteriopheophorbide-a”, *Photochemistry and Photobiology* **32**, 399 (1980).

[86] P. Martinsson, J. A. I. Oksanen, M. Hilgendorft, E. Åkesson, P. Hynninen, V. Sundström, “Characterisation of Chlorophyll a and Chlorophyll b Monomers in Various Solvent Environments with Ultrafast Spectroscopy”, in G. Garab (ed.), “Photosynthesis: Mechanisms and Effects: Volume I–V: Proceedings of the XIth International Congress on Photosynthesis, Budapest, Hungary, August 17–22, 1998”, 457–460, Springer Netherlands, Dordrecht, ISBN 978-94-011-3953-3 (1998).

[87] P. Martinsson, J. a. Oksanen, M. Hilgendorff, P. H. Hynninen, V. Sundström, E. Åkesson, “Dynamics of ground and excited state chlorophylla molecules in pyridine solution probed by femtosecond transient absorption spectroscopy”, *Chemical Physics Letters* **309**, 386 (1999).

[88] D. Leupold, S. Mory, R. König, P. Hoffmann, B. Hieke, “Laser action and excited state absorption of chlorophyll-a”, *Chemical Physics Letters* **45**, 567 (1977).

[89] R. A. Avarmaa, K. K. Rebane, “High-resolution optical spectra of chlorophyll molecules”, *Spectrochimica Acta Part A: Molecular Spectroscopy* **41**, 1365 (1985).

[90] K. K. Rebane, R. A. Avarmaa, “Sharp line vibronic spectra of chlorophyll and its derivatives in solid solutions”, *Chemical Physics* **68**, 191 (1982).

[91] M. Rätsep, J. Linnanto, A. Freiberg, “Mirror symmetry and vibrational structure in optical spectra of chlorophyll a”, *Journal of Chemical Physics* **130** (2009).

[92] M. Rätsep, Z. L. Cai, J. R. Reimers, A. Freiberg, “Demonstration and interpretation of significant asymmetry in the low-resolution and high-resolution Qy fluorescence and absorption spectra of bacteriochlorophyll a”, *Journal of Chemical Physics* **134** (2011).

[93] Y. Shi, J. Y. Liu, K. L. Han, “Investigation of the internal conversion time of the chlorophyll a from S3, S2 to S1”, *Chemical Physics Letters* **410**, 260 (2005).

[94] D. Kosumi, K. Nakagawa, S. Sakai, Y. Nagaoka, S. Maruta, M. Sugisaki, T. Dewa, M. Nango, H. Hashimoto, “Ultrafast intramolecular relaxation dynamics of Mg- and Zn-bacteriochlorophyll a”, *Journal of Chemical Physics* **139** (2013).

[95] W. P. Bricker, P. M. Shenai, A. Ghosh, Z. Liu, M. G. M. Enriquez, P. H. Lambrev, H. S. Tan, C. S. Lo, S. Tretiak, S. Fernandez-Alberti, Y. Zhao, “Non-radiative relaxation of photoexcited chlorophylls: Theoretical and experimental study”, *Scientific Reports* **5**, 1 (2015).

[96] H. M. Visser, O. J. Somsen, F. van Mourik, S. Lin, I. H. van Stokkum, R. van Grondelle, "Direct observation of sub-picosecond equilibration of excitation energy in the light-harvesting antenna of Rhodospirillum rubrum", *Biophysical Journal* **69**, 1083 (1995).

[97] K. L. Wells, Z. Zhang, J. R. Rouxel, H. S. Tan, "Measuring the spectral diffusion of chlorophyll a using two-dimensional electronic spectroscopy", *Journal of Physical Chemistry B* **117**, 2294 (2013).

[98] R. Moca, S. R. Meech, I. A. Heisler, "Two-Dimensional Electronic Spectroscopy of Chlorophyll a: Solvent Dependent Spectral Evolution", *Journal of Physical Chemistry B* **119**, 8623 (2015).

[99] E. Meneghin, C. Leonardo, A. Volpato, L. Bolzonello, E. Collini, "Mechanistic insight into internal conversion process within Q-bands of chlorophyll a", *Scientific Reports* **7**, 1 (2017).

[100] W. T. Simpson, D. L. Peterson, "Coupling strength for resonance force transfer of electronic energy in Van der Waals solids", *The Journal of Chemical Physics* **26**, 588 (1957).

[101] S. Bhandari, M. S. Cheung, E. Geva, L. Kronik, B. D. Dunietz, "Fundamental Gaps of Condensed-Phase Organic Semiconductors from Single-Molecule Calculations using Polarization-Consistent Optimally Tuned Screened Range-Separated Hybrid Functionals", *Journal of Chemical Theory and Computation* **14**, 6287 (2018).

[102] Y. Shao, Z. Gan, E. Epifanovsky, A. T. Gilbert, M. Wormit, J. Kussmann, A. W. Lange, A. Behn, J. Deng, X. Feng, D. Ghosh, M. Goldey, P. R. Horn, L. D. Jacobson, I. Kaliman, R. Z. Khaliullin, T. Kus, A. Landau, J. Liu, E. I. Proynov, Y. M. Rhee, R. M. Richard, M. A. Rohrdanz, R. P. Steele, E. J. Sundstrom, H. L. Woodcock, P. M. Zimmerman, D. Zuev, B. Albrecht, E. Alguire, B. Austin, G. J. Beran, Y. A. Bernard, E. Berquist, K. Brandhorst, K. B. Bravaya, S. T. Brown, D. Casanova, C. M. Chang, Y. Chen, S. H. Chien, K. D. Closser, D. L. Crittenden, M. Diedenhofen, R. A. Distasio, H. Do, A. D. Dutoi, R. G. Edgar, S. Fatehi, L. Fusti-Molnar, A. Ghysels, A. Golubeva-Zadorozhnaya, J. Gomes, M. W. Hanson-Heine, P. H. Harbach, A. W. Hauser, E. G. Hohenstein, Z. C. Holden, T. C. Jagau, H. Ji, B. Kaduk, K. Khistyaev, J. Kim, J. Kim, R. A. King, P. Klunzinger, D. Kosenkov, T. Kowalczyk, C. M. Krauter, K. U. Lao, A. D. Laurent, K. V. Lawler, S. V. Levchenko, C. Y. Lin, F. Liu, E. Livshits, R. C. Lochan, A. Luenser, P. Manohar, S. F. Manzer, S. P. Mao, N. Mardirossian, A. V. Marenich, S. A. Maurer, N. J. Mayhall, E. Neuscamman, C. M. Oana, R. Olivares-Amaya, D. P. Oneill, J. A. Parkhill, T. M. Perrine, R. Peverati, A. Prociuk, D. R. Rehn, E. Rosta, N. J. Russ, S. M. Sharada, S. Sharma, D. W. Small, A. Sodt, T. Stein, D. Stück, Y. C. Su, A. J. Thom, T. Tsuchimochi, V. Vanovschi, L. Vogt, O. Vydrov, T. Wang, M. A. Watson, J. Wenzel, A. White, C. F. Williams, J. Yang, S. Yeganeh,

S. R. Yost, Z. Q. You, I. Y. Zhang, X. Zhang, Y. Zhao, B. R. Brooks, G. K. Chan, D. M. Chipman, C. J. Cramer, W. A. Goddard, M. S. Gordon, W. J. Hehre, A. Klamt, H. F. Schaefer, M. W. Schmidt, C. D. Sherrill, D. G. Truhlar, A. Warshel, X. Xu, A. Aspuru-Guzik, R. Baer, A. T. Bell, N. A. Besley, J. D. Chai, A. Dreuw, B. D. Dunietz, T. R. Furlani, S. R. Gwaltney, C. P. Hsu, Y. Jung, J. Kong, D. S. Lambrecht, W. Liang, C. Ochsenfeld, V. A. Rassolov, L. V. Slipchenko, J. E. Subotnik, T. Van Voorhis, J. M. Herbert, A. I. Krylov, P. M. Gill, M. Head-Gordon, "Advances in molecular quantum chemistry contained in the Q-Chem 4 program package", *Molecular Physics* **113**, 184 (2015).

[103] T. N. Truong, E. V. Stefanovich, "A new method for incorporating solvent effect into the classical, ab initio molecular orbital and density functional theory frameworks for arbitrary shape cavity", *Chemical Physics Letters* **240**, 253 (1995).

[104] V. Barone, M. Cossi, "Quantum calculation of molecular energies and energy gradients in solution by a conductor solvent model", *Journal of Physical Chemistry A* **102**, 1995 (1998).

[105] J. Tomasi, B. Mennucci, R. Cammi, "Quantum Mechanical Continuum Solvation Models", *Chemical Reviews* **105**, 2999 (2005).

[106] R. Ditchfield, W. J. Hehre, J. A. Pople, "Self-Consistent Molecular-Orbital Methods. IX. An Extended Gaussian-Type Basis for Molecular-Orbital Studies of Organic Molecules", *The Journal of Chemical Physics* **54**, 724 (2004).

[107] R. Baer, D. Neuhauser, "Density functional theory with correct long-range asymptotic behavior", *Physical Review Letters* **94**, 2 (2005).

[108] S. Refaely-Abramson, M. Jain, S. Sharifzadeh, J. B. Neaton, L. Kronik, "Solid-state optical absorption from optimally tuned time-dependent range-separated hybrid density functional theory", *Physical Review B - Condensed Matter and Materials Physics* **92**, 1 (2015).

[109] L. Kronik, S. Kümmel, "Dielectric Screening Meets Optimally Tuned Density Functionals", *Advanced Materials* **30**, 1 (2018).

[110] A. K. Manna, S. Refaely-Abramson, A. M. Reilly, A. Tkatchenko, J. B. Neaton, L. Kronik, "Quantitative Prediction of Optical Absorption in Molecular Solids from an Optimally Tuned Screened Range-Separated Hybrid Functional", *Journal of Chemical Theory and Computation* **14**, 2919 (2018).

[111] A. Nitzan, *Chemical Dynamics in Condensed Phases. Relaxation, Transfer and Reactions in Condensed Matter Molecular Systems* (2006).

[112] V. Novoderezhkin, E. Romero, R. van Grondelle, "How exciton-vibrational coherences control charge separation in the photosystem II reaction center", *Phys. Chem. Chem. Phys.* (2015).

[113] C. Eijckelhoff, H. Van Roon, M. L. Groot, R. Van Grondelle, J. P. Dekker, "Purification and spectroscopic characterization of photosystem II reaction center complexes isolated with or without Triton X-100", *Biochemistry* **35**, 12864 (1996).

[114] P. F. Tekavec, J. A. Myers, K. L. M. Lewis, J. P. Ogilvie, "Two-dimensional electronic spectroscopy with a continuum probe", *Optics Letters* **34**, 1390 (2009).

[115] T. Wilhelm, J. Piel, E. Riedle, "Sub-20-fs pulses tunable across the visible from a blue-pumped single-pass noncollinear parametric converter.", *Optics letters* **22**, 1494 (1997).

[116] P. Tournois, "Acousto-optic programmable dispersive filter for adaptive compensation of group delay time dispersion in laser systems", *Optics Communications* **140**, 245 (1997).

[117] D. E. Wilcox, J. P. Ogilvie, "Comparison of pulse compression methods using only a pulse shaper", *Journal of the Optical Society of America B* **31**, 1544 (2014).

[118] M. Bradler, P. Baum, E. Riedle, "Femtosecond continuum generation in bulk laser host materials with sub-μJ pump pulses", *Applied Physics B: Lasers and Optics* **97**, 561 (2009).

[119] P. A. Tekavec, K. L. M. Lewis, F. D. Fuller, J. A. Myers, J. P. Ogilvie, "Toward broad bandwidth 2-d electronic spectroscopy: Correction of chirp from a continuum probe", *IEEE Journal on Selected Topics in Quantum Electronics* **18**, 210 (2012).

[120] D. M. Jonas, M. J. Lang, Y. Nagasawa, T. Joo, G. R. Fleming, "Pump Probe Polarization Anisotropy Study of Femtosecond Energy Transfer within the Photosynthetic Reaction Center of Rhodobacter sphaeroides R26", *Journal of Physical Chemistry* **100**, 12660 (1996).

[121] S. R. Greenfield, M. Seibert, Govindjee, M. R. Wasielewski, "Direct Measurement of the Effective Rate Constant for Primary Charge Separation in Isolated Photosystem II Reaction Centers", *The Journal of Physical Chemistry B* **101**, 2251 (2002).

[122] A. Konar, R. Sechrist, Y. Song, V. R. Policht, P. D. Laible, D. F. Bocian, D. Holten, C. Kirmaier, J. P. Ogilvie, "Electronic Interactions in the Bacterial Reaction Center Revealed by Two-Color 2D Electronic Spectroscopy", *Journal of Physical Chemistry Letters* **9**, 5219 (2018).

[123] B. Donovan, L. A. Walker, D. Kaplan, M. Bouvier, C. F. Yocum, R. J. Sension, "Structure and Function in the Isolated Reaction Center Complex of Photosystem II. 1. Ultrafast Fluorescence Measurements of PSII", *The Journal of Physical Chemistry B* **101**, 5232 (1997).

[124] R. J. van Dorssen, J. Breton, J. J. Plijter, K. Satoh, H. J. van Gorkom, J. Amesz, "Spectroscopic properties of the reaction center and of the 47 kDa chlorophyll protein of Photosystem II", *BBA - Bioenergetics* **893**, 267 (1987).

[125] S. L. Kwa, W. R. Newell, R. van Grondelle, J. P. Dekker, "The reaction center of photosystem II studied with polarized fluorescence spectroscopy", (1992).

[126] E. Romero, I. H. Van Stokkum, J. P. Dekker, R. Van Grondelle, "Ultrafast carotenoid band shifts correlated with Chlzexcited states in the photosystem II reaction center: Are the carotenoids involved in energy transfer?", *Physical Chemistry Chemical Physics* **13**, 5573 (2011).

[127] G. S. Engel, E. L. Read, T. R. Calhoun, T. K. Ahn, T. Mančál, R. E. Blankenship, G. R. Fleming, "Two dimensional Fourier transform electronic spectroscopy: Evolution of cross peaks in the Fenna-Matthews-Olson complex", *Springer Series in Chemical Physics* **88**, 392 (2007).

[128] G. Panitchayangkoon, D. V. Voronine, D. Abramavicius, J. R. Caram, N. H. C. Lewis, S. Mukamel, G. S. Engel, "Direct evidence of quantum transport in photosynthetic light-harvesting complexes", *Proceedings of the National Academy of Sciences* **108**, 20908 (2011).

[129] E. Harel, G. S. Engel, "Quantum coherence spectroscopy reveals complex dynamics in bacterial light- harvesting complex 2 (LH2)", *Proc. Natl. Acad. Sci. U.S.A.* **109**, 706 (2011).

[130] S. Westenhoff, D. Paleček, P. Edlund, P. Smith, D. Zigmantas, D. Palecek, D. Palecek, "Coherent picosecond exciton dynamics in a photosynthetic reaction center, Supplementary material", *Journal of the American Chemical Society* **134**, 16484 (2012).

[131] H.-G. Duan, V. I. Prokhorenko, R. J. Cogdell, K. Ashraf, A. L. Stevens, M. Thorwart, R. J. D. Miller, "Nature does not rely on long-lived electronic quantum coherence for photosynthetic energy transfer", *Proceedings of the National Academy of Sciences* **114**, 8493 (2017).

[132] V. R. Policht, A. Niedringhaus, J. P. Ogilvie, "Characterization of Vibrational Coherence in Monomeric Bacteriochlorophyll a by Two-Dimensional Electronic Spectroscopy", *Journal of Physical Chemistry Letters* **9**, 6631 (2018).

[133] J. L. Herek, M. Wendling, Z. He, T. Polívka, G. Garcia-Asua, R. J. Cogdell, C. N. Hunter, R. Van Grondelle, V. Sundström, T. Pullerits, "Ultrafast carotenoid band shifts: Experiment and theory", *Journal of Physical Chemistry B* **108**, 10398 (2004).